Contact Charge Electrophoresis: Cooperative dynamics of particle dispersions

Shashank Pandey

Submitted in partial fulfillment of the
requirements for the degree
of Doctor of Philosophy
in the Graduate School of Arts and Sciences

COLUMBIA UNIVERSITY

2019

ABSTRACT

Contact Charge Electrophoresis: Cooperative dynamics of particle dispersions

Shashank Pandey

In 1745 a Scotch Benedictine monk Andrew Gordon discovered Contact Charge Electrophoresis (CCEP) which remained in dormant state for centuries until gaining renewed prominence in the field of particle manipulation and actuation. Contact Charge Electrophoresis (CCEP) refers to the continuous to and fro motion of a conductive object between two electrodes subject to an applied voltage. The continuous motion of the conductive particle and the low power requirement provide an attractive alternative to traditional methods for particle manipulation techniques such as dielectrophoresis. Recent efforts to understand and apply CCEP have focused on the motion of single particles and we present dynamics of multiple conductive particles dispersed in non-conducting media that utilize CCEP to perform tasks like pumping and cargo transport operations as well as multiparticle clusters capable of tailored trajectories.

Chapters 1 provides motivation for this work and background on CCEP. Providing brief details on development of microfluidic devices and modeling that are covered in more details in subsequent chapters. It also focuses on the historical aspect of CCEP, relevant background, mechanism, physics, application strategies in literature, strategies developed for single particle systems and possible extension to multiparticle systems.

Chapters 2 and 3 talk about the dynamics and modeling of multiple conductive par-

ticles both in dispersion and aggregates/clusters powered by CCEP. In Chapter 2, we propose a new hybrid approach based on image-based method proposed earlier by Bonnecaze[18] for modeling CCEP. It covers challenges to modeling a multiple particle system in confinement, dynamics of chain formation and dynamics of cluster comprising conductive and non-conductive particles between two electrodes. While Chapter 3 focuses on details of methods and techniques used in development of the simulation for dispersion of conductive particles in confinement. We illustrate variation of conductivity for complete range of electrode separation with varying volume fraction.

Chapter 4 expands on multiple particle CCEP and shows that when we physically constrain particle trajectories to parallel tracks between the electrodes the emergence of traveling waves is observed. These traveling waves of mechanical actuation can be realized in linear arrays of electromechanical oscillators that move and interact via electrostatic forces. Conductive spheres oscillate between biased electrodes through cycles of contact charging and electrostatic actuation. The combination of repulsive interactions among the particles and spatial gradients in their natural frequencies lead to phase locked states characterized by gradients in the oscillation phase. The frequency and wavelength of these traveling waves can be specified independently by varying the applied voltage and the electrode separation. We demonstrate how traveling wave synchronization can enable the directed transport of material cargo. Our results suggests that simple energy inputs can power complex patterns of mechanical actuation with potential opportunities for soft robotics and colloidal machines.

Chapter 5 systematically investigate the dynamics of cluster comprising multiple spherical conductive particles driven via contact charge electrophoresis (CCEP). We are specifically interested in understanding dynamics of closed packed cluster of particles with both conductive and non-conductive particles in three dimensions(3D). Finally, Chapter 6 summarizes new ideas and proposes possible applications for multiple particle Contact charge electrophoresis motivated by this dissertation.

Table of Contents

List of Figures

List of Tables

Acknowledgments

First and foremost, I would like to thank my advisor Dr. Kyle Bishop. Kyle, your enthusiasm and dedication for research as well as your high standards for excellence and insight have helped me develop myself into a better version of myself. I appreciate your tolerance for all the silly ideas and bad presentations that you helped me make better.

To my friends and colleagues, these last five years have been a roller-coaster filled with fun and learning thanks to you all. It has been a pleasure working with you all. Mikolaj Kowalik, you helped me lot during my initial years working on modeling and simulations. I would always appreciate the scientific discussions with Yong Dou with whom I worked together on a really interesting project and learned lots of experimental designs from. Wenjie Fei, thanks for all the help, reminders and office discussions. Finally thanks to my friends Anish Dasgupta, Anirban Das, Digvijay Deswal and Abhishek Choudhary, if it wasn't for you all last 5 years would have turned out much harder.

To my family, there's not enough space here to show my gratitude and love for you all. Specifically my parents and my brother Aditya, who have always been there for me through every hardship in my life. I care for you all, and have always been grateful for your support.

For my family

Chapter 1

Contact Charge Electrophoresis: Fundamentals and Microfluidic Applications

1.1 Introduction

[1]In 1745, the Scotch Benedictine monk Andrew Gordon suspended a small metal sphere by a fine silk thread between two electrified bells [169]. He marveled as the sphere oscillated steadily between the bells, creating a gentle ringing sound (Fig. 1.1a). Years later, Benjamin Franklin combined Gordon's chimes with his recent invention, the lightning rod, to provide audible warning of approaching thunderstorms to further his own investigations of atmospheric electricity [74]. Franklin later noted the

[1]The material presented in this chapter has been reprinted with permission from Kyle J. M. Bishop, Aaron M. Drews, Charles A. Cartier, Shashank Pandey, and Yong Dou, Langmuir 2018, 34, 63156327. Copyright 2018 American Chemical Society. Author responsibilities were as follows: All the experiment designs reviewed were contributed by all the authors. All authors contributed to final text specifically K.J.M.B.

remarkably small amount of charge needed to drive the oscillator, and reported nearly indefinite operation of the chimes if the air were removed by means of an evacuated chamber. Legend has it that he left the bells audibly ringing during a trip to Europe, to his wife's great irritation [169].

These early investigations of Gordon's chimes mark the first application of electricity to perform mechanical work – that is, the first electric motors. Franklin took this new idea further with his "electric wheel", which used the repeated charging and electrostatic actuation of brass thimbles mounted on a carousel to drive steady rotational motions (Fig. 1.1b) [73]. In a world of powerful steam engines and water wheels, the electrostatic motor was merely a curiosity – Franklin himself suggested its use in an autonomous turkey rotisserie. In 1821, Michael Faraday demonstrated a superior electric motor based on electromagnetic forces, which continue to power our electric appliances and vehicles today. By contrast, the electrostatic motor faded into the annals of history, revived only for the occasional science demonstration [126].

Now this ca. 250 year-old technology has found new life in powering particle motions and mechanical functions at the micro- and nanoscales. In a process called contact charge electrophoresis (CCEP), a conductive particle [200, 117, 122, 58, 32, 54, 52] (or droplet [94, 114, 174, 113, 103, 4, 102, 105]) is first charged by contact with an electrode surface in the presence of an electric field and then actuated by that field via electrophoresis. Each time the particle contacts an electrode, its charge changes sign and its velocity changes direction (Fig. 1.1c). CCEP offers several unique characteristics that distinguish it from related forms of electric actuation such as electrophoresis (EP) and dielectrophoresis (DEP). Most notably, CCEP allows for rapid, sustained particle motion driven by constant voltages with small energy inputs. These at-

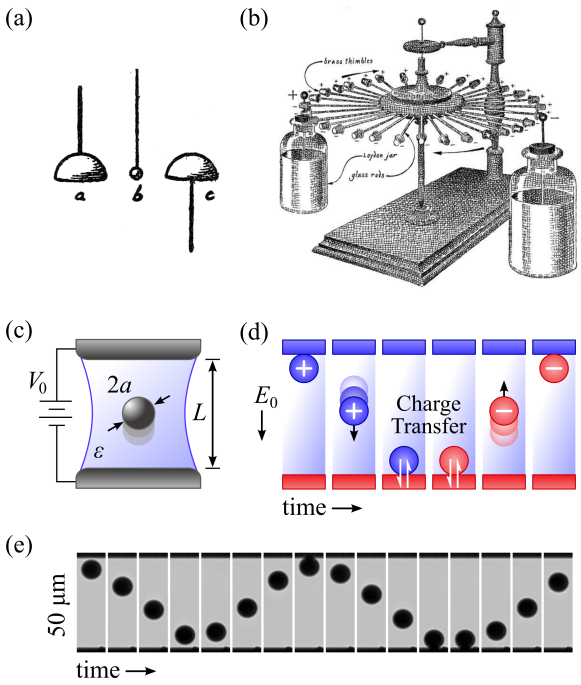

Figure 1.1: (a) Gordon's chimes as described in 1752[169]. (*image is public domain*) A small metal clapper b was positioned between two metal bells (a and c). An electrostatic voltage between the bells caused the clapper to oscillate continuously. (b) Franklin's electric wheel[73]. (*image is public domain*) (c) Experimental schematic of a conductive particle immersed in a dielectric fluid between two electrodes. (Adapted from reference [58] with permission of The Royal Society of Chemistry.) (d) Basic mechanism of contact charge electrophoresis. (Adapted from reference [58] with permission of The Royal Society of Chemistry.) (e) Optical images of a 10mm silver-coated glass particle subject to a constant electric field ($E_0 = 2.5\text{V/mm}$) at intervals of 24 ms. The particle oscillates indefinitely between the electrodes as long as the voltage is applied. (Reproduced from reference [54]; copyright 2015 American Chemical Society.)

tributes make CCEP an attractive mechanism for powering the active components needed for mobile (i.e., small, battery powered) microfluidic technologies such as those used in Point-of-Care diagnostics [82, 88]. To capitalize on these advantages, one must look beyond simple oscillatory motions and develop strategies for rectifying CCEP dynamics to perform useful functions.

This Feature Article presents our perspective on the coming renaissance of electrostatic motors in microfluidics and active colloidal systems. We introduce the basic characteristics of CCEP, highlighting the key distinctions between this mechanism and more common forms of electric particle actuation such as EP and DEP. We review the fundamental physics underlying contact charging and particle dynamics, emphasizing open questions on the role of particle shape and on the collective behaviors of many-particle systems. We describe recent applications of CCEP motions in powering microfluidic unit operations such as particle transport, separations, and fluid mixing. Looking forward, we discuss two frontiers in the study and application of CCEP: the realization of electrostatic motors and machines at the nanoscale and the creation of active macroscopic materials based on coupled electrostatic oscillators. Ultimately, it is our hope that the long-neglected phenomenon of CCEP will find its place along side other widely used methods for electric particle manipulation.

1.2 Basic Characteristics of CCEP

The simplest realization of CCEP is illustrated in Figure 1.1e, which shows the rapid oscillatory motion of a conductive sphere (radius, $a = 5\mu m$) immersed in mineral oil between two electrodes subject to a constant voltage. The particle acts as a

mechanical "shuttle" that transports charge between the two electrodes [117, 122]. When it makes electrical contact with the electrode surface, the particle acquires a net charge such that its voltage is equal to that of the electrode. Now charged, the particle migrates under the influence of the electric field with a velocity determined by the balance of the electrostatic force and the hydrodynamic drag force. Each time the particle contacts an electrode its charge changes sign, and its velocity changes direction.

This basic mechanism – combining contact charging and electrostatic actuation – is no different than that of Gordon's chimes discovered more than two centuries ago. More recently, the motion of conductive particles in dielectric liquids subject to strong electric fields has been studied to understand how the presence of such particles affects the conductivity and dielectric strength of insulating liquids [12, 200, 117]. Electromechanical "charge shuttles", as they are sometimes called, have also been studied for their potential relevance to micro- and nano-electromechanical systems [87, 202]. In addition to solid particles, liquid droplets have been shown to "bounce" off electrodes[144, 68, 94, 114, 103, 216] or even liquid interfaces [174, 91] by an analogous mechanism. The electrophoresis of charged drops (ECD[103]) in dielectric fluids enables new strategies for manipulating aqueous droplets within microfluidic systems [134, 101]. Here, we focus our discussion on the motions of *solid* particles moving in *viscous* fluids, in which the effects of fluid and particle inertia can be neglected.

1.2.1 Scaling Analysis

CCEP dynamics are governed primarily by two processes: contact charging, the acquisition of charge by a conductive particle upon contact with an electrode, and electrophoresis, the movement of the now-charged particle in the applied electric field. The following order-of-magnitude analysis of these processes shows how CCEP motions depend on system parameters such as the particle radius a, the electrode separation L, and the electric field strength $E_0 = V_0/L$; a more rigorous analysis is provided below. To estimate the charge acquired by the sphere, consider that the charge density on the electrode surface is εE_0 where ε is the permittivity of the liquid. When the sphere makes electrical contact with the electrode, the charge induced on its surface can be approximated as the charge density times the surface area, $q \sim 4\pi a^2 \varepsilon E_0$. The charged particle experiences an electric force in the field as approximated by that on a point charge, $F_E \sim qE_0$. At low Reynolds numbers, the resulting motion of the particle through its viscous surroundings creates a drag force that can be approximated by Stokes law $F_H \sim 6\pi a\eta U$, where η is the fluid visocity. At steady-state, the particle velocity U is determined by equating the electrostatic and hydrodynamic forces to obtain $U \sim \varepsilon a E_0^2/\eta$. This approximate relation has been confirmed by several experimental studies [112, 200, 117, 122, 54] and helps to illustrate the key characteristics of CCEP motion.

1.2.2 Carrier Liquid

CCEP is only effective in dielectric fluids with sufficiently low electrical conductivity (e.g., mineral oil[32], toluene [117], silicone oil[104]). A charged particle immersed in a

fluid of conductivity K will discharge on a time scale, $\tau_d \sim \varepsilon/K$. To sustain continuous motion, this charge relaxation time must be slow relative to the time between contact charging "collisions" (typically, ∼1 ms). Consequently, CCEP is effective in mineral oil ($\tau_d \sim 10s$) but ineffective in deionized water ($\tau_d \sim 10\mu s$) [32]. By contrast, traditional electrophoresis is effective in high dielectric solvents (typically, water), in which ions are soluble and particles can acquire a significant surface charge (e.g., by dissociation of ionizable surface groups). In low dielectric (nonpolar) solvents, the spontaneous charging of particle surfaces requires additives such as surfactants that stabilize dissociated ions and increase the electrical conductivity of the liquid [76, 131, 172]; without such additives, electrophoresis becomes ineffective and/or unreliable. CCEP therefore offers an attractive alternative to traditional EP for the electric manipulation of particles in organic or organofluorine solvents – common carrier fluids for droplet-based microfluidics.

1.2.3 Particle Material

CCEP can be used to manipulate electrically conductive particles that can charge and discharge upon contact with the electrodes (or other particles). Examples include metallic or metal-coated colloids, aqueous droplets[94, 114, 174, 113, 103, 4, 102, 105], hydrogel particles [58], and even suspensions of living cells [104]. CCEP of dielectric particles is also possible [52]; however, particle charging occurs much more slowly through a different mechanism (presumably contact electrification [11, 11]). We limit our discussion to conductive particles in insulating fluids, for which CCEP time scales are much longer than the charge relaxation time of the particle but much shorter than that of the fluid.

1.2.4 Electrodes

The electrodes can be fabricated from any conductive material including metals, hydrogel electrolytes, or even aqueous solutions[174]. In contrast to EP and DEP, CCEP requires direct (electrical) contact between the particle and the electrode surface to allow for particle charging / discharging. Once charged, however, a particle can be manipulated "remotely" via traditional EP. Notably, the surface charge acquired by contact charging is much larger than that acquired spontaneously, resulting in large electrophoretic mobilities. The characteristic surface potential due to the applied field, aE_0, is often three orders of magnitude larger than the thermal potential, k_BT/e. Phenomena due to thermal motions such as the diffuse double layer and the particle zeta potential are invariably neglected.

1.2.5 Continuous Motion

Most importantly, CCEP allows for continuous particle motion using constant voltages; the particle shown in Figure 1.1e will "bounce" indefinitely as long as the voltage is maintained. In this sense, CCEP is similar to a DC electric motor, which converts electrical energy into sustained motion. By contrast, DEP of a polarizable particle in an electric field gradient relaxes to a steady equilibrium state: the particle moves to the region of highest (or lowest) field strength and stops. Similarly, in electrophoresis, a charged particle moves from one electrode to the other and stops. As discussed below, the ability to achieve continuous motion using CCEP can lead to rapid particle transport, whereby strong electrostatic forces drive steady motions perpendicular to the field over long distances.

1.2.6 Low Power Operation

CCEP converts electrical energy into mechanical motion with high efficiency to enable rapid particle motions at low input power. The electric current through the circuit is due almost entirely to the motion of the charged particle. For a single particle, the average current scales as $I \sim qU/L$ and the input power as $P \sim IV_0$, which is of order $10 nanoWatts$ for a 30mm sphere oscillating at 500Hz [54]. Little or no energy is wasted in the absence of particle motion. By contrast, EP requires large faradaic currents to maintain steady electric fields within conductive liquids; these currents lead to significant dissipative losses even in the absence of particle motion [81]. The low power requirements of CCEP is attractive for use in portable microfluidic systems.

1.2.7 Scalability

Like other forms of electrostatic actuation, CCEP is highly amenable to miniaturization. For a constant applied voltage, the electrostatic force depends the ratio between the particle size and the electrode separation, $F_E \propto (a/L)^2$. By holding this ratio constant, the size of the system can be reduced without altering the magnitude of the electric force driving particle motion. By contrast, viscous drag and short-ranged surface forces (e.g., van der Waals) scale linearly with size [106]; they decrease in magnitude as the system is miniaturized. As a result, the particle velocity actually increases as the size of the system is decreased – that is, $U \propto a^{-1}$ for constant a/L and V_0. For example, we've observed that the particle velocity increases from ~7mm/s to more than 100mm/s as its diameter is reduced from $13\mu m$ to $1.5\mu m$. These scaling laws highlight the potential of CCEP for actuation at the micro- and nanoscales.

1.3 Fundamentals of CCEP

The charging of a conductive particle on contact with a biased electrode and its subsequent motion in the field are well described by a combination of classical electrostatics [128, 107] and low Reynolds number hydrodynamics [92, 118]. In this section, we discuss the physics underlying the processes of contact charging and particle motion. In addition to the well-studied case of a single sphere moving between parallel electrodes [54], we highlight recent work on the study of asymmetric particles and of many interacting particles.

1.3.1 Contact Charging

1.3.1.1 Thermodynamics of Charging

When a conductive particle makes electrical contact with an electrode surface, charge flows to/from the particle until electric equilibrium is achieved. At equilibrium, the electric potential difference between the particle and the electrode is equal to the contact potential difference characteristic of the two materials. This finite potential difference is often neglected due to the comparatively large voltages applied in CCEP experiments (typically, $10^2 - 10^4$ V). The charge acquired by the particle can be estimated by first solving the Laplace equation for the electric potential ϕ within the dielectric fluid

$$\nabla^2 \phi = 0, \tag{1.1}$$

subject to the follow conditions at the surfaces of the respective conductors

$$\phi(\boldsymbol{x}) = 0 \text{ for } \boldsymbol{x} \in \text{particle, electrode 1}, \phi(\boldsymbol{x}) = V_0 \text{ for } \boldsymbol{x} \in \text{electrode 2}. \tag{1.2}$$

The net charge on the particle is then obtained by integrating the surface charge density over the particle surface

$$q = \int_{S_p} -\varepsilon \boldsymbol{n} \cdot \nabla \phi dS, \tag{1.3}$$

where $\boldsymbol{n}$ is the unit normal vector directed out from the particle surface. For a conductive sphere in contact with a plane electrode and subject to an applied field E_0, the charge can be computed analytically to obtain [141, 182, 71, 44]

$$q_m = \frac{2}{3}\pi^3 \varepsilon a^2 E_0. \tag{1.4}$$

We refer to this result as the *Maxwell charge* as it was first obtained by Maxwell for the closely related problem of two contacting spheres [141]. The presence of a second co-planar electrode separated by a distance L results in an additional contribution of order $(a/L)^3$, which is typically neglected when $L \gg a$ [56].

The Maxwell charge of equation (1.4) is often considered as the "ideal" charge expected for a particle undergoing CCEP, and its accuracy has been evaluated for a variety of systems. Experimental measurements on solid conductive spheres generally agree with the theory [37, 40, 112, 200, 117, 122]; however, systematic deviations have been observed under certain conditions. In particular, micron-scale particles moving though viscous liquids at low Reynolds numbers ($\mathrm{Re} = \rho a U/\eta \ll 1$) acquire less charge than predicted by equation (1.4) [122, 54] (see below). For liquid droplets, a meta-analysis of recent literature showed that droplets regularly acquire more positive than negative charge [67]; such anomalous charging behavior has been attributed to perturbations in the applied field (e.g., due to charging of dielectric surfaces) [216]. Recent advances in measuring the charge acquired by particles during CCEP should

help to identify and resolve remaining discrepancies between theory and experiment [67].

1.3.1.2 Kinetics of Charging

When a charged particle approaches an oppositely biased electrode, the electric field in the particle-electrode gap increases inversely with the size of the gap δ as $E_{\max} \sim aE_0/\delta$ [54]. For small gaps ($\delta \ll a$), the local field becomes much greater than the applied field, eventually exceeding the dielectric strength of the fluid. The resulting spark or microdischarge [200, 66] creates a conductive pathway between the two surfaces prior to mechanical contact. For millimeter-scale particles or water drops, these discharges can be observed as flashes of visible light and are further evidenced by the formation of micron-scale craters on the electrode surface due to local melting [66]. The degradation of the electrode surface by repeated contact charging may contribute to deviations between the measured particle charge the predicted Maxwell charge. For a constant applied field, the diameter of the crater d is predicted to scale with the particle radius a and the electrode separation L as $d \propto (qV_0)^{1/3} \propto a^{2/3}L^{1/3}$ – smaller particles produce smaller craters[66].

The CCEP motion of micron-scale particles (e.g., $a \sim 10$mm) is characterized by low Reynolds numbers at which the inertia of the fluid and the particle are negligible. Under these conditions, particles can approach the electrode surface, transfer charge, and move away without ever making mechanical contact with the surface (Fig. 1.2). This putative mechanism is supported by experimental measurements of CCEP motions and the accompanying electric current combined with detailed theoretical predictions [54]. At low Reynolds numbers, changes in the particle charge and thereby

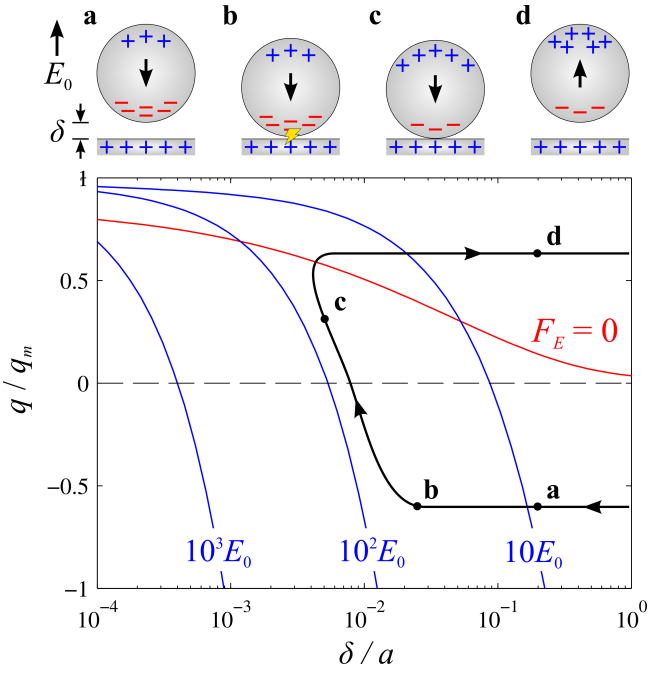

Figure 1.2: Qualitative particle trajectory (black) through the position-charge phase space. The surface separation δ is scaled by the particle radius a; the sphere charge q is scaled by the Maxwell charge q_m of equation (1.4). The blue curves show lines of constant electric field $E_{\max}$ within the sphere-electrode gap as multiples of the applied field, E_0. The red curve shows the line of zero electric force: $F_E < 0$ below the line and $F_E > 0$ above. (Adapted from reference [54]; copyright 2015 American Chemical Society.)

the electric force result in almost immediate changes in the particle velocity. Following the initiation of a microdischarge but prior to mechanical contact (Fig. 1.2b), the charge on the particle begins to relax to its new equilibrium value. Prior to reaching equilibrium, however, the electric force on the particle reverses direction, thereby increasing the surface separation and extinguishing the electric discharge. As a result, the charge on the particle is typically 60-80% less than that expected at equilibrium [54].

Charge transfer at finite surface separations ($\sim 0.1mm$ for a 10mm sphere[54]) suggests that surface forces between the particle and the electrodes play a minimal role in *sustaining* CCEP motions: the particle can oscillate between the two electrodes without ever making mechanical contact with either surface. However, these forces are likely relevant in *initiating* particle motions – especially at lower voltages. To initiate CCEP motion, the electrostatic force must exceed the adhesion force (see below). Consistent with this hypothesis, we have observed that the minimum voltage required to initiate CCEP motions is greater than that required to sustain such motions.

1.3.2 Particle Dynamics

Once sufficiently charged, particles move in the electric field as determined by the balance of electrostatic and hydrodynamic forces and torques (Fig. 1.3a). The movement of the charged particle acts to redistribute charge on the electrodes, producing measurable currents in the external circuit (Fig. 1.3b). One distinguishing feature of CCEP motions is the asymmetry of particle-electrode "collisions". Particles approach the electrode at a near constant velocity but depart slowly, accelerating to a constant velocity on time scales of order $\eta/\varepsilon E_0$. These and other experimental trends are captured quantitatively by the following models.

1.3.2.1 Electrostatic Forces & Torques

A charged conductor in a dielectric fluid experiences an electric force $\boldsymbol{F}_E$, which can be calculated by integrating the Maxwell stress over the particle surface

$$\boldsymbol{F}_E = \int_{S_p} \frac{1}{2}\varepsilon E^2 \boldsymbol{n} dS, \tag{1.5}$$

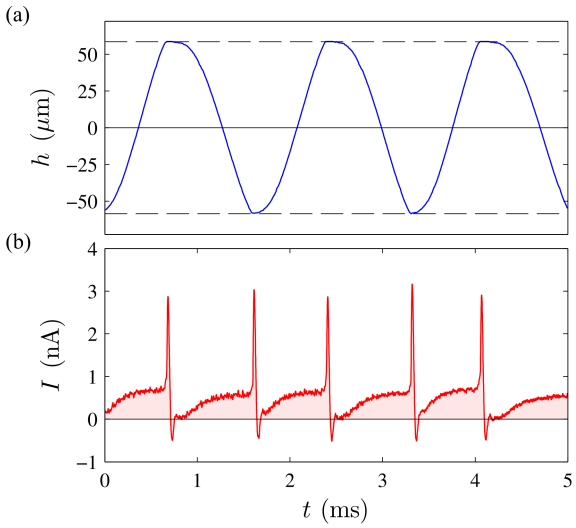

Figure 1.3: Synchronized particle trajectory $h(t)$ and electrical current $I(t)$ for a 28 μm sphere moving through mineral oil between two electrodes separated by a distance $L = 145\mu m$ and energized by a voltage $V_0 = 765V$. (Reproduced from reference [54]; copyright 2015 American Chemical Society.)

where $\boldsymbol{E} = -\nabla\phi$ is the electric field. This exact expression is often approximated by decomposing the field into two contributions: that due to charge on the particle $\boldsymbol{E}_p$ and that due to charge on the electrodes (and other particles) $\boldsymbol{E}^\infty$. By expanding the particle field in a multipole expansion, the above integral can be expanded as

$$\boldsymbol{F}_E = q\boldsymbol{E}^\infty + \boldsymbol{p}\cdot\nabla\boldsymbol{E}^\infty + \ldots, \tag{1.6}$$

where $\boldsymbol{p}$ is the particle dipole moment. The first two terms in the expansion correspond to the electrophoretic and dielectrophoretic forces, respectively, within an dielectric fluid.

As CCEP motions involve repeated contact between the particle and the electrodes, it is often necessary to include contributions due to higher order moments of the particle charge implicit in equation (1.5) to obtain an accurate description. Complete analytical solutions are available for a spherical particle near a plane electrode [44, 180, 108]. These solutions reveal a striking asymmetry between the approach of a charged particle to an oppositely biased electrode and its departure from that electrode after charge transfer [56]. In particular, the force on a positively charged sphere ($q = q_m$) departing the positively biased electrode is

$$F_E = 0.832 q_m E_0 + O(\xi) \quad \text{(departing)}, \tag{1.7}$$

where q_m is the Maxwell charge of equation (1.4), and $\xi = \delta/a$ is the dimensionless surface separation [180]. The reduction in the force from the expected value of $q_m E_0$ is due to the attraction of the charged sphere to its image in the nearby electrode. By contrast, the force on a negatively charge sphere ($q = -q_m$) approaching the same positively biased electrode is

$$F_E = -\frac{6.58}{\xi f^2(\xi)} q_m E_0 + O(\ln\xi) \quad \text{(approaching)}, \tag{1.8}$$

where $f(\xi)$ is a slowly varying logarithmic function [56]. The force increases asymptotically with decreasing separation as ξ^{-1}. It is this asymmetry in the electrostatic force that causes the asymmetric particle trajectories observed in experiment (Fig. 1.3a).

Even when analytical solutions are unavailable, there exist efficient simulation techniques based on Stokesian dynamics that accurately capture both the far field and near field contributions to the electrostatic interactions [23, 19, 56]. Bonnecaze and Brady applied this approach to describe the electrostatics of many, spherical particles interacting in an unbounded medium [19]. More recently, we considered the case of a single sphere bounded by two plane electrodes – the prototypical CCEP geometry [56]. A logical next step is the integration of these approaches to describe the dynamics of many particles moving between two electrodes. For non-spherical particles, one must turn to more general (but less efficient) numerical methods such as finite element solvers to compute the relevant electrostatic forces [52].

Non-spherical particles also experience an electric torque about the particle center $\boldsymbol{x}_p$ defined as

$$\boldsymbol{L}_E = \int_{S_p} \frac{1}{2}\varepsilon E^2(\boldsymbol{x}-\boldsymbol{x}_p)\times \boldsymbol{n} dS. \tag{1.9}$$

To first order, this torque can be approximated as the cross product between the dipole moment and the field,

$$\boldsymbol{L}_E = \boldsymbol{p}\times \boldsymbol{E}^\infty + \dots. \tag{1.10}$$

The dipole moment on a conductive particle is a linear function of the field: $\boldsymbol{p} = q(\boldsymbol{x}_q - \boldsymbol{x}_p) + \boldsymbol{\alpha}\cdot\boldsymbol{E}^\infty$, where $\boldsymbol{x}_q$ is the center of charge, and $\boldsymbol{\alpha}$ is the symmetric polarizability tensor [128]. Note that the particle center $\boldsymbol{x}_p$ (e.g., the center of hydrodynamic reaction [26]) need not coincide with the center of charge $\boldsymbol{x}_q$. Physically, particles

rotate to induce the largest dipole moment aligned with the field. As discussed below, these rotational motions can serve to rectify CCEP oscillations and drive steady motions of asymmetric particles.

1.3.2.2 Hydrodynamic Drag

At low Reynolds numbers, the electrostatic forces and torques are balanced by equal and opposite hydrodynamic forces $\boldsymbol{F}_H$ and torques $\boldsymbol{L}_H$ due to motion of the particle through its viscous surroundings. Owing the linearity of the Stokes equations governing fluid motion, the hydrodynamic forces and torques are linearly related to the translational and rotational velocities of the particle(s) [119]. The so-called resistance (or mobility) tensors relating these quantities depend on the position and orientation of the particle(s) relative to the bounding electrodes. In general, these tensors must be computed numerically by integrating the Stokes equations subject to no-slip conditions at the surfaces of the particle(s) and electrodes. However, there are few special geometries relevant to CCEP dynamics, for which analytical solutions and/or efficient numeric solutions are available.

Arguably, the most important case is that of a sphere moving in an unbounded fluid; the hydrodynamic drag is given by Stokes' law [190]

$$\boldsymbol{F}_H = -6\pi\eta a\boldsymbol{U}. \tag{1.11}$$

This expression provides a useful approximation when the particle is separated from either electrode by many particle radii. When the particle is near either electrode, the hydrodynamic resistance increases significantly due to fluid flow into or out from the particle-electrode gap. These effects are accurately captured by analytical solutions

for a solid sphere moving near a solid plane boundary [109, 25, 153, 47]. Of particular interest is motion normal to a plane surface, for which equation (1.11) is modified by a multiplicative factor $\lambda(\xi)$ that depends on the surface separation $\xi = \delta/a$ [25]. For small separations ($\xi \ll 1$), the resistance increases as $\lambda = \xi^{-1} + \ln(\xi)$. When a charged particle approaches contact with an electrode, the increase in the hydrodynamic resistance is almost exactly balanced by a similar increase in the electric force (see equation (1.8)). Upon charging, however, the electric force is greatly reduced (see equation (1.7)), and the particle moves slowly to escape from the electrode surface.

Even at large separations, the approach to Stokes' law occurs slowly as $\lambda = 1 + \frac{9}{8}\xi^{-1}$ due to long range hydrodynamic interactions with the wall. In general, such interactions with the bounding electrodes and other particles are not pairwise additive. Accurate treatments require efficient techniques such as Stokesian dynamics to capture the many body interactions between the particle(s) and the electrodes as well as the lubrication forces near contacting surfaces [191, 193, 194].

1.3.2.3 Other Forces: Gravity, Inertia, Adhesion

The above analysis of particle motions neglects several forces that can be relevant to CCEP depending on the experimental conditions. The significance of these forces can be assessed by comparing their magnitude to that of the electric forces driving CCEP motions, $F_E \sim 4\pi\varepsilon a^2 E_0^2$. Forces due to gravity and inertia scale as the particle volume and are therefore significant for larger particle sizes. As an example, we consider the motion of a steel sphere ($\rho_p = 8000 kg/m^3$) in mineral oil ($\rho = 840 kg/m^3$, $\eta = 0.027 Pa/s$, $\varepsilon = 2.5\varepsilon_0$) due to an applied field of $E_0 = 2V/\mu m$. The gravitational force $F_G \sim \frac{4}{3}\pi a^3(\rho_p - \rho)g$ becomes comparable to the electric force only for millimeter-

scale particles. Similarly, forces due to particle inertia $F_I \sim \frac{4}{3}\pi a^3 \rho_p U^2/a$ become significant for particle sizes of order 100 mm or larger [122].

By contrast, forces due to surface adhesion scale with the linear dimension of the particle and are therefore significant for smaller particle sizes. In the Hamaker approximation, the van der Walls force between a sphere and a plane scales as $F_{vdW} \sim aA/6\delta^2$ where A is the Hamaker constant [106]. Continuing the example above, this force is comparable to the electric force for 10 μm particles, assuming $A = 10^{-19J}$ and $\delta = 1nm$ [106]. When the electric force is smaller than adhesive surface forces, the particle remains "stuck" to the electrode surface. A finite "lift-off" voltage is therefore required to initiate particle motion [117, 122]. As the particle size decreases, larger electric fields are required to induce CCEP motions. Notably, by increasing the field to $E_0 \approx 16V/\mu m$, we were able to drive the motion of a 1 mm gold sphere between two gold wires at speeds of 100 mm/s (10^5 body lengths per second). The application of larger fields is limited by the dielectric strength of the fluid; however, it may be possible to manipulate smaller particles by tailoring their surface chemistry to mitigate adhesion. Further study is required to investigate the role of surface forces in initiating and sustaining CCEP motions.

1.3.3 Dynamics of Anisotropic Particles

The motion of spherical particles is relatively simple due to the absence of electric torques and the symmetry of the resistance tensor. The motion of anisotropic particles is considerably more complex – even in uniform fields and unbounded fluids. Here, we discuss the dynamics of two specific particle types: a conductive rod and a Janus sphere with a conductive hemispherical cap [52]. The generalization of these

specific examples to describe the motions of other particle shapes and symmetries is an interesting topic for further study.

1.3.3.1 Preferred Orientations

When subject to a uniform electric field, an uncharged conductive particle of anisotropic shape adopts a preferred orientation that maximizes the particle's dipole moment. Conductive rods rotate to align their long axis parallel to the applied field; Janus spheres rotate to align their axis perpendicular to the applied field (Fig. 1.4a). The addition of charge to the rod does not influence its preferred orientation but causes it to move parallel to the field. In this case, the particle's center of charge and its center of hydrodynamic reaction [26] are one an the same. By contrast, the center of charge on the Janus particle is displaced from the center of the sphere towards the conductive cap. As a result, the addition of charge to the Janus sphere alters its dipole moment an thereby its preferred orientation. Figure 1.4a shows the stable orientation of the Janus particle as a function of the charge q on its conductive hemisphere. Importantly, the dipole moment due to charge acquired by contact charging is comparable to that due to polarization (i.e., $qa \sim p$ when $q \sim 4\pi\varepsilon a^2 E_0$ and $p \sim 4\pi\varepsilon a^3 E_0$)[107]. As a result, the particle adopts a stable orientation with its axis oblique to the applied field. Moreover, as the particle oscillates between two electrodes, its orientation also oscillates between two stable values.

1.3.3.2 Rectified Motions

CCEP oscillations of Janus particles between parallel electrodes are accompanied by steady motions directed perpendicular to the applied field [52] (Fig. 1.4b). These lat-

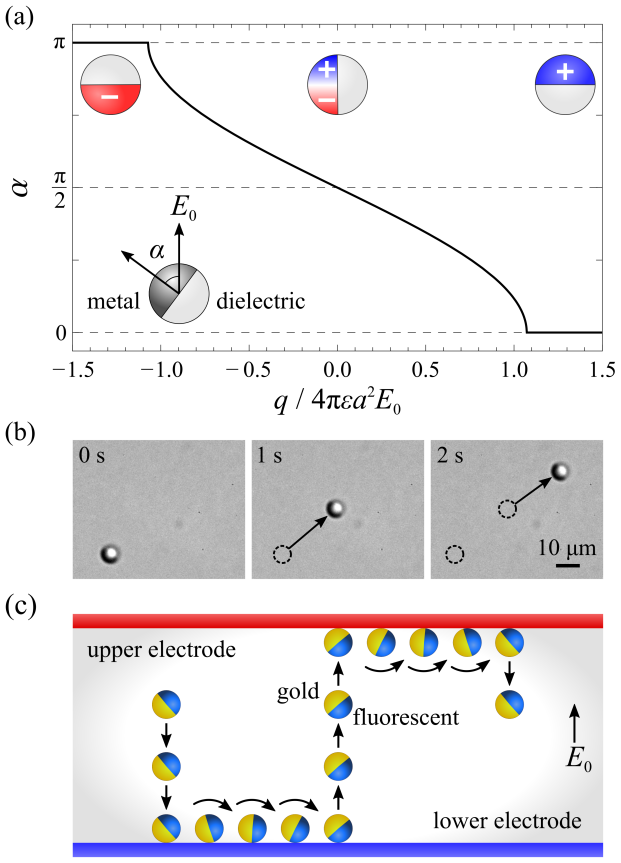

Figure 1.4: (a) Stable orientation α of a metallodielectric Janus sphere in a uniform electric field depends on the particle's charge q. Uncharged particles align perpendicular to applied field E_0; highly charged particles align parallel to the field. (b) Top view of a gold-silica Janus sphere oscillating between two transparent electrodes. Over many oscillation cycles, the particle moves in the direction opposite its conductive hemisphere. (c) Illustration of the propulsion mechanism showing one oscillation cycle. (Adapted from reference [52]; copyright 2016 American Chemical Society.)

eral motions are caused by successive particle rotations following each charge transfer at the electrode surface (Fig. 1.4c). Each time the particle contacts an electrode, its charge changes sign, thereby altering its preferred orientation in the field. The field-induced rotation of the particle in the vicinity of the electrode surface results in a lateral displacement, which is qualitatively similar to that of a sphere "rolling" along the surface. Successive rotations occur in a common direction toward the non-metallic hemisphere, causing a steady motion over the course of many oscillations. This mechanism is supported both by experiments with fluorescent particles that reveal their rotational motions and by simulations of CCEP dynamics that capture the electrostatic and hydrodynamic forces and torques outlined above. This strategy for rectifying particle oscillations to achieve directed motion is not limited to Janus spheres. Similar motions are observed for other anisotropic particles (e.g., clusters of spherical particles); however, further work is needed to understand and optimize particle shapes to maximize directed motion.

1.3.4 Dynamics of Multiple Particles

The vast majority of CCEP studies have focused on the dynamics of individual particles, and there remains much to explore when many particles move and interact with one another. Particles interact over large distances through both electrostatic and hydrodynamic forces. Additionally, particle "collisions" can serve to redistribute charge among particles in contact. To date, these effects have been shown to guide the formation of dynamic chains (so-called bucket brigades[165]), the synchronization of neighboring oscillators [142], and the emergence of collective motions[52].

1.3.4.1 Bucket Brigades

The phrase "bucket brigade" refers to a method of transporting items wherein items are passed from one stationary member of the "brigade" to the next. A conceptually similar behavior occurs during CCEP of multiple particles, which organize to pass charge from one electrode to the other. In one realization, multiple aluminum discs were distributed randomly on the surface of a dielectric liquid between two electrodes (Fig. 1.5a) [165]. Upon application of the field, the discs organized to form linear chains which oscillated continuously passing charge from neighbor to neighbor. Similar behaviors have been observed for water drops moving in oil between two electrodes [174]. Importantly, the number of particles in the chain cannot exceed $L/2a$; otherwise, they will span the gap between the electrode and short the circuit.

We have observed similar chains of spheres moving in mineral oil between two electrodes. Interestingly, particles appear to collide "elastically" despite the absence of inertia at low Reynolds numbers (Fig. 1.5b). During a collision between two spheres, the total charge is conserved and redistributes between the spheres to achieve a common electric potential. The amount of charge acquired during a sphere-sphere collision is the same as that acquired by contact with either electrode [46, 107]. These dynamical behaviors are well captured by Stokesian dynamics simulations of CCEP motions that incorportate the electrostatic and hydrodynamic contributions detailed above.

1.3.4.2 Synchronization

Prior to the formation bucket brigades, neighboring particles moving by CCEP begin to oscillate with a common frequency – that is, they synchronize[142]. Unlike many

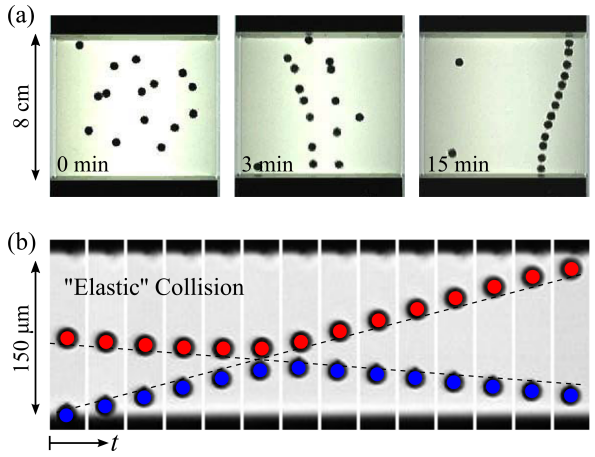

Figure 1.5: (a) Dynamic formation of a "bucket brigade" of aluminum disks in a $E_0 = 0.3V/\mu m$ field. (Reproduced from reference [165]; copyright 2014 IEEE Computer Society.) (b) Successive images of two spheres colliding "elastically" at lows Reynolds numbers; the time between successive images is 40 ms.

types of coupled oscillators which move in phase, CCEP oscillators prefer to move in an anti-synchronous fashion with a phase difference of 180°. As a result, the two particles always have charge of opposite polarity and attract one another. These synchronized Coulombic interactions along with dipole-dipole forces are ultimately responsible for the organization of dynamic particle chains. Unfortunately, the synchronization of dynamic assemblies by CCEP is limited by the particles' propensity to form chains that span the electrodes and short the circuit. Short circuits can be eliminated by constraining particle motions along dielectric "tracks", which do not interfere with the electrostatic interactions driving synchronization. The exploration of synchronization and dynamic pattern formation among CCEP oscillators is exciting direction for further study – both for its interesting physics and its potential relevance in coordinating the motions of many particles for useful functions (see below).

1.4 Microfluidic Applications

The attributes of contact charge electrophoresis make it potentially attractive for powering the active unit operations of microfluidic devices using portable battery power. Despite their small size, "lab-on-a-chip" (LoC) devices are often accompanied by bulky external equipment used for fluid transport[129], mixing[150], and detection[136]. This lack of self-containment can limit the use of LoC devices in point-of-care diagnostic systems, which seek to address health care challenges in regions without centralized medical facilities [82, 88]. The development of mobile microfluidic platforms for fast, accurate, and inexpensive medical diagnostics remains an important challenge for global health [205]. To help address this need, we have developed CCEP-based systems for rapid particle transport [58, 30], separations [58], and fluid mixing [32]. These demonstrations motivate the pursuit of other microfluidic operations such as pumping fluids and controlling heat/mass transfer via CCEP motions.

We note that the low power requirements of CCEP do not imply low voltage operation directly accessible by standard battery technologies. The unit operations below rely on relatively high voltages (typically, $10^2 - 10^3 V$) to achieve maximum performance. Such voltages are readily supplied by miniature, battery-powered amplifiers [69], which are ca. 1 cm^3 in size and commercially available. These amplifiers are commonly used to improve the performance of on-chip electrophoretic separations which benefit from high voltages ($\sim 10^3 V$) but require little current ($\sim 1\ \mu A$, as in capillary electrophoresis [80]).

1.4.1 Ratcheted Transport

Most studies of CCEP have been limited to simple oscillatory motions between two electrodes. To realize the full potential of this mechanism (e.g., for particle transport or droplet manipulation), effective strategies are required for rectifying particle oscillations to achieve directed linear or rotational motions.

We developed one such strategy that uses ratcheted microfluidic channels to direct CCEP motions perpendicular to the applied field [58]. As illustrated in Figure 1.6, the oscillatory motion of a conductive particle between two parallel electrodes can be biased by a series of inclined dielectric barriers ("teeth") that translate the electric force in the "vertical" direction into directed motion along the "horizontal" direction. This microfluidic ratchet is fabricated in polydimethylsiloxane (PDMS) using soft lithography [213]. To create electrodes that connect directly to the center channel, we flow liquid gallium (at 40°C) into the electrode channels using capillarity to prevent flow into the center channel [184]. After cooling to solidify the electrodes, we flow in particles suspended in mineral oil, apply a DC voltage between the two electrodes, and monitor the motion of the particles using a high speed camera. Remarkably, this CCEP ratchet allows for rapid particle transport (velocities of few cm/s) over arbitrary distances using DC voltages and very low power (typically, $\sim$1 nW). By contrast, DEP requires complex electric fields that vary in space and time (e.g., traveling wave DEP [89, 147]) to achieve comparable performance.

The same approach also enables the rapid transport of hydrogel capsules and aqueous droplets, which can serve as containers for chemical and biological cargo. We recently described how CCEP can be used both to generate and transport aque-

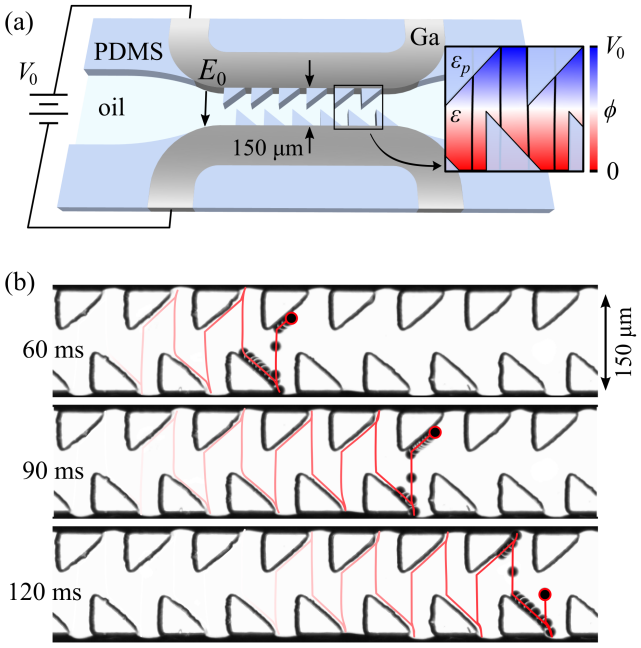

Figure 1.6: (a) Ratcheted microfluidic channel for directed particle transport. As the dielectric constant of PDMS is similar to that of mineral oil, the applied electric field remains nearly uniform throughout the interelectrode region (inset). (b) Reconstructed particle trajectories show the directed motion of a single 20 μm particle (silver coated glass sphere) for $E_0 = 4.6V/\mu m$. Each image is a composite of 16 individual frames collected at intervals of 0.67 ms; the position of the shuttle at each of those 16 time points is denoted by the black circle. The red line traces the shuttles trajectory in time. The speed of the particle through the fluid is 50,000 mm/s; the average speed of the particle in the horizontal direction is 5,000 mm/s. (Reproduced from reference [58] with permission of The Royal Society of Chemistry.)

ous droplets within a microfluidic system powered by a single, constant voltage input [30]. Drop generation is achieved through an electrohydrodynamic dripping mechanism by which conductive drops grow and detach from a grounded nozzle in response to an electric field. The now-charged drops are then transported down the ratcheted channel by CCEP in a manner similar to that of solid particles. By contrast, however, drops can deform in response to electric stresses acting at their surface. Such deformations are opposed by surface tension, which favors spherical drops that minimize the interfacial area. Ratcheted transport of drops requires sufficiently small capillary numbers (typically, $\mathrm{Ca} = \varepsilon E_0^2 a/\gamma < 1$), which limits the magnitude of the applied field and thereby the speed of drop transport.

1.4.2 Separations

The use of dielectric barriers to direct CCEP motions can be generalized to perform other functions such as separating and collecting particles[58]. This approach is illustrated in Figure 1.7, which shows a ratcheted microfluidic system for the separation of particles from a fluid stream. In the design process, we start with the desired functionality – particles will enter from channel 1 and exit from channel 2 – and choose the positon and polarity of the electrodes to ensure that the particle will only oscillate in the appropriate channels (e.g., not in channel 3; Fig. 1.7a). We then calculate the electric field between the electrodes for the proposed geometry using a finite element solver (Fig. 1.7b). Provided the dielectric constants of the PDMS barriers are similar to that of the fluid, the electric field lines will not be affected by the placement of the dielectric teeth.

The design of the dielectric barriers is guided by three heuristic rules for predicting

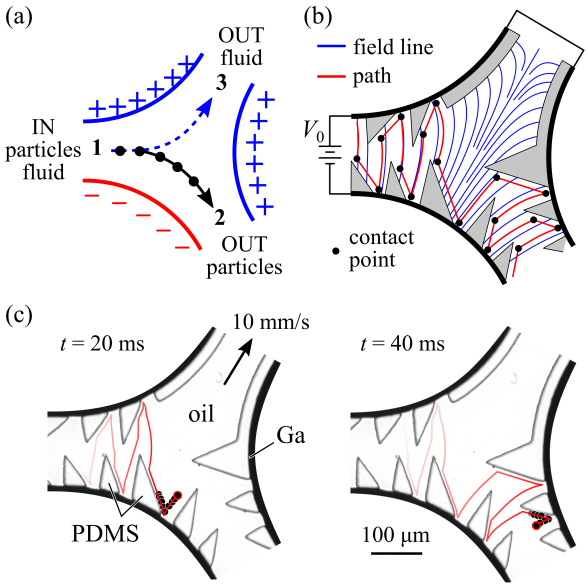

Figure 1.7: (a) Ratcheted CCEP system for separating particles from a fluid stream. (b) Schematic illustration showing the dielectric barriers (grey), electrodes (black), electric field lines (blue), and the anticipated particle trajectory (red). (c) Experimental realization of this design showing the dynamics of a 20 mm particle. The red line shows the reconstructed particle trajectory; the black circles denote the position of the particle at regular intervals of 0.2 ms. (Reproduced from reference [58] with permission of The Royal Society of Chemistry.)

particle motions: (i) a particle moves along the electric field lines until it contacts a surface, (ii) it slides / rolls along inclined dielectric barriers, and (iii) it reverses direction when it contacts an electrode surface. The key function of the dielectric barriers is to move a charged particle from one field line to another in programmed manner. With these rules, the PDMS teeth are designed by tracing field lines and adding barriers to direct particle motion. Implementing the design in a microfluidic system (Fig. 1.7c), we find remarkable agreement between the actual particle motion and that predicted by the simple heuristics [58].

Importantly, the rapid motion of particles via CCEP ($\sim$100 mm/s) effectively decouples their motion from that of the surrounding fluid ($\sim$1 mm/s); this enables particles to be transported upstream or downstream regardless of fluid flow [58]. Looking forward, we envision the development of CCEP-based transport systems for several useful applications including (i) the recycling of high-value catalyst particles in microfluidic reactors through "upstream" particle transport, (ii) capture and accumulation of particles in dead-end channels for isolation and analysis, as well as (iii) transport, manipulation, and merging of microfluidic droplets.

1.4.3 Mixing

The programmed transport of micron-scale particles within microfluidic systems can also be harnessed to rapidly mix laminar streams. Mixing two or more fluids within a microfluidic device can be challenging due to the absence of turbulence at low Reynolds numbers [155, 189]. Within laminar flows, mixing is achieved through molecular diffusion, which requires a characteristic time $\tau \sim \ell^2/D$ to homogenize the fluid composition over a length scale ℓ (here, D is the diffusion coefficient). Effective

mixers act to stretch and fold the flowing streams to reduce the length over which diffusion must act and accelerate the rate of diffusive mixing. Active microfluidic mixing using applied electric fields is often achieved through electrohydrodynamic flows [36, 93] caused by the action of the field on ionic space charge. While effective in aqueous systems, electrohydrodynamic mixers do not function in most organic fluids due to the absence of dissolved ions. By contrast, CCEP enables the rapid oscillatory movement of particles through dielectric fluids. These particle motions can be applied to mix organic liquids, which are used in the context of combinatorial syntheses and drug discovery[51, 149].

Figure 1.8 illustrates a simple mixer designed to mix two laminar streams [32]. Application of a DC voltage to the gallium electrodes creates a non-homogeneous electric field that enables the dielectrophoretic capture of a conductive particle, which then oscillates between the electrodes via CCEP. Perhaps surprisingly, we found that linear particle motions perpendicular to the direction of flow does not result in effective mixing due to the kinematic reversibility of low-Reynolds number flows [173, 92]. The mixing achieved by the "upward" movement of the particle is almost entirely reverse by its "downward" motion. By contrast, orbital particle motions guided by dielectric barriers (analogous to those used in the ratchets of the previous section) break the time-reversal symmetry and allow for effective mixing over lengths comparable to the width of the channel. Complete mixing requires that the speed of the particle be much larger than the fluid velocity such that the particle completes many orbits as the fluid flows through the mixing region. The extent of mixing also depends strongly on the size of the particle and the shape of its trajectory; effective mixers relied on larger particles (comparable to the size of the channel) moving along non-reciprocal

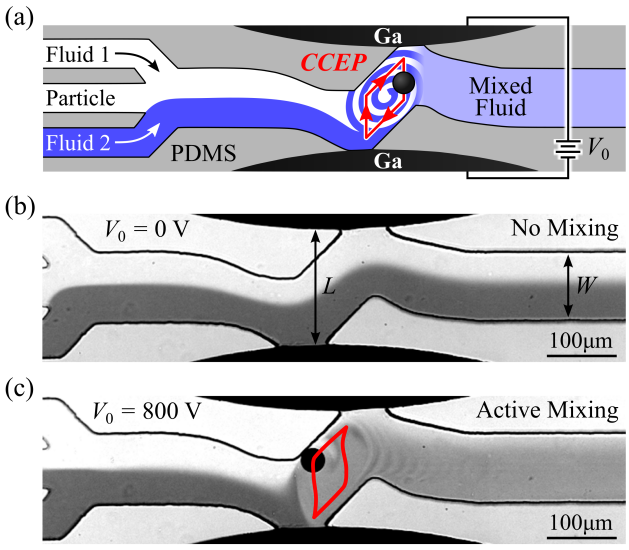

Figure 1.8: Schematic illustration of a microfluidic mixer based on CCEP. Two dielectric fluids (here, mineral oil with and without dye) flow laminarly into the channel and are mixed by the orbital motion of the particle. (b) Image of the mixer before introducing the particle and applying the electric field; the average fluid velocity is $u \approx 1$ mm/s. (c) Application of a constant voltage drives the oscillatory motion of the particle, which thoroughly mixes the two streams. The red curve denotes the particle trajectory. (Reproduced from reference [32] with permission of The Royal Society of Chemistry.)

orbits.

1.5 Future Directions

Contact charge electrophoresis is a promising technique for the electric manipulation of micron-scale particles and droplets. There remain outstanding opportunities to advance both our fundamental understanding of CCEP and our ability to apply it for microfluidic systems. More broadly, we recognize two frontiers for CCEP research: one based on further miniaturization to sub-micron dimensions, another based on the integration of many CCEP oscillators to form active, macroscopic materials. We close with a discussion of these complementary pursuits.

1.5.1 Go Smaller

Our study of CCEP was originally inspired by the catalytic nanomotors of Sen and Mallouk, who showed how electrochemical reactions could be harnessed to power the autonomous motion of colloidal particles [164]. Using catalytic materials, these nanoscale machines convert chemical energy from their surrounding environment into steady electric currents that lead to self-electrophoresis of the particles [210]. Importantly, only a tiny fraction of the chemical energy used is converted into the fluid flows that drive particle motions [208]. In this context, CCEP may provide an efficient electric motor, with which to realize the potential of chemically-powered colloidal machines. Of course, there remain many fundamental and technical challenges that must first be overcome.

CCEP motions described in the sections above were powered by large voltages –

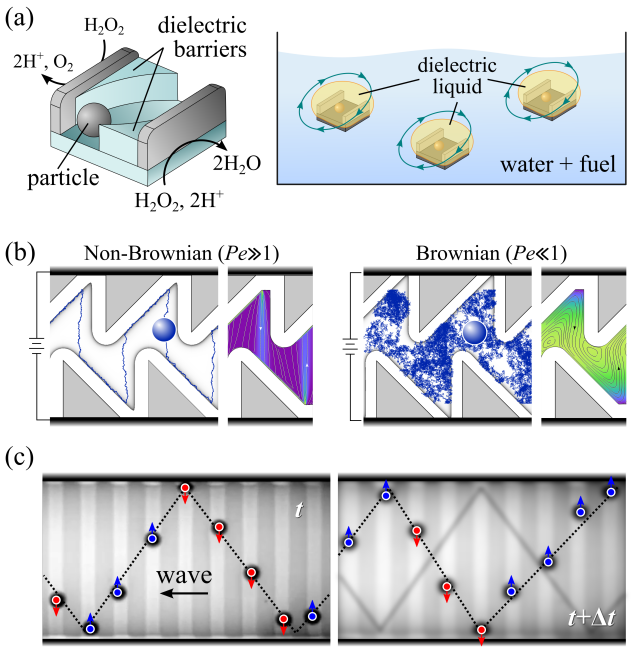

Figure 1.9: (a) Illustration of chemically powered, active emulsion droplets powered by CCEP. (b) Ratcheted CCEP transport is effective even at low Péclet numbers, $\mathrm{Pe} = aF_e/k_BT \ll 1$. Blue curves show individual particle trajectories; the colormaps and streamlines show the steady-state particle density and flux, respectively. (Reproduced from reference [125]; copyright 2016 AIP Publishing LLC). (c) Electrostatically coupled CCEP oscillators synchronize to form traveling waves capable of transport and actuation.

significantly greater than that provided by a single electrochemical reaction (ca. $0.1-1V$). Rapid particle motions are possible at these smaller voltages provided the electrode separation is also reduced to maintain large electric fields (ca. 1 V/μm). Perhaps the greater challenge is preventing particle adhesion at the electrodes, which becomes increasingly problematic at smaller scales (see above). There are two main strategies for reducing adhesive forces: change the surface chemistry and/or reduce the contact area. For example, by coating both the electrodes and the particle with a self-assembled monolayer of 1-octadecanethiol, we observed that the lift-off voltage for CCEP motion was reduced by a factor of $\sim$5. It is desirable to identify molecular surface coatings that both reduce adhesion forces and allow facile charge transfer on contact. Additionally, one can modify the geometry of the particle and/or electrode to reduce the contact area without significantly altering the electric forces driving CCEP motions. So-called "hedgehog particles" with an armor of rigid spikes are a particularly attractive candidate to investigate [7].

Another challenge is linking CCEP motions in dielectric fluids to autonomous functions in aqueous environments. One possible approach is to embed CCEP motors within emulsion droplets and rely on the hydrodynamic coupling of particle motions inside the drop to drive external flows (Fig. 1.9a). Such active droplets could convert chemical energy into motion with efficiency improvements of up to seven orders of magnitude over existing motors [208]. Dramatic improvements in the energy efficiency of colloidal machines could enable their autonomous operation in low fuel environments. In addition to improved efficiency, ratcheted transport using CCEP is predicted to be remarkably robust to Brownian motion [125]. Buffeted by an incessant assault of thermal noise, nanoscale ratchets continue to function effectively, in

sharp contrast other ratcheting mechanisms (Fig. 1.9b).

1.5.2 Go Bigger

At the other end of the spectrum, the collective motions of many CCEP oscillators may provide a basis for soft actuator materials inspired by biological muscle. Muscles are motors: they convert chemical free energy into mechanical motion and generate large forces through the steady repetition of small steps namely, those of myosin motor proteins. By orchestrating the coordinated action of these many elemental motors, living organisms perform a diverse range of mechanical functions. Similarly, the electrostatic and hydrodynamic interactions among arrays of CCEP oscillator can lead to self-organized motions such as traveling wave synchronization (Fig. 1.9c). The distributed actuation of many CCEP oscillators can be harnessed to perform useful mechanical functions such as cargo transport and locomotion.

In particular, the fabrication of oscillator arrays in soft, elastomeric materials could provide a basis for new types of actuator materials – so-called artificial muscles. Soft materials are readily deformed by electric stresses, which can vary in time due to motions of charged particles. In this way, traveling waves of particle motion can be translated into traveling waves of material deformation. Such self-organized deformations are potentially useful for driving the locomotion of soft robots (e.g., inchworm-type motions) at the scale of microns to millimeters [100, 175]. Like biological muscle, active materials based on many elemental actuators are robust to failure of individual components and allow for complex collective motions.

1.5.3 Coda

From its humble beginnings more than 250 years ago, the electrostatic motor and its colloidal analogs are well positioned to contribute to a new industrial revolution at the micro- and nanoscales. The realization of active microfluidic systems and colloidal machines[186] that organize in space and time to perform useful functions requires efficient mechanisms for converting energy into motion. Applied creatively, contact charge electrophoresis can be engineered to power an increasingly diverse set of mechanical operations that meets these needs.

Chapter 2

Dynamic modeling of Multiparticle contact charge electrophoresis in confined electro-rheological environment

2.1 Introduction

[1]A 250 year technology first introduced by a Scotch Benedictine monk Andrew Gordon to demonstrate continuous oscillation of a small metal sphere suspended via a silk thread between two electrified bells[206]. After its first conception by Andrew Gordon and improvements by Benjamin Franklin[75] this idea remained largely dormant for

[1]The material presented in this chapter is being prepared for submission to Physics of Fluids with permission from Shashank Pandey, Mikolaj Kowalik, Charles Cartier and Kyle J. M. Bishop. Author responsibilities were as follows: S.P. and K.J.M.B. developed the algorithms and performed simulations. All authors contributed to final text. Supplementary Information is available in appendix A.

couple of centuries, has reignited recently into a great way to power motion of particles at micro and nanoscales. This process of charging of particles by contact and their actuation by the electric field is called Contact charge electrophoresis[54, 14]. Over the years CCEP has evolved into powering mechanism for uses in simple microfluidic system that is capable of enabling steady generation and efficient transport of aqueous drops [34], dynamics of metallodielectric Janus particles moving via contact charge electrophoresis[52], simple and effective ratcheted microfluidic mixer that uses contact charge electrophoresis (CCEP) of a micron-scale particle to rapidly mix nonpolar liquids[33] and ratcheted electrophoresis of contact-charged particles allowing for high speed transport through microfluidic channels over large distances[59].

Despite several experimental studies dealing with CCEP, there are no computational many-body simulations that take into account the effect of confinement which drastically changes the property and dynamics of passive and active colloidal suspensions confined between pair of electrodes. A general method was proposed by Bonnecaze & Brady [20, 18] to predict the effective conductivity of an infinite, statistically homogeneous suspension of particles without considering effects of confinement. There approach closely followed the ideas of Stokesian dynamics[24] and extended it to an analogues electrostatic system. It captured both far-field and near-field electrostatic particle interactions accurately with no convergence difficulties. Introducing a capacitance matrix which relates the moments of charge with potential moments of the particles, where the moment expansion of the integral equation for the potential generates the far-field approximation to the capacitance matrix and the near-field effects are added via exact two-body interactions. Emergence of anisotropic particles in colloidal

science has lead to development of several methodologies for colloids with anisotropic dielectric properties include auxillary field simulation methods[135, 70, 162] which introduce local algorithm with a propagating field that evolve with its own intrinsic dynamics locally. Building on similar idea Iterative dielectric solver developed by Lujiten [212, 77] which utilizes Boundary Element Method to specifically tackle polarization of anisotropic particles with the multiple dielectric contrasts. BEM-based approach is effective for cases with sharp dielectric interfaces[215] compared to image-based approach suggested by Bonnecaze which performs robustly for isotropic and planar interfaces, furthermore BEM-based solver's accuracy and convergence rates are dependent on conditioning of BEM equations. Most computational methods are developed taking into account specific physical scenarios so as to keep the computational complexity low, which most general methods fail to achieve.

The effect of confinement in colloids for an electrostatic system has yet to be explored computationally, though confinement has been studied in detail for hydrodynamics. Most notable being the study by Swan & Brady[194] of low-Reynolds-number hydrodynamic forces on particles comprising a suspension confined by two parallel walls. Building on the accelerated Stokesian dynamics(ASD) approach with inclusion of wall-effects into the formulation. Another popular approach was developed for hydrodynamic interactions in suspensions of rigid particles in a half-space bounded by an infinite no-slip wall have been efficiently[8] simulated by Donev[187] using multiblob approach and recently for fully confined suspensions of rigid particles[188]. Describes a fingering hydrodynamic instability in a suspension of active rollers[48] including the effect of the wall on the hydrodynamic interactions. Considering only the RPY

tensor that captures the far-field hydrodynamic interactions but does not accurately model near-field hydrodynamics. Utilizing simple direct summation implemented in Graphical Processing Units (GPUs) parallelised PyCUDA[121] to compute the matrix vector product. Parallellization of GPUs[124] compensate the O(N^2) computational cost of this method. Fnite element method(FEM) and direct numerical simulations via Lattice blotzmann method(LBM) use discretization os sptial domain that inherent allows for inclusion of effect of confinement and arbitrary shape of particles when modeling particulate suspensions. In FEM discretized stokes equation are solved based on Galerkin's formulation and fields for velocity and pressure are computed on highly resolved structured/unstructured meshes. While numerical scheme for LBM involves fictious fluid elements that move around with a probability distribution function and collisions[96] are tabulated at lattice nodes. A comparative analysis of FEM, LBM and ASD was performed by Schlauch[177] concluding that for ASD since only integrals on the particle surfaces are evaluated, the method is fast and efficient when compared with FEM and LBM.

The study of suspensions and clusters of conductive passive and active particles in presence of two confining electrodes has become ubiquitous particularly for understanding the dynamics of Contact Charge Electrophoresis. So here we develop efficient numerical methods based on hybrid image-based approach with green's functions for performing many-body electro-rheological dynamic simulations of suspensions and clusters of electrically conductive colloidal particles dispersed in dielectric media. This approach removes the computational bottlenecks of traditional image-based approach and add contribution of confining electrodes.

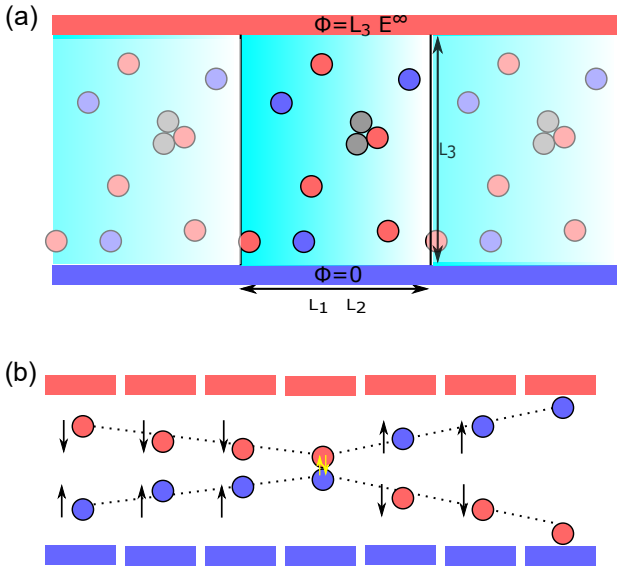

Figure 2.1: (a) Schematic of the simulation domain with periodic boundaries and random dispersion of conductive particles and semi-conductive cluster of particles sandwiched between two parallel plate electrodes with constant potential in a dielectric media. (b) When a set of particles approach contact with each other or with the walls they experience contact charging.

2.2 Model of CCEP Dynamics

2.2.1 Electrostatics

We consider a collection of conductive spheres of equal radius a dispersed in a viscous dielectric fluid between two parallel electrodes separated by a distance L_3. The electric

potential $\phi(\boldsymbol{x})$ in the dielectric is governed by the Laplace equation

$$\nabla^2\phi = 0, \tag{2.1}$$

subject to boundary conditions on the particle surfaces and the bounding electrodes. A constant potential difference is applied across the electrodes

$$\phi(\boldsymbol{x}) = 0 \quad \text{for} \quad x_3 = 0, \tag{2.2}$$

$$\phi(\boldsymbol{x}) = -L_3 E^\infty \quad \text{for} \quad x_3 = L_3, \tag{2.3}$$

where E^∞ is the applied field. At the surface of particle β (denoted $\mathcal{S}_\beta$), the potential is constant and equal to the particle potential Φ_β

$$\phi(\boldsymbol{x}) = \Phi_\beta \quad \text{for} \quad \boldsymbol{x} \in \mathcal{S}_\beta. \tag{2.4}$$

During its motion, the net charge on the particle remains constant between collisions and is given by the following integral over the particle surface

$$q_\beta = -\varepsilon \int_{\mathcal{S}_\beta} \boldsymbol{n} \cdot \nabla\phi d\mathcal{S}, \tag{2.5}$$

where ε is the permittivity of the fluid, and $\boldsymbol{n}$ is the unit normal vector directed into the fluid. Given the N-dimensional vector $\boldsymbol{q}$ of particle charges, the above equations can be used to determined the particle potentials $\boldsymbol{\Phi}$ and the potential $\phi(\boldsymbol{x})$ within the surrounding dielectric.

Each sphere experiences an electrostatic force that drives particle motion through the viscous fluid. The force $\boldsymbol{F}_\beta$ on particle β can be obtained by integrating the Maxwell stress over the conductive particle surface

$$\boldsymbol{F}_\beta = \frac{1}{2}\varepsilon \int_{\mathcal{S}_\beta} |\nabla\phi|^2 \boldsymbol{n} d\mathcal{S}, \tag{2.6}$$

Alternatively, the force can be computed by differentiating the electrostatic free energy $\mathcal{U}$ with respect to the particle position $\boldsymbol{x}_\beta$

$$\boldsymbol{F}_\beta = -\left.\frac{\partial \mathcal{U}}{\partial \boldsymbol{x}_\beta}\right|_{\boldsymbol{q},E^\infty}, \tag{2.7}$$

where the particle charges $\boldsymbol{q}$ and the applied field E^∞ (i.e., the electrode potentials) are held constant. The relevant free energy is given by

$$\mathcal{U} = \frac{1}{2}\varepsilon \int_V |\nabla\phi|^2 dV + QL_3E^\infty \tag{2.8}$$

where the integral is carried out over the volume of the dielectric, and Q is the net charge on the electrode at $x_3 = L_3$. The second term accounts for the electric work that is needed to maintain the potential difference between the two electrodes.[128, 54]

Rather than solve for the potential directly, we make use of the linear relation between the moments of the charge density and those of the potential on the particle surfaces[18]

$$\begin{bmatrix} \boldsymbol{q} \\ \boldsymbol{p} \end{bmatrix} = \begin{bmatrix} \boldsymbol{C}_{q\Phi} & \boldsymbol{C}_{q\Phi} \\ \boldsymbol{C}_{qE} & \boldsymbol{C}_{pE} \end{bmatrix} \cdot \begin{bmatrix} \boldsymbol{\Phi} - \boldsymbol{\Phi}^\infty \\ \boldsymbol{E}^\infty \end{bmatrix}. \tag{2.9}$$

Here, $\boldsymbol{\Phi} - \boldsymbol{\Phi}^\infty$ is an N-dimensional vector containing the particle potentials less the external potential evaluated at the particle centers $\boldsymbol{x}_\beta$ in their absence (e.g, $\Phi_\beta^\infty = -x_3^\beta E^\infty$ for sphere β). Similarly, $\boldsymbol{E}^\infty$ is a $3N$-dimensional vector containing the external electric field evaluated at the particle centers ($\boldsymbol{E}_\beta^\infty = E^\infty \boldsymbol{e}_3$). The $3N$-dimensional vector $\boldsymbol{p}$ contains the dipole moments of each sphere defined as

$$\boldsymbol{p}_\beta = -\varepsilon \int_{\mathcal{S}_\beta} (\boldsymbol{x} - \boldsymbol{x}_\beta)(\boldsymbol{n} \cdot \nabla\phi) d\mathcal{S}. \tag{2.10}$$

These quantities are related by the grand capacitance tensor $\boldsymbol{\mathcal{C}}$, which is symmetric and positive definite.[18] As detailed below, we use the Stokesian dynamics method to

estimate the capacitance tensor for a given particle configuration. Given the particle charges $\boldsymbol{q}$ and the applied field $\boldsymbol{E}^{\infty}$, we compute the particle potentials $\boldsymbol{\Phi}$ and dipole moments $\boldsymbol{p}$. With these quantities, the electrostatic energy $\mathcal{U}$ of equation (2.8) can be computed as

$$\mathcal{U} = \frac{1}{2}\boldsymbol{q} \cdot \boldsymbol{\Phi} + QL_3E^{\infty}. \tag{2.11}$$

Using this expression for the energy, the $3N$-dimensional vector of forces $\boldsymbol{F}$ is evaluated using equation (2.7).

2.2.2 Hydrodynamics

At small Reynolds numbers, these forces drive particle motion with linear velocities $\boldsymbol{U}$ and angular velocities $\boldsymbol{\Omega}$ as described by the linear relation[63, 194]

$$\begin{bmatrix} \boldsymbol{F} \\ \boldsymbol{L} \end{bmatrix} = \begin{bmatrix} \boldsymbol{R}_{FU} & \boldsymbol{R}_{F\Omega} \\ \boldsymbol{R}_{LU} & \boldsymbol{R}_{L\Omega} \end{bmatrix} \cdot \begin{bmatrix} \boldsymbol{U} \\ \boldsymbol{\Omega} \end{bmatrix}, \tag{2.12}$$

where $\boldsymbol{\mathcal{R}}$ is the grand resistance tensor. The electric torques $\boldsymbol{L}$ are zero for conductive spheres. The resistance tensor is approximated using the Stokesian dynamics method to determine the particle velocities. The particle positions evolve in time as

$$\frac{\partial \boldsymbol{x}_{\beta}}{\partial t} = \boldsymbol{U}_{\beta}, \tag{2.13}$$

where the velocity depends on the particle positions, the particle charges, and the applied field.

2.2.3 Contact Charging

When particles approach contact with one another or either electrode, the local electric field between the nearly contacting surfaces diverges, causing an electric discharge.

Charge flows rapidly between the two surfaces to equalize their respective potentials. Here, we assume that contact charging occurs instantaneously and to completion. For two spheres α and β, the new charges q'_α and q'_β are given by

$$\Phi'_\alpha = \Phi'_\beta \quad \text{and} \quad q'_\alpha + q'_\beta = q_\alpha + q_\beta, \tag{2.14}$$

where Φ' denotes the new potential after charge transfer. When a particle contacts either electrode, its potential is set equal to the electrode potential thereby specifying its new charge q'_β. In the simulations, we initiate charge transfer when particles approach closer than a critical surface separation δ—that is, when $|\boldsymbol{x}_\alpha - \boldsymbol{x}_\beta| < 2a + \delta$.

2.3 Simulation method

2.3.1 The grand potential tensor

We consider a collection of N charged, dielectric particles positioned within an uncharged, dielectric medium between two parallel electrodes of infinite extent. The particles are spherical in shape, and their respective charges are distributed uniformly throughout their interiors. The case of conductive spheres will be treated as a limiting case, in which the permittivity of the particles greatly exceeds that of the surrounding medium, $\lambda = \varepsilon_p/\varepsilon \to \infty$. The electric potential $\phi(\boldsymbol{x})$ in and around the particles can be expressed as

$$\phi(\boldsymbol{x}) - \phi^\infty(\boldsymbol{x}) = \sum_{n=1}^{N} \int_{V_n} \mathcal{G}(\boldsymbol{x}, \boldsymbol{x}')\rho_n(\boldsymbol{x}')d\boldsymbol{x}', \tag{2.15}$$

where $\phi^\infty(\boldsymbol{x})$ is the external potential, ρ_n and V_n are, respectively, the charge density and the volume of particle n, and $\mathcal{G}(\boldsymbol{x}, \boldsymbol{x}')$ is the relevant Green's function for the potential at position $\boldsymbol{x}$ due to a unit charge at position $\boldsymbol{x}'$ between two grounded

planes.[170] By expanding the Green's function in a Taylor series about the center of each particle and integrating over the particle surfaces, Bonnecaze & Brady[18] derived the following linear relationship between the moments of the charge density and those of the potential on the particle surfaces

$$\begin{bmatrix} \boldsymbol{\Phi} - \boldsymbol{\Phi}^{\infty} \\ \boldsymbol{E}^{\infty} \\ \vdots \end{bmatrix} = \begin{bmatrix} \boldsymbol{P}_{\Phi q} & \boldsymbol{P}_{\Phi q} & \dots \\ \boldsymbol{P}_{Eq} & \boldsymbol{P}_{Ep} & \\ \vdots & & \ddots \end{bmatrix} \cdot \begin{bmatrix} \boldsymbol{q} \\ \boldsymbol{p} \\ \vdots \end{bmatrix}. \tag{2.16}$$

Here, $\boldsymbol{\Phi} - \boldsymbol{\Phi}^{\infty}$ is an N-dimensional vector containing the potentials at the particle centers less the external potential present in their absence. Similarly, $\boldsymbol{E}^{\infty}$ is a $3N$-dimensional vector containing the external electric field evaluated at the particle centers. For the present case of parallel electrodes, the external field is uniform and directed normal to the electrode surface. These quantities are related to the vectors of particle charges $\boldsymbol{q}$ and dipole moments $\boldsymbol{p}$ by the so-called grand potential tensor $\mathcal{P}$, which is symmetric and positive definite.[18]

From the quantities in equation (3.4), one can readily determine the effective permittivity of the particle dispersion and/or the electrostatic free energy of the system. In other words, this relation is all we need to compute the macroscopic material properties or the field-induced forces that drive particle dynamics. The primary purpose of the present work is to accurately and efficiently evaluate equation (3.4) for an arbitrary distribution of spherical particles between two grounded planes. Our approach follows closely that of Swan & Brady [194] who solved an analogous hydrodynamic problem posed by a collection of solid spheres moving between parallel walls. We build on previous work[56] on the electrostatics of a single conductive particle between parallel electrodes, which provides analytical expressions for the 'self'

components of the potential tensor. Here, these self contributions are augmented by those due to neighboring particles, which modify the local potential and field.

In the simulation method, we do not solve for the grand potential tensor directly but instead rely on iterative methods (e.g., GMRES) to solve for the unknown quantities (e.g., the particle potentials $\boldsymbol{\Phi}$ and dipoles $\boldsymbol{p}$). Such methods rely on the rapid and repeated evaluation of the right-hand-side of equation (3.4). To this end, it is convenient to focus on a particular particle n and clearly distinguish the self contributions from those due to the other particles. We therefore write the inegral solution of equation (3.3) as

$$\phi(\boldsymbol{x}) - \phi^{\infty}(\boldsymbol{x}) = \int_{V_n} \mathcal{G}(\boldsymbol{x}, \boldsymbol{x}')\rho_n(\boldsymbol{x}')d\boldsymbol{x}' + \phi'_n(\boldsymbol{x}), \tag{2.17}$$

where $\phi'_n(\mathbf{x})$ represents the disturbance potential due to the other particles. Integrating the potential over the surface of particle n, one can show that

$$\Phi_n - \Phi_n^{\infty} = \left(P_{\Phi q}^{(S)} q_n + \boldsymbol{P}_{\Phi p}^{(S)} \cdot \boldsymbol{p}_n + \dots\right) + \phi'_n(\boldsymbol{x}_n), \tag{2.18}$$

where $\boldsymbol{\Phi}_n = \phi(\boldsymbol{x}_n)$ and $\boldsymbol{\Phi}_n^{\infty} = \phi^{\infty}(\boldsymbol{x}_n)$ are evaluated at the particle's center $\boldsymbol{x}_n$, and $\boldsymbol{P}^{(S)}$ is the self potential tensor for a single particle between two parallel electrodes. The relevant components of the self potential tensor for the case of uniformly charged, dielectric spheres are detailed in Appendix A. Similarly, by integrating the product of $\phi(\boldsymbol{x})$ and $\boldsymbol{x} - \boldsymbol{x}_n$ over the particle surface, one can show that

$$\boldsymbol{E}_n^{\infty} = \left(\boldsymbol{P}_{Eq}^{(S)} q_n + \boldsymbol{P}_{Ep}^{(S)} \cdot \boldsymbol{p}_n + \dots\right) + \nabla\phi'_n(\boldsymbol{x}_n), \tag{2.19}$$

where $\boldsymbol{E}_n^{\infty}$ is the electric field at the center of particle n. Higher order moments of the potential can be constructed in a analogous manner; however, we limit our present analysis at the level of particle dipoles.

To make use of equations (3.6) and (3.7), we require a strategy to compute the the disturbance potential and its gradient at the particle centers given the particle charges and dipole moments. In Section 3.2.2, we derive a general solution for the electric potential due to an arbitrary charge distribution positioned between two grounded planes using a novel approach of pseudo-periodic charge distribution. In Section 2.3.3, we describe how this solution can be implemented efficiently using a the Ewald method for periodic distribution of charge. Importantly, the resulting solution of the Ewald method is only accurate in the far field owing to the truncation of the multipole expansion in equation (3.4). In Section 3.2.3, we describe how the stokesian dynamics approach can be applied to accurately incorporate near field contributions for the important limiting case of conducting particles. We further discuss the technical details of implementing the simulation approach in practice.

2.3.2 Pseudo-periodic distribution of charge and electric potential between two grounded planes

We consider the potential due to a periodic charge distribution $\rho(\boldsymbol{x})$ with periods L_1 and L_2 in the $\boldsymbol{e}_1$ and $\boldsymbol{e}_2$ directions (Fig. 3.2). The charge is sandwiched between two grounded planes positioned at $x_3 = 0$ and $x_3 = L_3$. The resulting potential $\phi(\boldsymbol{x})$ is similarly periodic with the additional condition that $\phi = 0$ on the upper and lower boundaries. This problem can be approached in two different ways. The first approach uses the method of image charges[107] to construct an equivalent three-dimensionally periodic charge distribution on a larger domain (Fig. 3.2); the potential is then solved using standard methods for Ewald summation.[41] The second approach uses the Green's function for a point charge between grounded planes to derive an analogous

Ewald method for the two-dimensionally periodic system. The focus of this paper would be on utilizing first approach considering cost of computing green functions for wall contributions greatly slow down the computation in second approach.

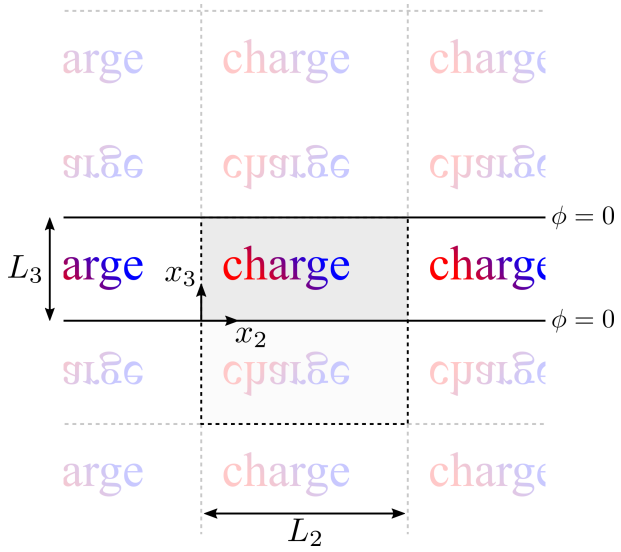

Figure 2.2: Schematic illustration of a two-dimensionally periodic charge distribution between two grounded planes. The zero potential conditions at $x_3 = 0$ and $x_3 = L_3$ are satisfied by an infinite system of image charges obtained by reflecting the charge and its images about both planes. Reflection about two planes separated by a distance L_3 is identical to translation over a distance of $2L_3$; consequently, this problem is identical to that of a three-dimensionally periodic charge distribution with periods $L_1 \times L_2 \times 2L_3$ (dotted lines).

We first expand the charge density and the potential in Fourier series along all the three directions

$$\rho(\boldsymbol{x}) = \sum_{k_1,k_2,k_3} e^{-2\pi i k_\alpha x_\alpha} \rho^{(k)}, \tag{2.20}$$

$$\phi(\boldsymbol{x}) = \sum_{k_1,k_2,k_3} e^{-2\pi i k_\alpha x_\alpha} \phi^{(k)}, \tag{2.21}$$

where $k_j = n/L_j$ for $n = 0, \pm 1, \pm 2, \ldots$ are the wavevectors, and repeated Greek indices signify summation over the index values $(1, 2, 3)$. The Fourier coefficients are related to one another through equations (3.1) and (3.2) as

$$(2\pi k)^2 \phi^{(k)} = -\frac{\rho^{(k)}}{\varepsilon}, \tag{2.22}$$

where $k^2 = k_\alpha k_\alpha$. This equation can be solved to obtain the following solution

$$\phi^{(k)} = \mathcal{G}^{(k)} \rho^{(k)}, \tag{2.23}$$

in which the Fourier coefficients of the Green's function $\mathcal{G}^k$ are given by

$$\mathcal{G}^{(k)} = -\frac{1}{(2\pi k)^2 \varepsilon}. \tag{2.24}$$

This term describes the contribution due to a point charge in an unbounded medium.

2.3.3 Ewald summation technique

The potential generated by a three-dimensionally periodic charge distribution in a dielectric medium is

$$\varepsilon \phi(\mathbf{x}) = \sum_{\boldsymbol{\xi} \neq 0} e^{-2\pi i \boldsymbol{\xi} \cdot \mathbf{x}} (2\pi \xi)^{-2} \rho^{(\xi)}, \tag{2.25}$$

where the $\boldsymbol{\xi}$ are the three-dimensional reciprocal lattice vectors, and the $\rho^{(\xi)}$ term represents the three-dimensional Fourier coefficients of the charge distribution. To accelerate this otherwise slowly converging summation, the Ewald technique carries out one part of the summation in real space and the other in reciprocal space

$$\varepsilon \phi(\mathbf{x}) = \frac{1}{4\pi} \int_V \frac{1}{r} \operatorname{erfc}\left(\sqrt{\pi r^2/\alpha}\right) \rho(\mathbf{x}') d\mathbf{x}' + \sum_{\boldsymbol{\xi} \neq 0} e^{-2\pi i \boldsymbol{\xi} \cdot \mathbf{x}} (2\pi \xi)^{-2} e^{-\pi \alpha \xi^2} \rho^{(\xi)}, \tag{2.26}$$

where $\mathbf{r} = \mathbf{x} - \mathbf{x}'$, and α is the so-called splitting parameter[194]. Notice that the summation in (2.26) is the exact solution for the potential due to a charge distribution with Fourier coefficients $e^{-\pi\alpha\xi^2}\rho^{(\xi)}$. This charge distribution – denoted ρ_g for 'global' charge distribution – contains the long-range contributions to the potential, while the remaining charge $\rho - \rho_g$ gives rise to short-ranged effects.

2.3.4 Reflections in real space

In an unbounded medium, the local potential ϕ_l governed by equation (**??**) can be written as

$$\phi_l(\mathbf{x}) = \int_V \frac{1}{4\pi\varepsilon r}(\rho(\mathbf{x}') - \rho_g(\mathbf{x}'))d\mathbf{x}', \tag{2.27}$$

where $\mathbf{r} = \mathbf{x} - \mathbf{x}'$. Substituting equation (**??**) for the global charge density, we can rewrite equation (2.27) to obtain

$$\phi_l(\mathbf{x}) = \int_V \frac{1}{4\pi\varepsilon r}\left[\int_V \left(\delta(\mathbf{r}') - \frac{e^{-\pi r'^2/\alpha}}{\alpha^{3/2}}\right)\rho(\mathbf{x}'')d\mathbf{x}''\right]d\mathbf{x}', \tag{2.28}$$

where $\mathbf{r}' = \mathbf{x}' - \mathbf{x}''$. Changing the order of integration and evaluating the integral over $\mathbf{x}'$, we find

$$\phi_l(\mathbf{x}) = \int_V G_l(\mathbf{r}''; \alpha)\rho(\mathbf{x}'')d\mathbf{x}'', \tag{2.29}$$

where $\mathbf{r}'' = \mathbf{x} - \mathbf{x}''$ and $G_l(\mathbf{r}; \alpha)$ is a Green's-like function for a point charge neutralized by a Gaussian envelope

$$G_l(\mathbf{r}; \alpha) = \frac{1}{4\pi\varepsilon r}\,\mathrm{erfc}\left(\sqrt{\pi r^2/\alpha}\right). \tag{2.30}$$

This result is simply the real-space contribution to the Ewald summation of equation (2.26). Importantly, the potential disturbance due to a charge at $\mathbf{x}''$ decays faster than exponentially over a distance $\sqrt{\alpha/\pi}$.

To account for boundary condition $\phi_l = 0$ on the electrode surface usually we introduce a fictitious 'image' charge distribution $\rho_i(\mathbf{x}) = -\rho(\mathbf{x} + 2x_3\mathbf{e}_3)$ which is added to the actual charge to satisfy the boundary condition but instead we consider pseudo-periodic simulation box as described in 3.2.2 which emulates the method of images.

2.3.5 Computations in wave space

In the particle-mesh approach, the charge distribution $\rho(\mathbf{x})$ due to the particles is approximated by a collection of point charges

$$\rho(\mathbf{x}) = \sum_n \delta(\mathbf{x} - \mathbf{x}_n) q_n, \tag{2.31}$$

where q_n is the magnitude of the n^{th} point charge. Applying the Gaussian filter of equation (**??**) yields the global charge density

$$\rho_g(\mathbf{x}) = \sum_n \frac{e^{\pi r_n^2/\alpha}}{\alpha^{3/2}} q_n, \tag{2.32}$$

where $\mathbf{r}_n = \mathbf{x} - \mathbf{x}_n$ and $r_n^2 = \mathbf{r}_n \cdot \mathbf{r}_n$. where $q_n^{(k)} = e^{2\pi i k_\alpha x_\alpha^{(n)}} q_n$. Substituting $\rho_g^{(k)}$ into equation 3.12 yields a rapidly converging summation describing the long-range contribution to the potential denoted $\phi_g(\mathbf{x})$.

$\phi_g^{(k)} = \sum_n G_g^{(k)}(\mathbf{r}, \alpha) q_n^{(k)}$, where the Green's-like function for $\mathrm{G}_g^{(k)}(\mathbf{r}, \alpha) = \frac{1}{4\pi k\varepsilon} \frac{\operatorname{erfc} \sqrt{\pi r^2/\alpha}}{r}$,

2.4 Results and discussion

Accurately accounting for electrostatic interparticle forces for a multiparticle system by considering many body potential problem and the integration of Maxwell stresses

over each particle becomes very tidious so we utilize an alternative strategy suggested by Bonnecaze[21] that uses electrostatic energy of the system to calculate the electrostatic interparticle forces.

2.4.1 Dynamics of chain formation or 'Bucket Brigade' during multiparticle CCEP

The term "Bucket Brigade" here refers to the transporting items over large distances by transferring it between multiple members of brigade that are either stationary or moving. Analogues behavior is observed during the CCEP of multiple particle systems where conductive particles form chain like assembly to transfer charge from one electrode to another. One experimental realization of such phenomenon has been reported with multiple aluminum discs distributed randomly on the surface of a dielectric liquid between two electrodes. Upon application of the field, the discs organized to form linear chains which oscillate continuously, passing charge from neighbor to neighbor. Similar behaviors have been observed for water drops moving in oil between two electrodes. If the number of particles in the system are equal to or more than L/2a the chain connects the oppositely charged electrodes and lead to short circuit. Here we use our simulation to predict and validate the existence of these chain formations that have been observed and reported in experiments. Figure 2.3 illustrates the formation of chain like structures when multiple spherical conductive particles are dispersed in dielectric media between set of plate electrodes, as shown in snapshots the system of particles starts with multiple chains which coalesce over time to form a single chain. Particles appear to collide elastically despite the absence of inertia at low Reynolds numbers as was also shown in experimental results from

Chapter 1. During a collision between two spheres, the total charge is conserved and redistributes between the spheres to achieve a common electric potential. All these observations from the experiments are well captured by our simulation that incorporate both the electrostatic and hydrodynamic contributions.

2.4.2 Dynamics of cluster of particles between two electrodes

Utilizing particle shape to direct the motion of active colloids is generally applicable to any energy input or propulsion mechanism either it be chemical, electrical or magnetic. CCEP can be used to continuously power the up and down motion of the cluster if cluster consist of at least one particle with different dielectric value (conductive particle for our case). The shape of the cluster determines what trajectory the cluster is going to assume. Though the introduction of electrostatics of CCEP the cluster trajectory becomes more complex since the electrostatic force and torques experienced by the particle are off center while the hydrodynamic drag experienced by the cluster is at the center. An interesting example of such a system is a six particle cluster with an octahedron geometry and three conductive particle as shown in Figure 2.4.

2.5 Conclusion

An accurate and efficient approach has been developed to successfully simulate dynamics of system of multiple particles dispersed between two parallel grounded electrodes. Taking into account confinement with both the electrostatic and hydrodynamic effects, this is tackled by deploying accurate and computationally efficient

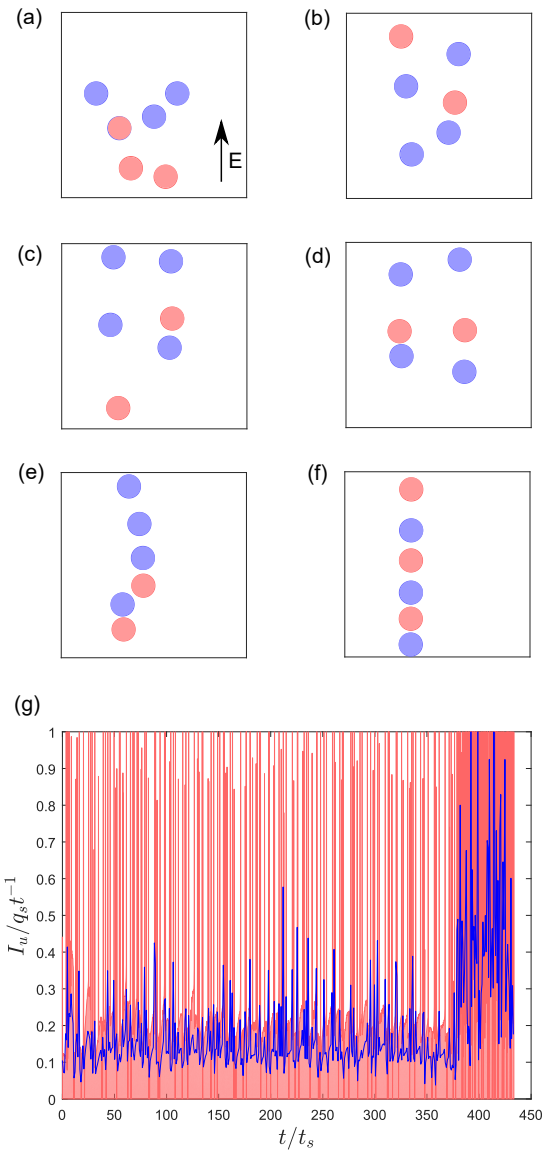

Figure 2.3: (a) Instantaneous snapshots of multiple particles interacting with each other while performing Contact charge electrophoresis leading to formation of chain like structure. (b) Computed electric current registered on upper electrode due to the movement of a charged spherical particles via CCEP. The current takes into account the collision of particles with the upper wall and collision between the particles. The results are presented in dimensionless form using the characteristic scales $q_s = 4\pi\epsilon\epsilon_0 a^2 E_0$ and $t_s = 3/2\epsilon\epsilon_0 E_0^2$. Note that as the chain forms at $t = 380t_s$ and the amount of charge transferred to the upper electrode spikes as shown by blue solid line, suggesting increased transfer of charge on chain formation.

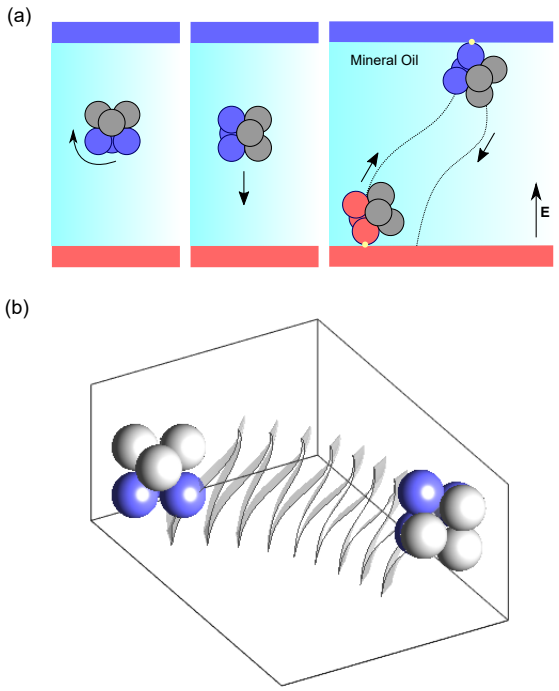

Figure 2.4: (a) Schematic illustration of two-dimensional dynamics of alignment and trajectory for a Janus Octahedron particle cluster with three conductive and three non-conductive particles in the cluster, non-conductive particles are represented by grey while positively charged and negatively charged particles are shown in red and blue respectively. (b) The trajectory of Janus Octahedron is shown using a three dimensional ribbon plot of the movement of cluster centroid.

methodology similar to the Stokesian dynamics approach. Typical to a Stokesian dynamics like approach, the electrostatic interactions of multiple particle suspension is broken down into far-field and near-field components. The effect of confinement is introduced by considering a pseudo-periodic lattice with twice the size of original configuration to emulate the method of images. Previously reported observations of chain formation in experiments have been modeled using the described simulation approach and all the dynamic behaviors illustrated. Apart from dispersion of conductive particles results for partially conductive clusters have also been illustrated for the case of Janus octahedron cluster which also points towards the importance of presence of walls on trajectory of cluster.

Chapter 3

Confinement induced effective conductivity variations in random suspensions of spherical particles

3.1 Introduction

[1]Computational prediction of effective conductivity over wide range of volume fractions covered by Bonnecaze(1991) has been applied to simulate the dynamics of electro- and magnetorheological fluids[21, 17] comprised of dispersions of colloidal particles interacting *via* dipolar forces. Previous simulation studies of these systems have focused almost exclusively on the bulk properties of the dispersions. Finite size effects due to the presence of confining boundaries are typically neglected. There are,

[1]The material presented in this chapter is being prepared for submission to Journal of Chemical Physics with permission from Shashank Pandey, Mikolaj Kowalik and Kyle J. M. Bishop. Author responsibilities were as follows: S.P. and K.J.M.B. developed the algorithms and performed simulations. All authors contributed to final text. Supplementary Information is available in appendix B.

however, scenarios in which these boundary effects are important. For example, in the context of heat transfer fluids, the effective conductivity depends on the thickness of the layer through which heat is conducted since presence of film can lead to formation of microstructures that can drastically change electro-thermomechanical properties of material over very small changes in film thickness as shown by Wei and Takele [196, 211] which correlate between the electrical conductivity of Ag/polymer matrix nanocomposites in thin-film form and their microstructures as a function of both film thickness and metal loading. There are other phenomena in which the bounding electrodes play a critical role -e.g., in contact charge electrophoresis (CCEP) [60, 33].

Micro- and nanoscale particles are often incorporated within otherwise homogenous media to modify their macroscopic material properties. For example, nanoparticles are commonly added to heat transfer fluids to increase their effective thermal conductivity [43, 199] or to polymeric materials to modify their dielectric properties.[127] A wide variety of physical problems involving such two-phase media can be described using the following continuum equations within both the dispersed and the continuous phases [18]

$$\nabla \cdot \boldsymbol{D} = \rho(\boldsymbol{x}), \tag{3.1}$$

$$\boldsymbol{D} = -\varepsilon \nabla \phi. \tag{3.2}$$

The first equation is a conservation equation that relates the flux $\boldsymbol{D}$ to spatially distributed sources and sinks described by $\rho(\boldsymbol{x})$. The second is a linear constitutive equation that connects the flux $\boldsymbol{D}$ to the corresponding potential gradient $\nabla\phi$ by means of a coefficient ε. In the context of electrostatics,[128] $\boldsymbol{D}$ is the electric displacement, ρ is the charge density, ϕ is the electric potential, and ε is the per-

mittivity. For reasons of mathematical analogy, this formalism can also describe the steady transport of heat, mass, and charge through two-phase media as well as the linear magnetic response of such materials (Table 3.1).

The macroscopic properties of particle dispersions (e.g., the effective permittivity) depend on the properties of each phase and on their microscopic arrangement. This relationship was originally addressed by Maxwell,[141] who recognized that the change in permittivity due to the addition of particles was related to their average dipole moment in the applied field.[9, 18] For macroscopically homogeneous and isotropic dispersions, there exists rigorous upper and lower bounds on the effective permittivity ε_{eff} in terms of the volume fractions and permittivities of each phase.[95] These bounds agree to within ca. 2% across all particle volume fractions ϕ when the permittivity of the particles is similar to that of the continuous phase (i.e., when $\varepsilon_p \approx \varepsilon$). When, however, the properties of the dispersed phase differ significantly from those of the continuous phase (e.g., when $\varepsilon_p \gg \varepsilon$), the upper and lower bounds offer divergent predictions, which can be resolved only by careful consideration of the particle microstructure. The sensitive dependence of macroscopic properties on microscopic structure is well illustrated by the case of heat transport in nanofluids, where fractal particle aggregates give rise to large enhancements in the effective conductivity at low volume fractions. [116]

Beyond predicting macroscopic material properties, accurate microscopic models of particle dispersions are essential in describing their dynamic response to applied electric and magnetic fields. The electric or magnetic dipoles induced by the field give rise to dipolar interactions among the particles, which can mediate their assembly into chains and fibers. Such field-induced changes in the particle microstructure

Table 3.1: Conductive-type transport phenomena governed by equations (3.1) and (3.2).[18]

material flux, $\boldsymbol{D}$	**gradient, $\nabla\phi$**	**transport coefficient, ε**
heat flux	temperature gradient	thermal conductivity
mass flux	concentration gradient	diffusion coefficient
current density	electric field	electrical conductivity
electric displacement	electric field	permittivity
magnetic induction	magnetic field	permeability

can increase the effective viscosity of the fluid by up to 10^5 times and provides the basis for electro- and magneto-rheological fluids.[90, 161, 29] In addition to electric polarization, conductive particles dispersed in dielectric (perfectly insulating) fluids can acquire electric charge on contact with the bounding electrodes and/or each other. The resulting back-and-forth motions of such contact-charged particles in the applied field is termed contact charge electrophoresis (CCEP).[59, 54] While the oscillatory motion of individual particles is well understood,[54] the collective dynamics of many interacting particles moving by CCEP is less explored. Such particles are known to organize spontaneously to form oscillating particle chains – so called bucket brigades – that transport charge from one electrode to the other.[166, 52] Accurate numerical simulations of such processes must account for (1) far-field many body interactions among the particles, (2) near-field interactions governing contact charge transfer, and (3) the effects of confinement by the bounding electrodes. Moreover, the simulation methodology must be efficient as to allow for rapid and repeated computation of the electrostatic forces driving the particle dynamics.

In this context, the 'stokesian dynamics' method is particularly well-suited to de-

scribe the electrostatics of many conductive spheres dispersed in a dielectric medium.[18] Rather than solve for the electric potential directly, this approach seeks to approximate the capacitance matrix, which relates the charge and dipole moment on each particle to the external field and the corresponding particle potential. To achieve an accurate and efficient approximation, the calculation of the capacitance matrix is divided into far field and near field contributions. In the far field, the charge distribution of each particle is approximated by a truncated multipole expansion; the self-consistent calculation of the multipole moments captures the many body electrostatic interactions among the conductive spheres. In the near field, the contributions due to higher order moments are introduced in a pairwise fashion using analytical results for the interaction between two conductive spheres.[44] This approach has been applied to compute the effective conductivity of random particle dispersions[20] and to simulate particle dynamics in electrorheological fluids.[21, 17] In these previous reports, periodic boundary conditions are used to approximate unbounded, bulk dispersions; however, it is sometimes necessary to consider the effects of system boundaries. Examples include the dielectric response of thin film polymer nanocomposites, heat transfer through lubricating films of nanofluids, as well as CCEP between parallel plane electrodes. In each case, the effective properties of the film or the dynamics of the dispersion can depend on the extent of confinement between the parallel boundaries.

Here, we extend the 'stokesian dynamics' approach to describe the electrostatics of particles dispersions sandwiched between two plane boundaries at constant potential.

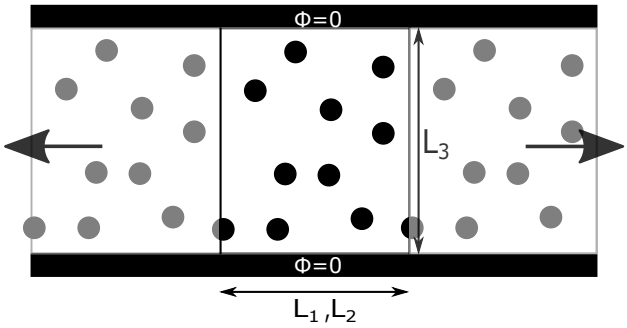

Figure 3.1: Schematic of the simulation domain.

3.2 Methods

3.2.1 The grand potential tensor

We consider an collection of N charged, dielectric particles positioned within an uncharged, dielectric medium between two parallel electrodes of infinite extent. The particles are spherical in shape, and their respective charges are distributed uniformly throughout their interiors. The case of conductive spheres will be treated as a limiting case, in which the permittivity of the particles greatly exceeds that of the surrounding medium, $\lambda = \varepsilon_p/\varepsilon \to \infty$. The electric potential $\phi(\boldsymbol{x})$ in and around the particles can be expressed as

$$\phi(\boldsymbol{x}) - \phi^{\infty}(\boldsymbol{x}) = \sum_{n=1}^{N} \int_{V_n} \mathcal{G}(\boldsymbol{x}, \boldsymbol{x}')\rho_n(\boldsymbol{x}')d\boldsymbol{x}', \tag{3.3}$$

where $\phi^{\infty}(\boldsymbol{x})$ is the external potential, ρ_n and V_n are, respectively, the charge density and the volume of particle n, and $\mathcal{G}(\boldsymbol{x}, \boldsymbol{x}')$ is the relevant Green's function for the potential at position $\boldsymbol{x}$ due to a unit charge at position $\boldsymbol{x}'$ between two grounded planes.[170] By expanding the Green's function in a Taylor series about the center of each particle and integrating over the particle surfaces, Bonnecaze & Brady[18]

derived the following linear relationship between the moments of the charge density and those of the potential on the particle surfaces

$$\begin{bmatrix} \boldsymbol{\Phi} - \boldsymbol{\Phi}^{\infty} \\ \boldsymbol{E}^{\infty} \\ \vdots \end{bmatrix} = \begin{bmatrix} \boldsymbol{P}_{\Phi q} & \boldsymbol{P}_{\Phi q} & \dots \\ \boldsymbol{P}_{Eq} & \boldsymbol{P}_{Ep} & \\ \vdots & & \ddots \end{bmatrix} \cdot \begin{bmatrix} \boldsymbol{q} \\ \boldsymbol{p} \\ \vdots \end{bmatrix} . \tag{3.4}$$

Here, $\boldsymbol{\Phi} - \boldsymbol{\Phi}^{\infty}$ is an N-dimensional vector containing the potentials at the particle centers less the external potential present in their absence. Similarly, $\boldsymbol{E}^{\infty}$ is a $3N$-dimensional vector containing the external electric field evaluated at the particle centers. For the present case of parallel electrodes, the external field is uniform and directed normal to the electrode surface. These quantities are related to the vectors of particle charges $\boldsymbol{q}$ and dipole moments $\boldsymbol{p}$ by the so-called grand potential tensor $\mathcal{P}$, which is symmetric and positive definite.[18]

From the quantities in equation (3.4), one can readily determine the effective permittivity of the particle dispersion and/or the electrostatic free energy of the system. In other words, this relation is all we need to compute the macroscopic material properties or the field-induced forces that drive particle dynamics. The primary purpose of the present work is to accurately and efficiently evaluate equation (3.4) for an arbitrary distribution of spherical particles between two grounded planes. Our approach follows closely that of Swan & Brady [194] who solved an analogous hydrodynamic problem posed by a collection of solid spheres moving between parallel walls. We build on previous work[56] on the electrostatics of a single conductive particle between parallel electrodes, which provides analytical expressions for the 'self' components of the potential tensor. Here, these self contributions are augmented by those due to neighboring particles, which modify the local potential and field.

In the simulation method, we do not solve for the grand potential tensor directly but instead rely on iterative methods (e.g., GMRES) to solve for the unknown quantities (e.g., the particle potentials $\boldsymbol{\Phi}$ and dipoles $\boldsymbol{p}$). Such methods rely on the rapid and repeated evaluation of the right-hand-side of equation (3.4). To this end, it is convenient to focus on a particular particle n and clearly distinguish the self contributions from those due to the other particles. We therefore write the inegral solution of equation (3.3) as

$$\phi(\boldsymbol{x}) - \phi^{\infty}(\boldsymbol{x}) = \int_{V_n} \mathcal{G}(\boldsymbol{x}, \boldsymbol{x}')\rho_n(\boldsymbol{x}')d\boldsymbol{x}' + \phi'_n(\boldsymbol{x}), \tag{3.5}$$

where $\phi'_n(\mathbf{x})$ represents the disturbance potential due to the other particles. Integrating the potential over the surface of particle n, one can show that

$$\Phi_n - \Phi_n^{\infty} = \left(P_{\Phi q}^{(S)} q_n + \boldsymbol{P}_{\Phi p}^{(S)} \cdot \boldsymbol{p}_n + \dots\right) + \phi'_n(\boldsymbol{x}_n), \tag{3.6}$$

where $\boldsymbol{\Phi}_n = \phi(\boldsymbol{x}_n)$ and $\boldsymbol{\Phi}_n^{\infty} = \phi^{\infty}(\boldsymbol{x}_n)$ are evaluated at the particle's center $\boldsymbol{x}_n$, and $\boldsymbol{P}^{(S)}$ is the self potential tensor for a single particle between two parallel electrodes. The relevant components of the self potential tensor for the case of uniformly charged, dielectric spheres are detailed in Appendix A. Similarly, by integrating the product of $\phi(\boldsymbol{x})$ and $\boldsymbol{x} - \boldsymbol{x}_n$ over the particle surface, one can show that

$$\boldsymbol{E}_n^{\infty} = \left(\boldsymbol{P}_{Eq}^{(S)} q_n + \boldsymbol{P}_{Ep}^{(S)} \cdot \boldsymbol{p}_n + \dots\right) + \nabla\phi'_n(\boldsymbol{x}_n), \tag{3.7}$$

where $\boldsymbol{E}_n^{\infty}$ is the electric field at the center of particle n. Higher order moments of the potential can be constructed in a analogous manner; however, we limit our present analysis at the level of particle dipoles.

To make use of equations (3.6) and (3.7), we require a strategy to compute the the disturbance potential and its gradient at the particle centers given the particle charges

and dipole moments. In Section 3.2.2, we derive a general solution for the electric potential due to an arbitrary charge distribution positioned between two grounded planes. In Section 2.3.3, we describe how this solution can be implemented efficiently using a variant of the Ewald method that respects the boundary conditions on the electrode surfaces. Importantly, the resulting solution of the Ewald method is only accurate in the far field owing to the truncation of the multipole expansion in equation (3.4). In Section 3.2.3, we describe how the stokesian dynamics approach can be applied to accurately incorporate near field contributions for the important limiting case of conducting particles. We further discuss the technical details of implementing the simulation approach in practice.

3.2.2 Pseudo-periodic electric potential and charge distribution between two grounded planes

We consider the potential due to a periodic charge distribution $\rho(\boldsymbol{x})$ with periods L_1 and L_2 in the $\boldsymbol{e}_1$ and $\boldsymbol{e}_2$ directions (Fig. 3.2). The charge is sandwiched between two grounded planes positioned at $x_3 = 0$ and $x_3 = L_3$. The resulting potential $\phi(\boldsymbol{x})$ is similarly periodic with the additional condition that $\phi = 0$ on the upper and lower boundaries. This problem can be approached in two different ways. The first approach uses the method of image charges[107] to construct an equivalent three-dimensionally periodic charge distribution on a larger domain (Fig. 3.2); the potential is then solved using standard methods for Ewald summation.[41] The second approach uses the Green's function for a point charge between grounded planes to derive an analogous Ewald method for the two-dimensionally periodic system. The focus of this paper would be on utilizing first approach considering cost of computing green functions for

wall contributions greatly slow down the computation in second approach.

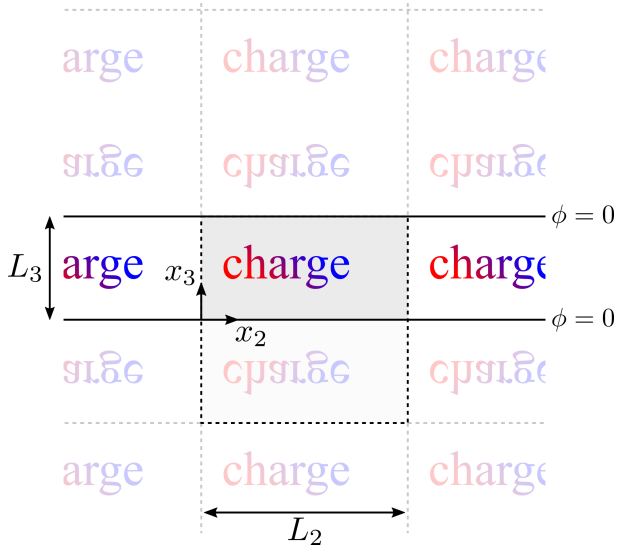

Figure 3.2: Schematic illustration of a two-dimensionally periodic charge distribution between two grounded planes. The zero potential conditions at $x_3 = 0$ and $x_3 = L_3$ are satisfied by an infinite system of image charges obtained by reflecting the charge and its images about both planes. Reflection about two planes separated by a distance L_3 is identical to translation over a distance of $2L_3$; consequently, this problem is identical to that of a three-dimensionally periodic charge distribution with periods $L_1 \times L_2 \times 2L_3$ (dotted lines).

We first expand the charge density and the potential in Fourier series along all the three directions

$$\rho(\boldsymbol{x}) = \sum_{k_1,k_2,k_3} e^{-2\pi i k_\alpha x_\alpha} \rho^{(k)}, \tag{3.8}$$

$$\phi(\boldsymbol{x}) = \sum_{k_1,k_2,k_3} e^{-2\pi i k_\alpha x_\alpha} \phi^{(k)}, \tag{3.9}$$

where $k_j = n/L_j$ for $n = 0, \pm 1, \pm 2, \ldots$ are the wavevectors, and repeated Greek indices signify summation over the index values $(1, 2, 3)$. The Fourier coefficients are

related to one another through equations (3.1) and (3.2) as

$$(2\pi k)^2 \phi^{(k)} = -\frac{\rho^{(k)}}{\varepsilon}, \tag{3.10}$$

where $k^2 = k_\alpha k_\alpha$. This equation can be solved to obtain the following solution

$$\phi^{(k)} = \mathcal{G}^{(k)} \rho^{(k)}, \tag{3.11}$$

in which the Fourier coefficients of the Green's function $\mathcal{G}^k$ are given by

$$\mathcal{G}^{(k)} = -\frac{1}{(2\pi k)^2 \varepsilon}. \tag{3.12}$$

This term describes the contribution due to a point charge in an unbounded medium.

3.2.3 Simulation procedure

We are now prepared to apply the above results using the stokesian dynamics approach to compute the electrostatic interactions among a collection of charged dielectric spheres between two parallel electrodes. For this electrode geometry, the applied field $\boldsymbol{E}^\infty$ is spatially uniform such that higher order derivatives of the external potential are identically zero. As a result, equation (3.4) can be inverted to obtain the following exact relation for the particle charges $\boldsymbol{q}$ and dipoles $\boldsymbol{p}$

$$\begin{bmatrix} \boldsymbol{q} \\ \boldsymbol{p} \end{bmatrix} = \mathcal{C} \cdot \begin{bmatrix} \boldsymbol{\Phi} - \boldsymbol{\Phi}^\infty \\ \boldsymbol{E}^\infty \end{bmatrix}, \tag{3.13}$$

where $\mathcal{C}$ is the grand capacitance matrix. [18] Knowledge of the capacitance matrix allows one to compute, for example, the particle potentials and dipole moments given their charges and the applied field. In principle, the capacitance tensor can be computed as the inverse of the potential tensor $\mathcal{C} = \mathcal{P}^{-1}$; however, in practice, such

computation requires large numbers of multipole moments to achieve an accurate approximation. The stokesian dynamics method overcomes this challenge by decomposing the capacitance tensor into near field and far field contributions, which can be computed in an efficient manner.

In particular, we decompose the particle charges and dipoles as

$$\begin{bmatrix} \boldsymbol{q} \\ \boldsymbol{p} \end{bmatrix} = \begin{bmatrix} \boldsymbol{q}^{ff} \\ \boldsymbol{p}^{ff} \end{bmatrix} + \mathcal{C}^{nf} \cdot \begin{bmatrix} \boldsymbol{\Phi} - \boldsymbol{\Phi}^{\infty} \\ \mathbf{E}^{\infty} \end{bmatrix}, \tag{3.14}$$

where the first term represents the far field contribution and the second the near field contribution. The former is obtained from equation (3.4) by truncating the potential tensor at the dipole level such that

$$\begin{bmatrix} \boldsymbol{\Phi} - \boldsymbol{\Phi}^{\infty} \\ \boldsymbol{E}^{\infty} \end{bmatrix} = \mathcal{P}^{\infty} \cdot \begin{bmatrix} \boldsymbol{q}^{ff} \\ \boldsymbol{p}^{ff} \end{bmatrix}, \tag{3.15}$$

where $\mathcal{P}^{\infty}$ denotes far field approximation to the potential tensor. This relationship captures the long-ranged, many-body interactions among the spheres but fails to describe near-field effects that arise between nearly contacting particles. The near field contributions to the capacitance tensor $\mathcal{C}^{nf}$ are computed in a pairwise fashion using analytical results for two spheres in an applied field.[45] The details of the far field and near field calculations are discussed in the following sections. For specificity, we will assume that the particle charge $\boldsymbol{q}$ and the applied field $\boldsymbol{E}^{\infty}$ are known; our objective is to compute the dipole moments $\boldsymbol{p}$ and the particle potentials $\boldsymbol{\Phi}$. Other variations of the problem can be solved in an analogous manner. As noted above, the linear system of equations (3.13) are solved in an iterative fashion using the GMRES method. We start with an initial guess for the far field charges $\boldsymbol{q}^{ff}$ and dipole moments $\boldsymbol{p}^{ff}$. The particle potentials and fields are then computed in accordance with equation

(3.15) using a particle-mesh Ewald implementation of the general solution derived in section 2.3.3. These provisional quantities are then used to evaluate the particle charges $\boldsymbol{q}$ and dipoles $\boldsymbol{p}$ accounting for the near-field contributions of equation (3.14). The far-field charges and dipoles are subsequently refined to minimize the residuals in the charge from equation (3.14) and in the field from equation (3.15).

The value of splitting parameter,$\sqrt{\frac{\alpha}{\pi}}$ governs the rate of decay. Since far-field electrostatic contribution is broken down by Ewald summation into two fast converging summations comprising far-field real space part and far-field wave space part, identifying the important length scales involved during both these summation procedures establishes the constraint on the system. For 'wave' space part where calculations are performed on discreet mesh points according to *Particle-Mesh-Ewald approach(PME)*[41], the constraint $\Delta x \ll \sqrt{\frac{\alpha}{\pi}}$ is established which implies that the width of Gaussian cloud, $\sqrt{\frac{\alpha}{\pi}}$ for a particle should be should be equal to several mesh spacing so as to accurately capture the interaction with particles on nearby mesh points. Similarly for the computations in the 'real' part of far-field, the radius of influence of disturbance should be smaller than half the domain length since minimum-image convention must be followed. Leading to constraint given by, $\frac{L}{2} \gg \sqrt{\frac{\alpha}{\pi}}$. The prominence of disturbance reduces to negligible amount on moving far away from the specific particle so it makes most sense to only consider disturbance effect on nearby particles in $\sqrt{\alpha}$ extent of the specific particle. From both these constraints we deduce the following bounds on the value of splitting alpha

$$\Delta x = \frac{L}{N_{grid}} \ll \sqrt{\frac{\alpha}{\pi}} \ll \frac{L}{2}.$$

Taking into consideration the bounds on value of splitting parameter,α, we come to

conclusion that there exist a relation between value of optimal beta and number of grid points.

For the case of random particle dispersion, the Stokesian dynamics like approach is used in conjugation with the High Performance Monte Carlo method for hard particles (HPMC) developed by Glotzer group[5, 83]. HPMC is a recent extension of HOOMD blue capable of performing parallel on several multicore CPUs and GPUs which drastically reduces the computational time required for generating random configurations of dispersion of particles. The HPMC code for random particle position generates equilibrated configuration averaged over 50 different realizations with each configuration tuned till it reaches optimal move size over 200,000 sweeps then the optimal move size is utilized for further 100,000 sweeps to obtain the final equilibrated configuration for a single realization. For every case of particle dispersion 50 realizations have been used to calculate the pair correlation function compared against the analytical solution of Percus-Yevick(an approximate closure of Ornstein-Zernike equation) as illustrated in Bonnecaze[20] and developed by[181, 168] for the case of hard-particle distribution in periodic media. Similarly for the case of confined media particle density analysis was performed similar to described in [50] where they provide tangible evidence for complete wetting based on rigorous simulations and observe that the portion of film near wall experiences crystalline ordering which increases with increasing "bulk" density of suspension, ρ_p. The choice of HPMC for our Monte Carlo procedure enables us to generate computationally efficient random particle positions which are easily reproducible.

3.3 Results and discussion

For a confined media we illustrate variation of conductivity for complete range of electrode separation with varying volume fraction. For this case of confined media, particle density variation as described in Dijkstra[50] should show complete wetting based on their rigorous simulations and we should observe that the portion of film near wall experiences crystalline ordering which increases with reduction in channel width leading to lower value of effective conductivity. Studying an analogues system, Swan[194] suggested for hydrodynamic interactions at low volume fractions the particle-wall interactions make the predominant contribution to the viscous dissipation while at high volume fractions the particle-particle hydrodynamic interactions dominate and the bulk rheology is recovered.

3.3.1 Drastic increase in conductivity at extreme confinement

At extreme confinements $\Xi - 2a < 2a$, we observe a drastic increase in the value of effective electrical conductivity of the dispersion due to the chaining of particles between the two electrodes.

3.3.2 Gradual increase in conductivity at moderate confinement

At moderate values of separation $2a < \Xi - 2a < 10a$, the effective electrical conductivity shows gradual increase with the increase in electrode separation, since due to the presence of walls particles near the walls arrange parallel to the walls that is perpen-

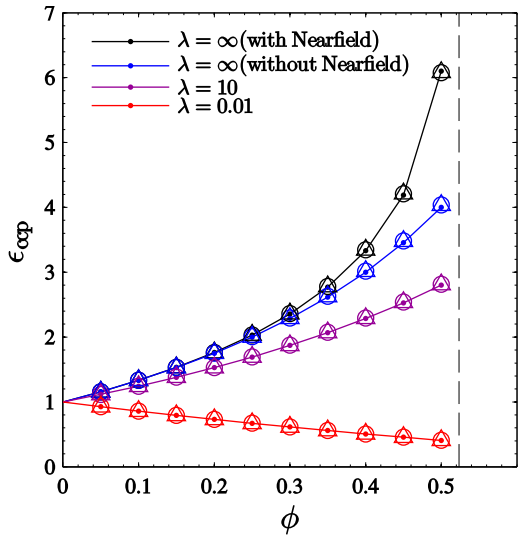

Figure 3.3: Effective conductivity of system for variation in particle volume fraction at different values of conductivity ratio represented by $\lambda(=\frac{\epsilon_p}{\epsilon_m})$ is plotted. The results for effective conductivity against particle volume fraction in unbounded periodic simple cubic lattice have been previously demonstrated by `Bonnecaze (1990)`[18], have been reproduced in our calculation for both periodic ($\triangle$) and confined ($\bigcirc$) lattice.

dicular to the electric field leading to reduced conductivity compared to the case of bulk unbounded dispersion, as was also explained by Dijkstra[50] who made a systematic study of the effect of plate separation and was able to distinguish a regime where complete wetting of the hard-sphere crystal appears to occur at the wall-dispersion interface. The oscillatory variation of effective conductivity with the increase in electrode separation can be explained by changing of the lattice from buckled state to rhombic state as has been previously reported in [178]. During the rhombic state the effective conductivity spikes while in buckled state the value of effective conductivity diminishes, giving a oscillatory variation to effective conductivity.

3.3.3 Conductivity asymtotes at large electrode separation

Confinement induces glassiness or high local density of particles near the walls but as the separation of walls increases bulk properties are restored. At electrode separation $\Xi - 2a > 10a$, the effective electrical conductivity of the dispersion asymtotes to the unbounded periodic random dispersion results for respective volume fraction of particles as shown in figure 3.4.

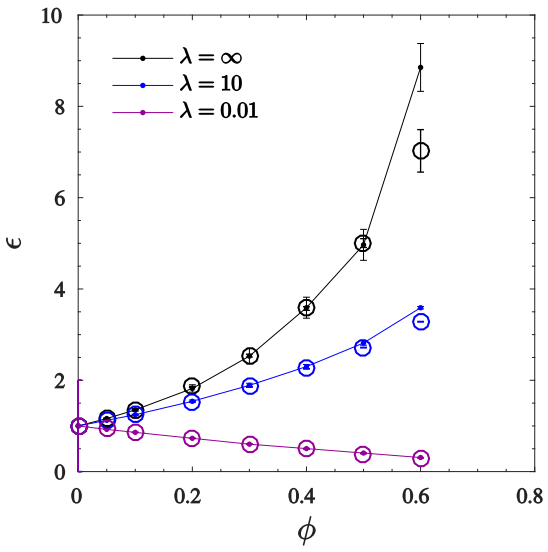

Figure 3.4: **Equilibrated suspension of randomly distributed particles in unbounded media**. Effective conductivity ($\circ$) for unbounded periodic random configuration against the particle volume fraction, ϕ is plotted and compared with the results demonstrated by `Bonnecaze(1991)`[20]; Note the difference in results for $\lambda = 10$ and ∞ at high volume fraction, $\phi = 0.6$.

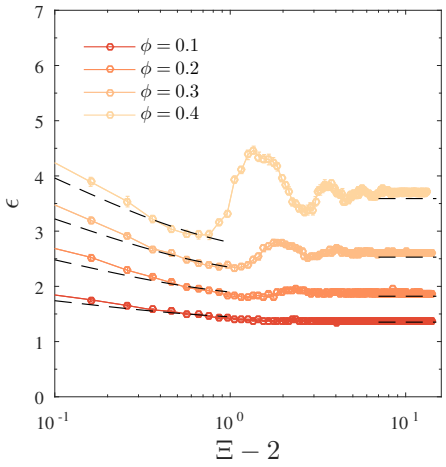

Figure 3.5: **Effect of confinement on the effective conductivity of randomly distributed particles**; Effective conductivity is plotted across channels of varying width covering entire range of values for different volume fractions, plot depict effective conductivity asymptotes to the unbounded periodic random configuration results from Figure 3 at large value of L_3.

3.4 Conclusion

To accurately account for all the electrostatic interactions involved in the system of multiple particles dispersed between two parallel grounded electrodes is a huge challenge, this electrostatic problem is tackled by deploying accurate and computationally efficient methodology similar to the Stokesian dynamics approach. The use of grand capacitance tensor representation allows for high level abstraction and breaks down this complicated problem to the relationship between different components of charge and potential moments on the particle, which allows us to utilize first and second

order Madelung constants to verify the relationships between charge-potential and dipole-field in order to validate the method. Typical to a Stokesian dynamics like approach, the electrostatic interactions of multiple particle suspension is broken down into far-field and near-field components which are furthermore differentiated on basis of presence of wall to include the particle-particle and particle-wall contributions separately. Utilizing this method, its possible to accurately quantify the dependence of effective conductivity of the dispersion of conductive particles on the channel width and particle volume fraction at low, moderate and high conductivity ratios. Currently we have been working to combine this approach with the Stokesian dynamics allowing us to understand more complex coupling of electric field and shear effects on suspension microstructure.

Chapter 4

Emergence of traveling waves in linear arrays of electromechanical actuators

4.1 Introduction

[1]Traveling waves of mechanical actuation provide a versatile strategy for locomotion and transport in both natural[39, 16, 198] and engineered[99, 158, 160, 140, 217] systems across many scales. In vertebrates such as the aquatic lamprey [39, 38], these and other rhythmic motor patterns are orchestrated by networks of neurons called central pattern generators (CPGs) [138], which are often idealized as systems

[1]The material presented in this chapter is reproduced from Ref. Shashank Pandey, Yong Dou, Charles Cartier, Olivia Miller and K. J. M. Bishop, Communications Physics volume 1, Article number 85, 2018. S.P., Y.D. and C.A.C. contributed equally to this work. Reproduced by permission of Nature Communication Physics and with permission from the authors. Author responsibilities were as follows: Y.D. and S.P. performed the experiments and analyzed the results. K.J.M.B. and S.P. developed the theoretical model. Y.D., S.P., C.A.C., O.M., and K.J.M.B. conceived the project and wrote the paper. Supplementary Information is available in appendix C.

of coupled oscillators [39, 38]. The rhythmic output of these oscillators is relayed to actuators (e.g., muscles) to produce complex motions without the need for sensory feedback. Similar control strategies based on CPGs are used to direct locomotion in macroscopic robots [99]. At smaller scales, however, it becomes increasingly challenging to accommodate centralized control systems capable of directing the coordinated actions of multiple actuators. Instead, microorganisms such as ciliated protozoa integrate pattern generation and mechanical actuation within a single material system. The oscillatory motions of beating cilia couple to one another through hydrodynamic interactions to produce metachronal waves that drive cellular locomotion through viscous surroundings [16, 151, 65]. This biological example illustrates how the coupled motions of many mechanical oscillators can organize spontaneously and autonomously to perform dynamic functions.

The realization of synthetic systems that mimic such functions requires experimental strategies for powering mechanical oscillators and for coupling their motions to achieve the desired dynamics. One approach relies on coupling reaction-diffusion patterns to the mechanical deformation of responsive gels, for example, to achieve traveling wave motions in excitable media[217, 140]. Despite fascinating demonstrations of this approach on millimeter length scales, it remains challenging to miniaturize due to the need for faster reactions that compete with diffusion at smaller scales. To achieve scalable mechanisms of pattern formation, the processes that drive oscillations should scale in the same way as those used to couple neighboring oscillators. In this context, electromechanical oscillators based on contact charge electrophoresis (CCEP) [13, 53] can provide a useful model on length scales spanning millimeters[142] to microns[52] (perhaps even nanometers [159, 125]).

CCEP refers to the back-and-forth motion of a conductive particle through an insulating fluid separating two electrodes subject to a constant voltage. The particle charges on contact with either electrode and moves down the applied potential gradient, thereby transporting charge between the biased electrodes. This type of electromechanical oscillator is fundamentally distinct from the weakly damped harmonic oscillators of micro-electromechanical systems (MEMS)[204, 218], which rely on resonant excitation by time-varying fields. By contrast, CCEP oscillators are powered by a constant thermodynamic driving force and operate even under conditions of strong damping, which arise at small scales and in viscous environments. Similar to those of molecular motors[123, 125], CCEP motions can be rectified to perform mechanical work or to transport material cargo[57, 125]. Moreover, the charge acquired by the particle and the forces driving its motion are well described by classical electrostatics, which is invariant to changes in scale. The discovery of new CCEP motions at the macroscale is therefore transferable to emerging applications at the microscale[13].

Here, we investigate the collective dynamics of many CCEP oscillators positioned along a linear array between two (nearly) parallel electrodes (Fig. D.1a). Each oscillator is comprised of a conductive sphere that moves back and forth between the electrodes along a dielectric track. Oscillatory motions are driven by the repeated charging of the particles on contact with either electrode and their subsequent movement in the applied field. The dynamics of neighboring oscillators are coupled to one another through the electrostatic interactions between the charged particles. We show how this electrostatic coupling mediates the organization of phase-locked states in which all oscillators move with a common frequency. Interestingly, the distribution

of oscillator phases at steady state corresponds to traveling waves of particle motion with a characteristic wavelength comparable to the electrode separation. These experimental observations are explained by a Kuromoto-like model[1, 201] that accounts for weak repulsive coupling between neighboring phase oscillators and for small systematic variations in their natural frequencies. We demonstrate how traveling wave synchronization can be used to transport material cargo along the length of the oscillator array. More generally, our approach shows how simple energy inputs can power complex patterns of mechanical actuation, which may be useful in powering the motions of soft robots[176, 2] and colloidal machines[183, 214, 139, 86, 62].

4.2 Experiment

Copper spheres ($a = 1$ mm in radius) immersed in mineral oil were positioned within an array of dielectric tracks connecting two plane electrodes separated by a distance L (Fig. D.1a). The tracks were spaced evenly with a period $W = 3a$ and aligned perpendicular to the electrode surfaces and to the direction of gravity. Each track contained a single particle, which was free to move back and forth between the two electrodes. Application of a constant voltage (typically, $V = 10$ kV) caused the particles to oscillate continuously between the electrodes via contact charge electrophoresis (CCEP) [13, 53]. The conductive particles acquired an electrostatic charge on contact with the biased electrodes and moved under the influence of the applied field. This periodic cycle of contact charging and electrostatic actuation continued for as long the voltage was applied.

Figure D.1b shows the reconstructed trajectory of a single sphere oscillating be-

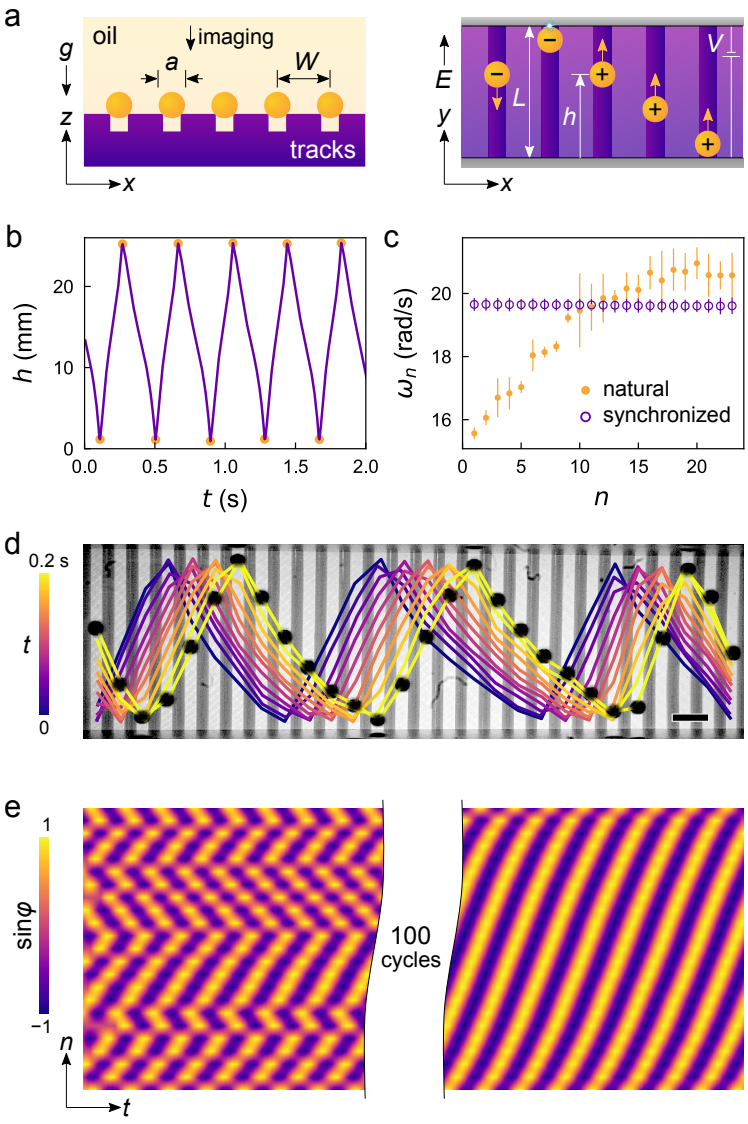

Figure 4.1: **Travelling wave synchronization.** (a) Conductive spheres immersed in mineral oil oscillate along dielectric tracks connecting two plane electrodes subject to a constant voltage V. Particles charge on contact with each electrode and move in the electric field E. (b) Oscillatory dynamics of a single particle; yellow markers denote contacts with the electrodes. The applied voltage is $V = 19$ kV; the electrode separation is $L = 25$ mm. (c) Oscillation frequency ω_n as a function of the position n along the array. The natural frequency of each oscillator varies with position (solid markers); all oscillators move with a common frequency in the synchronized state (open markers). (d) Image of the experiment showing particle positions at successive times; scale bar is 3 mm. See also Supplementary Movie 1. (e) Space-time plot showing the emergence of traveling wave synchronization for the $N = 23$ oscillators in (c) starting from a random initial configuration. Here, the track period is $W = 3$ mm; other parameters are listed in (b). See also Supplementary Movie 2 and Figure

tween the two electrodes. Each time the particle contacts an electrode, its charge changes sign and the particle reverses direction under the influence of the field. To facilitate the analysis of multiple particles over many oscillation cycles, we record the times at which each particle contacts one of the electrodes. From this data, we approximate the phase of each oscillator by interpolating between successive contacts as $\varphi(t) = 2\pi(t - t_k)/(t_{k+1} - t_k)$ where t_k denotes the time of the k^{th} contact and $t_k \leq t < t_{k+1}$. By definition, the oscillator phase increases at a constant rate equal to the natural frequency, $\mathrm{d}\varphi/\mathrm{d}t = \omega$, which is approximated by averaging over many oscillation cycles as $\omega = \langle 2\pi/(t_{k+1} - t_k)\rangle_k$. Repeating this analysis for each particle in isolation (i.e., one track at a time), we observed small systematic variations in the natural frequency ω_n with respect to the oscillator position n along the array (Fig. D.1c, solid markers). The spatial gradients in the oscillator frequency were caused by small deviations in the electrode alignment, which was controlled only to within ca. 1° of parallel. Particles oscillated faster where the electrodes were closer together due to an increase in field strength at those locations.

Despite variations in their natural frequencies, linear arrays of N particle oscillators moving simultaneously evolved in time to a phase-locked state, in which each particle moved with a common frequency (Fig. D.1c). Interestingly, the synchronized particles did not move in phase with one another but rather organized to form a single traveling wave, which remained stable for hundreds of oscillation cycles (Fig. D.1d; Supplemental Movie 1). Space-time plots of the oscillator phase $\varphi_n(t)$ show how this wave-like pattern emerged from a disordered initial configuration (Fig. D.1e; Supplementary Movie 2). The direction of wave propagation was related to the spatial gradient in the oscillators' natural frequencies: waves traveled from slower to faster

oscillators. Notably, the travelling wave patterns were robust to disturbances and recovered when disrupted by external perturbations (Supplementary Movie 3).

4.3 Results and Discussion

The stability of the synchronized state and the distribution of oscillator phases therein depended on the number of oscillators N in the array. For $N = 2$ oscillators, the particles moved in antiphase as reported previously [142] (Fig. D.2a). Such antiphase synchronization suggests that neighboring oscillators are coupled together by repulsive interactions such as the Coulombic forces between like-charged particles. As the number of particles was increased, the average phase difference between successive oscillators decreased giving rise to stable traveling waves with wavelengths spanning many oscillators (Fig. D.2b; see also Fig. S2 and Supplementary Movie 4). Beyond some critical number of oscillators N^*, the synchronized state became unstable (Fig. D.2c). Above this threshold, traveling waves were observed to grow and break near the center of the array in a periodic fashion (Supplementary Movie 5). Such breaking events are characterized by dislocation-like defects in the space-time plots for the oscillator phases (Fig. D.2c). The breaking frequency increased as the number of oscillators was increased beyond the stability threshold N^* (Fig. S3). For $N \gg N^*$, wave breaking was no longer periodic but rather occurred at irregular intervals and at different locations (Fig. S4 and Supplementary Movie 5).

To better understand the synchronized state, we quantified the distribution of oscillator phases for $N = N^*$ as a function of the electrode separation L and the oscillator spacing W. For each electrode configuration, we started with $N > N^*$ os-

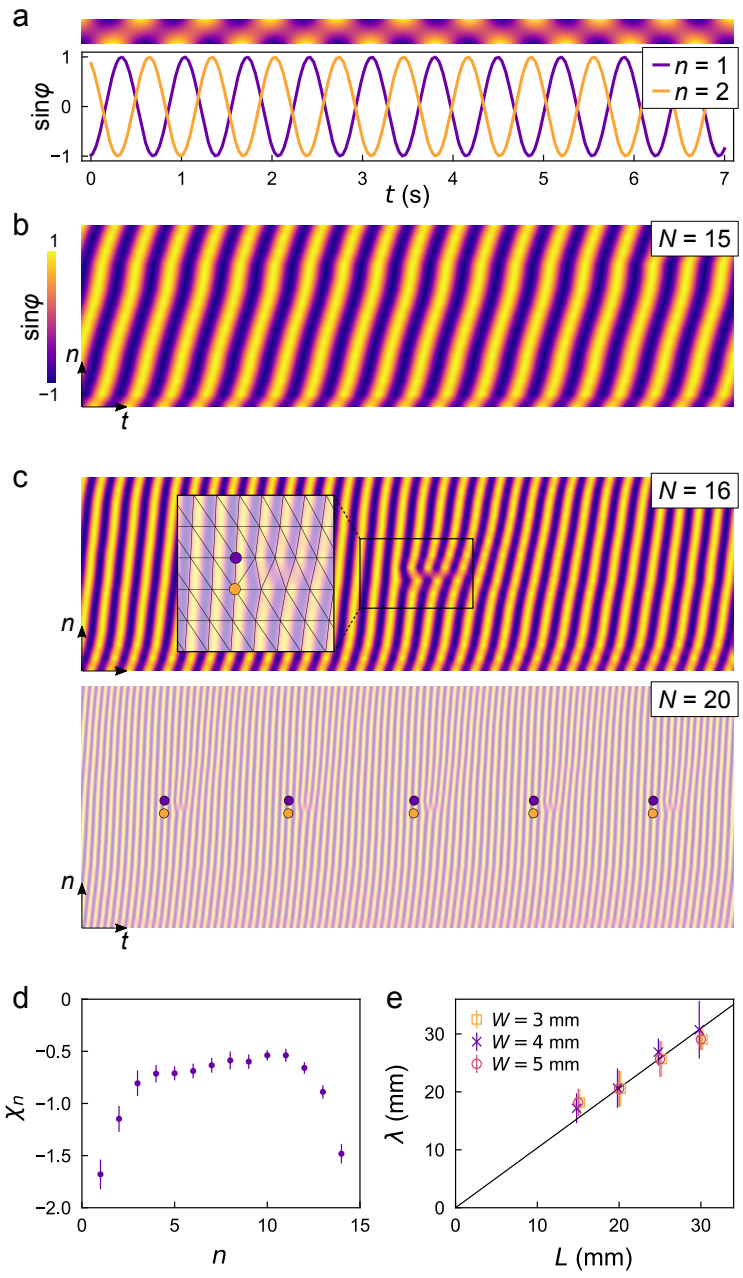

Figure 4.2: **Characterization of travelling waves.** (a) $N = 2$ oscillators moving in antiphase. The plot shows the sine of the oscillator phases (bottom); the space-time image shows the same data in a different way (top). (b) Space-time plot for $N = N^* = 15$ oscillators showing 20 oscillation cycles. (c) Space-time plots for $N > N^*$ showing defects that occur at regular time intervals. The markers show points in the space-time lattice with five-fold (purple) and seven-fold (yellow) coordination. (d) Time-averaged phase difference χ_n as a function of position n for $N = N^*$ oscillators. Data for (a-d) were collected with $L = 25$ mm, $W = 3$ mm, and $V = 18$ kV. (e) Characteristic wavelength λ as a function of the electrode separation L for $N = N^*$ and different oscillator spacings W. Error bars represent the standard deviation from

cillators and removed one particle at a time from the end of the array until reaching a stable synchronized state, at which the phase difference between neighboring oscillators was constant in time. Figure D.2d shows the time-averaged phase difference $\chi_n^{ss} = \langle \varphi_{n+1}(t) - \varphi_n(t) \rangle_t$ at the stationary state for a typical experiment. The phase difference was smallest (in magnitude) near the center of the array and largest near the edges. For each such state, we defined a characteristic wavelength in terms of the average phase difference as $\lambda = 2\pi W / \langle \chi_n^{ss} \rangle_n$. This wavelength increased linearly with the electrode spacing L but was independent of the oscillator spacing W over the range explored (Fig. D.2e).

The experimental observations are reproduced by a Kuramoto-like model [1] that accounts for the local repulsive coupling between neighboring oscillators and the systematic variations in their natural frequencies. In the model, we adopt the following simplified description of CCEP dynamics[125]. On contact with either electrode, a conductive sphere acquires a charge $q = \pm\frac{2}{3}\pi^3 \varepsilon a^2 E$, where E is the electric field at the electrode surface, and ε is the permittivity of the surrounding dielectric. This expression—first derived by Maxwell[141]—assumes that charge flows to/from the particle until its potential equals to that of the contacting electrode[55]. The electrostatic force on the particle is approximated as $F = qE$, which drives motion with velocity $U = F/\gamma$, where γ is a constant friction coefficient. Figure D.4a shows how the charge q and position h of a single oscillator depend on its phase $\varphi = \omega_o t$, where $\omega_o = \pi q_o E_o / \gamma L$ is the natural frequency defined in terms of the applied field $E_o = V/L$ and the Maxwell charge $q_o = \frac{2}{3}\pi^3 \varepsilon a^2 E_o$. By comparing the measured frequency in Fig. D.1c to the prediction of the model, the friction coefficient can be estimated to be $\gamma = 1.8 \times 10^{-3}$ N·s/m, which ca. 4 times larger than the Stokes drag, $\gamma_s = 6\pi\eta a$. The

increased drag is attributed to the solid boundaries formed by the patterned tracks and the planar electrodes (Fig. S5)[84].

The presence of neighboring oscillators influences both the charge that a particle acquires and the speed at which it moves. To describe these interactions, we decompose the electric field as $E = E_o + E'$, where E_o is the applied field and E' is a disturbance field due to neighboring particles, which are approximated as point charges (see Methods). In the limit of weak interactions (i.e., when $E' \ll E_o$), the moving particles are well approximated as phase oscillators with weak repulsive coupling between nearest neighbors. The phase of the n^{th} oscillator evolves in time as

$$\frac{\partial \varphi_n}{\partial t} = \omega_n + f(\varphi_n - \varphi_{n-1}) + f(\varphi_n - \varphi_{n+1}), \tag{4.1}$$

where ω_n is the natural frequency, and the function $f(\ )$ describes the phase-averaged interactions between neighboring oscillators as a function of their phase difference $\chi_n = \varphi_{n+1} - \varphi_n$. The boundaries of the array are open such that oscillators at the edges ($n = 1, N$) interact with only one neighbor [156]. We assume a uniform gradient in the natural frequency: $\omega_n = \omega_o + \Delta\left[n - \frac{1}{2}(N+1)\right]$ for $n = 1 \ldots N$, where ω_o is the mean oscillator frequency, and Δ is the frequency difference between successive oscillators due to a small angle θ between the electrodes ($\Delta/\omega_o \approx 3(W/L)\theta \ll 1$). Interestingly, this model was investigated previously as a possible explanation for traveling wave oscillations in the central pattern generator of the aquatic lamprey [39].

In the present context, the primary interaction between neighboring oscillators is electrostatic in origin; other interactions are neglected. In particular, the neglect of hydrodynamic interactions was supported by experiments in which neighboring parti-

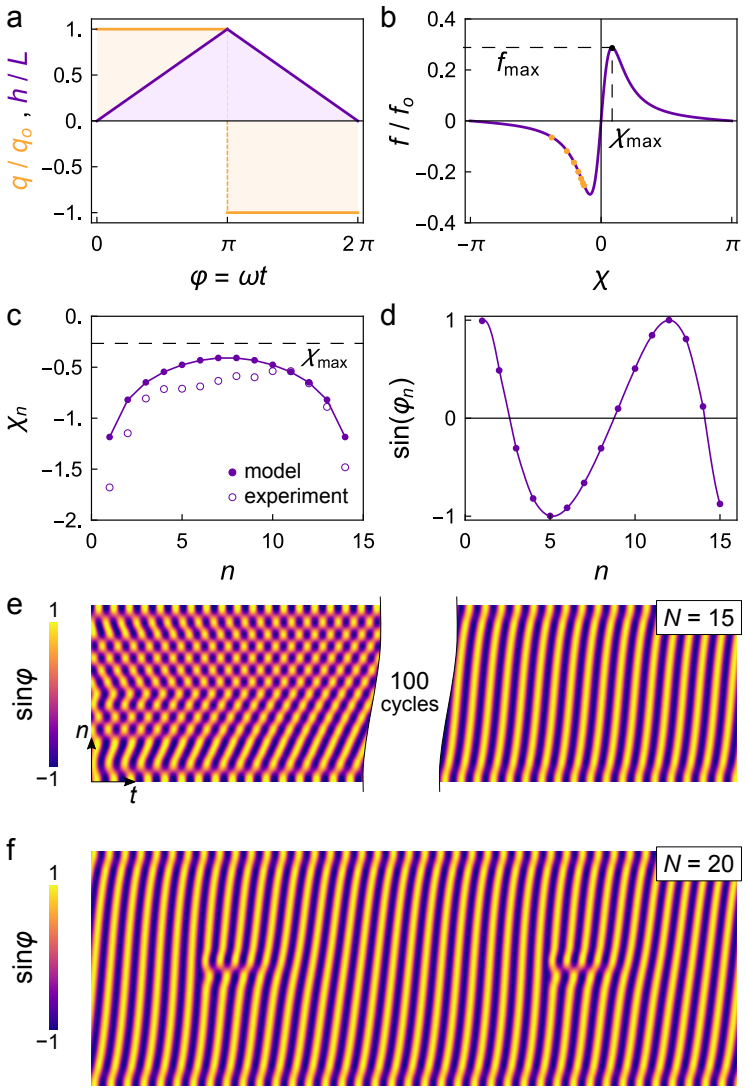

Figure 4.3: **Minimal model of traveling wave synchronization.** (a) Charge q and position h of a idealized CCEP oscillator as a function of phase φ. (b) Phase-averaged electrostatic interaction between two weakly-coupled CCEP oscillators as a function of their phase difference χ. The interaction is scaled by $f_o = q_o^2/\varepsilon W^2 L\gamma$; the oscillator spacing is $W = 0.12L$ as in Fig. 2. (c) Stable stationary solution for the phase difference χ_n of $N = 15$ oscillators. Experimental data from Fig. D.2d is reproduced for comparison; the predicted phase differences are plotted also in (b) to show their relationship with the interaction function $f(\ )$. (d) Sine of the oscillator phase φ_n showing the wave-like pattern. (e) Dynamics of the $N = 15$ oscillators starting from random initial conditions. (f) Oscillator dynamics for $N = 20$ showing the periodic breaking of the traveling waves comparable to that in Fig. D.2c. In (c)–(e) the critical oscillator number is $N^* = 15.5$ as in Fig. D.2b, corresponding to a frequency gradient $\Delta = 0.0096 f_o$. The natural frequency is $\omega_o = \frac{3}{2\pi^2}(W/a)^2 f_o = 1.4 f_o$

cles were separated by solid walls without altering their collective dynamics (Fig. S6). Approximating the particles as point charges, we compute the electrostatic interaction averaged over one oscillation cycle for a constant phase difference χ (see Methods). These repulsive interactions are described by an odd function characterized by the location $\chi_{\max}$ and height $f_{\max}$ of its maximum (Fig. D.4b). For large electrode separations ($L \gg W$), these quantities are well approximated as $f_{\max} \approx \frac{1}{2\sqrt{3}}(q_o^2/\varepsilon W^2 L\gamma)$ and $\chi_{\max} \approx \frac{\pi}{\sqrt{2}}(W/L)$. Our assumption of weak coupling implies that the phase velocity due to interactions is small compared to the natural frequency—that is, $f_{\max} \ll \omega_o$ or, equivalently, $a/W \ll 0.72$. Additional simulations incorporating the full amplitude dynamics provide further support for the phase oscillator approximation under the experimental conditions of $a/W = 0.33$ (Fig. S7).

The competition between the repulsive interactions and the frequency gradient leads to stable stationary solutions described by $f(\chi_n) = -\frac{1}{2}\Delta n(N-n)$ (see Methods). This solution exists provided that the number of oscillators is below some critical value $N^* = \sqrt{8f_{\max}/|\Delta|}$. Figure D.4c,d shows the stable solution in terms of the phase difference and the sine of the phase for $N = 15$ oscillators—just below the chosen critical value of $N^* = 16$. The addition of more particles ($N > N^*$) causes the waves to break periodically in the center of the array (Fig. D.4f). Physically, faster oscillators pile up behind the slower ones and are prevented from passing by the local repulsive interactions. In this way, the frequency gradient acts to compress the oscillator phases together to create longer waves that travel always from slower to faster oscillators. When compression by the frequency gradient exceeds the repulsive barriers between neighboring oscillators, global synchronization is lost and the waves break.

At the critical oscillator number ($N = N^*$), repulsive interactions are at their maximum ($\chi_n^{ss} \sim \chi_{\max}$), and the characteristic wavelength scales linearly with the electrode separation in agreement with experimental observations (Fig. D.2e)—that is, $\lambda \sim 2\pi W/\chi_{\max} \sim L$ for $W \ll L$. Moreover, the critical oscillator number observed in experiment implies a certain angle between the electrodes, which can be estimated from the model as $\theta = \frac{1}{3}(L\Delta/W\omega_o) = \frac{8\pi^2}{9\sqrt{3}}(a^2 L/W^3 N^{*2})$. For the conditions of Figure D.2, this angle is predicted to be $\theta = 1.1°$, which agrees well with that measured from the experimental images (Fig. D.1b). Smaller angles allow for stable waves containing more particles.

The average phase within the wave evolves in time at a constant rate equal to the average frequency ω_o, which is specified independently of the wavelength. In experiment, the oscillator frequency could be altered by changing the applied voltage; however, the range of accessible frequencies was limited by dielectric breakdown at higher voltages and by particle sticking at lower voltages[53]. Notably, the frequency of the phase locked state was slightly faster than the average natural frequency (Fig. D.1d). Dipolar interactions among the particles (neglected here) break the odd symmetry of the interaction function thereby altering the frequency of the synchronized state.

4.4 Conclusion

We have shown how arrays of electromechanical oscillators can organize spontaneously to form synchronized traveling waves of particle motion powered by a constant input voltage. The direction of wave propagation is determined by small gradients in the natural frequencies of the oscillators and can be controlled by introducing a

small angle between the otherwise parallel electrodes. The characteristic wavelength is approximately equal to the electrode separation L and corresponds to the largest possible wave that can be stabilized by repulsive interactions among the charged particles. The traveling wave motions are robust to perturbations and can be harnessed to direct the transport of material cargo. In particular, Figure 4 shows how traveling waves can direct the motion of gas bubbles floating at the interface just above the oscillating particles (see also Supplementary Movie 6). Bubbles are transported in the direction of wave propagation at speeds comparable to the wave velocity (Fig. D.5b). In contrast to previous strategies for rectifying CCEP motions based on ratcheted channels[57] or asymmetric particles[52], the present approach relies on the self-organization of multiple particles working in concert.

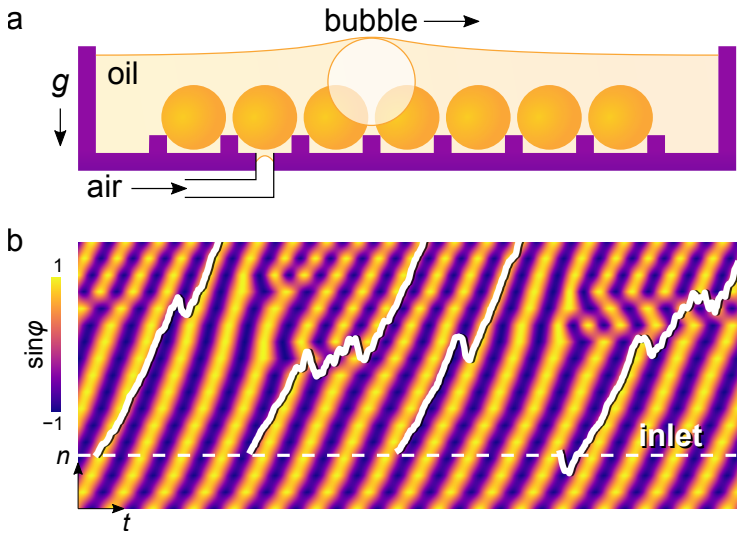

Figure 4.4: **Transport of air bubbles via travelling waves.** (a) Schematic illustration of the experimental set-up from the side. (b) Trajectories of four bubbles (white) superimposed over the space-time plot of the oscillator phase. See also Supplementary Movie 6.

Beyond this initial demonstration, traveling wave synchronization of CCEP oscillators may be useful for peristaltic pumping within microfluidic systems. Unlike standard pressure pumps, those based on traveling wave motions allow for recirculating flows[197] and would complement existing applications of CCEP in microfluidic cargo transport[57, 35], separations[57], and fluid mixing[31]. These CCEP-powered unit operations rely on constant voltages at low input power, which makes them attractive for use in portable, battery-powered microfluidic devices[13]. One important limitation of these oscillators is their reliance on the dielectric environment provided by non-polar fluids; CCEP motions cannot be sustained in even weakly conductive liquids such as deionized water[31]. However, recent advances in soft robotics suggest one strategy for circumventing this limitation by encapsulating non-polar liquids in stretchable, impermeable compartments[2]. These soft composite materials can be deformed by applying voltages to stretchable electrodes patterned on their surfaces. By incorporating arrays of CCEP oscillators within such dielectric compartments, it should be possible to create self-organized motions that drive transient deformations and thereby locomotion of soft robotic materials.

4.5 Methods

4.5.1 Experiment Set-up.

Periodic arrays of dielectric tracks were 3D printed in acrylonitrile butadiene styrene (ABS) with a period of $W = 3 - 5$ mm. The array was sandwiched between two copper plates separated by a distance $L = 10 - 30$ mm (McMaster-Carr 3350K201) and immersed in mineral oil (Sigma Aldrich CAS No. 8042-47-5). The tracks were

aligned perpendicular to the electrode surfaces and to the direction of gravity. Each track contained a single copper sphere (McMaster-Carr No. 64715K16, radius $a = 1$ mm), which rolled freely between the two electrodes (Fig. D.1a). Prior to use, the system was heated in a 60°C oven for several hours to remove any moisture. The copper electrodes were connected to a amplifier (Trek 20/20C) with an output voltage $V = 0 - 20$ kV. The particles were illuminated from below by a Light-emitting diodeLEDlight and their motions captured by a high-speed camera (Phantom V310). During each experiment, the electrodes were energized to a specified voltage and the resulting particle motions captured. The voltage was switched off for at least one minute between successive experiments to allow for the dissipation of any space charge accumulated on the surfaces of the tracks and/or the electrodes. Particle location data were extracted using standard image tracking routines in MATLAB.

Bubble Transport. Bubbles were generated within the oscillator array by a continuous flow of air supplied by a syringe pump at a rate of 0.2 ml/min. The air was delivered through a tube that connected to a hole in the base of one of the tracks (Fig. D.5a). The bubbles (ca. 4 mm in diameter) were transported down the length of the array by the coordinated motions of $N = 17$ particles of radius $a = 1.5$ mm (Supporting Video 6). In these experiments, the applied voltage was $V = 18$ kV, the electrode separation was $L = 20$ mm, and the height of the mineral oil above the base of the track was 4 mm. Bubbles were always transported in the direction of wave propagation, which was controlled by introducing a finite angle between the two electrodes. Control experiments with no applied voltage showed no bubble motion in either direction.

4.5.2 Electrostatic Interactions.

We first consider a single point charge q positioned at a height $z = h$ between two grounded planes at $z = 0$ and $z = L$. The resulting electrostatic potential at point $\boldsymbol{x}$ is

$$\phi(\boldsymbol{x}) = \frac{q}{\pi L \varepsilon} \sum_{m=1}^{\infty} \sin\left(\frac{m\pi h}{L}\right) \sin\left(\frac{m\pi z}{L}\right) K_0\left(\frac{m\pi r}{L}\right), \tag{4.2}$$

where $r = \sqrt{x^2 + y^2}$ is the radial distance from the charge, and $K_0(\ )$ is the zeroth order modified Bessel function of the second kind. For large arguments, the Bessel function decays exponentially as $K_0(s) \to e^{-s}\sqrt{\pi/2s}$; the infinite series can be truncated for some $m \gg L/\pi r$ to obtain an accurate approximation. The corresponding electric field in the z-direction is given by $E_z = -\partial\phi/\partial z$.

We now consider how the disturbance field E' due to one oscillator i influences the dynamics of another oscillator j in the limit of weak coupling. At zeroth order in E', the phase of each oscillator increases at a constant rate ω_o such that $\varphi_i = \omega_o t$ and $\varphi_j = \omega_o t + \chi$, where $\chi = \varphi_j - \varphi_i$ is the constant phase difference. The charge $q = q(\varphi)$ and position $h = h(\varphi)$ of each oscillator depends on the phase as shown in Figure D.4a. At first order in E', the disturbance in the phase of oscillator j evolves as

$$\frac{d\varphi_j'}{dt} = \frac{\pi n(\varphi_j)}{L\gamma} \left[q(\varphi_j) E'(\varphi_i, \varphi_j) + q'(\varphi_i, \varphi_j) E_o + \dots \right], \tag{4.3}$$

where the factor $\pi n(\varphi_j)/L\gamma$ relates the electric force to the corresponding phase velocity with $n(\varphi_j) = \pm 1$ indicating the direction of travel. The bracketed terms describe two types of electrostatic interactions. First, the disturbance field due to particle i drives particle j to move faster or slower between the electrodes. Using the

point charge solution (4.2), this disturbance $E'(\varphi_i, \varphi_j)$ is given by

$$E'(\varphi_i, \varphi_j) = -\frac{q(\varphi_i)}{L^2 \varepsilon} \sum_{m=1}^{\infty} m \sin\left(\frac{m\pi h(\varphi_i)}{L}\right) \cos\left(\frac{m\pi h(\varphi_j)}{L}\right) K_0\left(\frac{m\pi W}{L}\right), \quad (4.4)$$

where W is the oscillator spacing. Second, the disturbance field due to particle i alters the charge acquired by particle j on contact with either electrode; the disturbance charge $q'(\varphi_i, \varphi_j)$ is given by

$$q'(\varphi_i, \varphi_j) = \begin{cases} +\frac{2}{3}\pi^3 \varepsilon a^2 E'(-\chi, 0) & 0 \le \varphi_j < \pi \\ -\frac{2}{3}\pi^3 \varepsilon a^2 E'(\pi - \chi, \pi) & \pi \le \varphi_j < 2\pi \end{cases}. \quad (4.5)$$

Physically, the charge on particle j is determined by its most recent contact with either electrode ($\varphi_j = 0$ or π); the field due to particle i at the time of that contact determines the disturbance charge.

We can now average these two interactions over one oscillation cycle to obtain the phase-averaged interaction function,

$$f(\chi) = \frac{\pi}{L\gamma} \frac{1}{2\pi} \int_0^{2\pi} n(\varphi_j) \left[q(\varphi_j) E'(\varphi_j - \chi, \varphi_j) + q'(\varphi_j - \chi, \varphi_j) E_o\right] d\varphi_j. \quad (4.6)$$

Carrying out the integration, each of the two electrostatic interactions produce contributions of the same mathematical form with the second term contributing twice that of the first,

$$f(\chi) = \frac{3\pi q_o^2}{2\varepsilon L^3 \gamma} \sum_{m=1}^{\infty} m \sin(m\chi) K_0\left(\frac{m\pi W}{L}\right). \quad (4.7)$$

This final expression is plotted in Figure D.4b for the case of $W/L = 0.12$.

4.5.3 Stationary Solution.

Starting from Eq. (4.1), we recast the oscillator dynamics in terms of the phase difference $\chi_n = \varphi_{n+1} - \varphi_n$ and the average phase $\Phi = \frac{1}{N} \sum_n \varphi_n$. Taking the difference

in the phase dynamics of successive oscillators, we obtain the following equation for the phase difference

$$\frac{\partial \chi_n}{\partial t} = \Delta - f(\chi_{n-1}) + 2f(\chi_n) - f(\chi_{n+1}) \quad \text{for } n = 2, \ldots, N-2, \tag{4.8}$$

which makes use of the fact that $f(\ )$ is an odd function. At the open boundaries of the array, the phase difference evolves as

$$\frac{\partial \chi_1}{\partial t} = \Delta + 2f(\chi_1) - f(\chi_2) \quad \text{and} \quad \frac{\partial \chi_{N-1}}{\partial t} = \Delta - f(\chi_{N-2}) + 2f(\chi_{N-1}). \tag{4.9}$$

In addition to these $N-1$ equations, the dynamics of the N oscillators is described by the that of the average phase, $\partial\Phi/\partial t = \omega_o$, which is fully decoupled from the phase differences. Setting the time derivatives in Eqs. (4.8) and (4.9) equal to zero, the resulting recurrence equation can be solved to obtain the stationary solution, $f(\chi_n) = \frac{1}{2}\Delta n(n-N)$, presented in the main text. As detailed in the Supplementary Information, this solution exists provided that $f_{\max} > \frac{1}{8}N^2|\Delta|$ and is stable when $f'(\chi_n) < 0$. The characteristic relaxation time for approaching the stationary state is given by the diffusive-like scaling relation $\tau \sim \chi_{\max} N^2/\pi^2 f_{\max}$.

Chapter 5

Shape directed colloidal clusters via Contact Charge Electrophoresis

5.1 Introduction

[1]Simple energy inputs via Contact Charge Electrophoresis are capable of driving complex particle motions through dielectric environments due to symmetry and shape of colloidal particles. The capability to taylor trajectories of colloidal cluster by coupling their shape to hydrodynamics and electrostatics of the system gives us tools to design complex microfluidic systems that can perform operations like sensing, transport, mixing etc. In this chapter we systematically investigate the dynamics of cluster comprising multiple spherical conductive particles driven via contact charge electrophoresis (CCEP). We are specifically interested in understanding dynamics of

[1]The material presented in this chapter is in process of preparation with permission from Shashank Pandey, Ghanim Hableel and K.J.M. Bishop. Author responsibilities were as follows: K.J.M.B, G.H. and S.P. performed the simulations. G.H. and S.P. developed the theoretical model and performed the experiments. S.P., G.H., and K.J.M.B. conceived the project and wrote the paper.

closed packed cluster of particles with or without few non-conductive particles in three dimensions (3D).

5.2 Theory and Formulation for rigid body dynamics

The equation of motion for the cluster of closed particles is represented in the form shown below:

$$U = M_{UF} \cdot F + M_{UT} \cdot T, \tag{5.1}$$

$$\Omega = M_{\Omega F} \cdot F + M_{\Omega T} \cdot T. \tag{5.2}$$

where U and Ω represent the velocity and angular velocity of the cluster while F and T denote the force and torque on the cluster with their relation represented in form of Mobility tensors eg. "M_{UF}" for the tensor relating velocity and force on the cluster.

Since the cluster consist of few or all conductive particles placed in a dielectric media between two parallel electrode, the force and torque represented in 5.1 and 5.2 are generated due to the electrostatics and are given as shown below.

We consider a conductive particle immersed in a dielectric medium and subject to a uniform external field $\boldsymbol{E}^{\infty}$. The disturbance potential $\phi(\boldsymbol{x})$ due to the particle is governed by the Laplace equation

$$\nabla^2 \phi = 0 \tag{5.3}$$

Far from the particle, the disturbance potential decays to zero

$$\phi(\boldsymbol{x}) = -\boldsymbol{x} \cdot \boldsymbol{E}^{\infty} \quad \text{for } x \to \infty \tag{5.4}$$

Along the particle surface $\mathcal{S}$, the potential is constant and equal to the particle potential Φ less the external potential Φ^∞

$$\phi(\boldsymbol{x}) = \Phi - \Phi_o^\infty \quad \text{for } \boldsymbol{x} \in \mathcal{S} \tag{5.5}$$

where the external potential is evaluated at the particle origin, $\Phi_o^\infty = -\boldsymbol{x}_o \cdot \boldsymbol{E}^\infty$. This problem can be decomposed into two sub-problems:

$$\nabla^2 \phi' = 0 \tag{5.6}$$

$$\phi'(\boldsymbol{x}) = 1 \quad \text{for } \boldsymbol{x} \in \mathcal{S} \tag{5.7}$$

$$\phi'(\boldsymbol{x}) = 0 \quad \text{for } x \to \infty \tag{5.8}$$

and

$$\nabla^2 \boldsymbol{\phi}_o'' = 0 \tag{5.9}$$

$$\boldsymbol{\phi}_o''(\boldsymbol{x}) = 0 \quad \text{for } \boldsymbol{x} \in \mathcal{S} \tag{5.10}$$

$$\boldsymbol{\phi}_o''(\boldsymbol{x}) = -(\boldsymbol{x} - \boldsymbol{x}_o) \cdot \boldsymbol{\delta} \quad \text{for } x \to \infty \tag{5.11}$$

where $\boldsymbol{\delta}$ is the identity tensor. The total electric potential is then given by

$$\phi = \phi'(\Phi - \Phi_o^\infty) + \boldsymbol{\phi}_o'' \cdot \boldsymbol{E}^\infty \tag{5.12}$$

The subscripts o serve to remind us that these quantities depend on the location of the origin $\boldsymbol{x}_o$.

5.2.1 Hydrodynamics of Rigid Particles

We consider a rigid particle moving through an unbounded quiescent fluid at low Reynolds numbers. The linear velocity $\boldsymbol{U}$ and angular velocity $\boldsymbol{\Omega}$ are linearly related

to the external force $\boldsymbol{F}$ and torque $\boldsymbol{T}$ acting on the particle as

$$\begin{bmatrix} \boldsymbol{F} \\ \boldsymbol{T} \end{bmatrix} = \begin{bmatrix} \boldsymbol{R}_{UF} & \boldsymbol{R}_{UT} \\ \boldsymbol{R}_{\Omega F} & \boldsymbol{R}_{\Omega T} \end{bmatrix} \cdot \begin{bmatrix} \boldsymbol{U} \\ \boldsymbol{\Omega} \end{bmatrix} \tag{5.13}$$

where the $\boldsymbol{R}$ are resistance tensors. The translation tensor $\boldsymbol{R}_{UF}$ and the rotation tensor $\boldsymbol{R}_{\Omega T}$ are symmetric; the coupling tensors $\boldsymbol{R}_{\Omega F}$ and $\boldsymbol{R}_{UT}$ are related as

$$\boldsymbol{R}_{UF} = \boldsymbol{M}_{UF}^{\dagger}, \qquad \boldsymbol{M}_{\Omega T} = \boldsymbol{M}_{\Omega T}^{\dagger}, \qquad \boldsymbol{M}_{\Omega F} = \boldsymbol{M}_{UT}^{\dagger}, \tag{5.14}$$

where † denotes the transpose. Importantly, these tensors share the symmetry of the particle and are uniquely specified by its shape and orientation.

To describe the rigid-body motion of the particle, we introduce two coordinate systems: a stationary system and a moving system, which is fixed to the particle and participates in its motion. The origin of the moving system is chosen such that the coupling tensor $\boldsymbol{M}$ to be the 'center of hydrodynamic resistance'.

A vector $\boldsymbol{v}'$ expressed in the moving system is related to the same vector $\boldsymbol{v}$ in the stationary system as $v_i' = R_{ij} v_j$ where $\boldsymbol{R}$ is an orthogonal rotation matrix that depends on the orientation of the particle. Similarly, the components of the mobility tensors in the stationary system are related to those in the moving system as

$$M_{ij} = R_{pi} R_{qj} M_{pq}'. \tag{5.15}$$

The components M_{pq}' are independent of particle orientation and depend only on particle shape. Knowledge of these constants allows for computation of the particle trajectory in accordance with equations (5.13) and the kinematics of rigid-body motion.

Within the particle frame of reference, the mobility tensors are constant but depend on the choice of origin, denoted $\boldsymbol{x}_O$ in the laboratory frame.

These mobility tensors share the symmetry of the particle and are therefore invariant to symmetry operations that leave the particle unchanged.

5.2.2 Electrostatics of Conductive Particles

We consider a conductive particle immersed in a dielectric medium and subject to a uniform external field $\boldsymbol{E}^{\infty}$. The disturbance potential $\phi(\boldsymbol{x})$ due to the particle is governed by the Laplace equation

$$\nabla^2 \phi = 0 \tag{5.16}$$

Far from the particle, this disturbance decays to zero

$$\phi(\boldsymbol{x}) = 0 \quad \text{for } x \to \infty \tag{5.17}$$

Along the particle surface $\mathcal{S}$, the particle potential is constant Φ such that the disturbance in the externally applied potential is

$$\phi(\boldsymbol{x}) = \Phi + \boldsymbol{x} \cdot \boldsymbol{E}^{\infty} \quad \text{for } \boldsymbol{x} \in \mathcal{S} \tag{5.18}$$

This problem can be decomposed into two sub-problems:

$$\nabla^2 \phi' = 0 \tag{5.19}$$

$$\phi'(\boldsymbol{x}) = 1 \quad \text{for } \boldsymbol{x} \in \mathcal{S} \tag{5.20}$$

$$\phi'(\boldsymbol{x}) = 0 \quad \text{for } x \to \infty \tag{5.21}$$

and

$$\nabla^2 \boldsymbol{\phi}_o'' = 0 \tag{5.22}$$

$$\boldsymbol{\phi}_o''(\boldsymbol{x}) = \boldsymbol{x} - \boldsymbol{x}_o \quad \text{for } \boldsymbol{x} \in \mathcal{S} \tag{5.23}$$

$$\boldsymbol{\phi}_o''(\boldsymbol{x}) = 0 \quad \text{for } x \to \infty \tag{5.24}$$

where $\boldsymbol{x}_o$ is the particle origin. The disturbance potential is given by

$$\phi = \phi'(\Phi - \Phi_o^\infty) + \boldsymbol{\phi}_o'' \cdot \boldsymbol{E}^\infty \tag{5.25}$$

where the external potential is evaluated at the particle origin, $\Phi_o^\infty = -\boldsymbol{x}_o \cdot \boldsymbol{E}^\infty$. The subscripts o serve to remind us that these quantities depend on the location of the origin $\boldsymbol{x}_o$.

Charge and Dipole. By Gauss's law, the charge on the particle is

$$q = -\varepsilon \int_{\mathcal{S}} \boldsymbol{n} \cdot \nabla\phi d\mathcal{S} \tag{5.26}$$

where $\boldsymbol{n}$ is the unit normal vector directed out from the particle, and ε is the permittivity of the dielectric medium. Substituting equation (5.25) for the potential, the charge is linearly related to the particle potential and to the applied field as

$$q = C_{q\Phi}(\Phi - \Phi_o^\infty) + \boldsymbol{C}_{qE}^o \cdot \boldsymbol{E}^\infty \tag{5.27}$$

where the capacitance coefficients are

$$C_{q\Phi} = -\varepsilon \int_{\mathcal{S}} \boldsymbol{n} \cdot \nabla\phi' d\mathcal{S} \tag{5.28}$$

$$\boldsymbol{C}_{qE}^o = -\varepsilon \int_{\mathcal{S}} \boldsymbol{n} \cdot \nabla\boldsymbol{\phi}_o'' d\mathcal{S} \tag{5.29}$$

Similarly, the dipole moment $\boldsymbol{p}_o$ relative to the particle origin $\boldsymbol{x}_o$ is

$$\boldsymbol{p}_o = -\varepsilon \int_{\mathcal{S}} (\boldsymbol{x} - \boldsymbol{x}_o)\boldsymbol{n} \cdot \nabla\phi d\mathcal{S} \tag{5.30}$$

Like the monopole, the dipole depends linearly on the particle potential and the external field

$$\boldsymbol{p}_o = C_{p\Phi}^o(\Phi - \Phi^\infty) + \boldsymbol{C}_{pE}^o \cdot \boldsymbol{E}^\infty \tag{5.31}$$

where the capacitance coefficients are

$$\boldsymbol{C}^o_{p\Phi} = -\varepsilon \int_{\mathcal{S}} (\boldsymbol{x} - \boldsymbol{x}_o)\boldsymbol{n} \cdot \nabla \phi' d\mathcal{S} \tag{5.32}$$

$$\boldsymbol{C}^o_{pE} = -\varepsilon \int_{\mathcal{S}} (\boldsymbol{x} - \boldsymbol{x}_o)\boldsymbol{n} \cdot \nabla \boldsymbol{\phi}''_o d\mathcal{S} \tag{5.33}$$

Capacitance Tensor. To summarize, the moments of the surface charge are linearly related to the particle potential and the external field by a grand capacitance tensor $\mathcal{C}$

$$\begin{bmatrix} q \\ \boldsymbol{p}_o \end{bmatrix} = \begin{bmatrix} C_{q\Phi} & \boldsymbol{C}^o_{qE} \\ \boldsymbol{C}^o_{p\Phi} & \boldsymbol{C}^o_{pE} \end{bmatrix} \cdot \begin{bmatrix} \Phi - \Phi^\infty_o \\ \boldsymbol{E}^\infty \end{bmatrix} \tag{5.34}$$

The tensor $\mathcal{C}$ is symmetric such that

$$C^o_{qE,i} = C^o_{p\Phi,i} \tag{5.35}$$

$$C^o_{pE,ij} = C^o_{pE,ji} \tag{5.36}$$

The first of these results follows from the definitions (5.29) and (5.32) and the reciprocal relation

$$\int_{\mathcal{S}} \boldsymbol{n} \cdot (\phi' \nabla \phi''_{o,i} - \phi''_{o,i} \nabla \phi') d\mathcal{S} = 0 \tag{5.37}$$

Similarly, equation (5.36) follows from the definition (5.33) and a different reciprocal relation (5.32)

$$\int_{\mathcal{S}} \boldsymbol{n} \cdot (\phi''_{o,i} \nabla \phi''_{o,j} - \phi''_{o,j} \nabla \phi''_{o,i}) d\mathcal{S} = 0 \tag{5.38}$$

Center of Charge. The components of the capacitance tensor depend on the choice of the particle origin. The vector $\boldsymbol{C}^o_{p\Phi}$ can be written as

$$\boldsymbol{C}^o_{p\Phi} = \boldsymbol{C}_{p\Phi} - \boldsymbol{x}_o C_{q\Phi} \tag{5.39}$$

where $\boldsymbol{C}_{p\Phi}$ is defined relative to the origin $\boldsymbol{x}_o = 0$

$$\boldsymbol{C}_{p\Phi} = -\varepsilon \int_{\mathcal{S}} \boldsymbol{x} \left(\boldsymbol{n} \cdot \nabla \phi'\right) d\mathcal{S} \tag{5.40}$$

Similarly, the vector $\boldsymbol{C}^o_{qE}$ can be written as

$$\boldsymbol{C}^o_{qE} = \boldsymbol{C}_{qE} - \boldsymbol{x}_o C_{q\Phi} \tag{5.41}$$

where $\boldsymbol{C}_{qE}$ is defined as

$$\boldsymbol{C}_{qE} = -\varepsilon \int_{\mathcal{S}} \left(\boldsymbol{n} \cdot \nabla \boldsymbol{\phi}''\right) d\mathcal{S} \tag{5.42}$$

with $\boldsymbol{\phi}''(\boldsymbol{x}) = \boldsymbol{x}$ on the surface of the particle. Finally, the tensor $\boldsymbol{C}^o_{pE}$ can be expressed as

$$C^o_{pE,ij} = C_{pE,ij} - x^o_i C_{qE,j} - x^o_j C_{p\Phi,i} + x^o_i x^o_j C_{q\Phi} \tag{5.43}$$

where $\boldsymbol{C}_{pE}$ is defined as

$$\boldsymbol{C}_{pE} = -\varepsilon \int_{\mathcal{S}} \boldsymbol{x} \left(\boldsymbol{n} \cdot \nabla \boldsymbol{\phi}''\right) d\mathcal{S} \tag{5.44}$$

There exists a particular choice of origin such that the coupling vector, $\boldsymbol{C}^o_{qE} = \boldsymbol{C}^o_{p\Phi}$, between the charge and the dipole vanish—namely,

$$\boldsymbol{x}_c = \boldsymbol{C}_{qE} / C_{q\Phi} \tag{5.45}$$

We refer to this position as the particle's 'center of charge'. Substituting this result into equation (5.43), we obtain the following expression for the polarizability tensor relative to the center of charge

$$C^c_{pE,ij} = C_{pE,ij} - C_{p\Phi,i} C_{p\Phi,j} / C_{q\Phi} \tag{5.46}$$

Electric Force and Torque. For a particle of constant charge q in a constant field $\boldsymbol{E}^{\infty}$, the force and torque on the particle are

$$\boldsymbol{F} = q\boldsymbol{E}^{\infty} \tag{5.47}$$

$$\boldsymbol{T}_o = \boldsymbol{p}_o \times \boldsymbol{E}^{\infty} \tag{5.48}$$

In general, the dipole moment can be expressed in terms of the known charge q and field $\boldsymbol{E}^{\infty}$ as

$$\boldsymbol{p}_o = \frac{\boldsymbol{C}^o_{p\Phi}}{C_{q\Phi}} \left(q - \boldsymbol{C}^o_{qE} \cdot \boldsymbol{E}^{\infty} \right) + \boldsymbol{C}^o_{pE} \cdot \boldsymbol{E}^{\infty} \tag{5.49}$$

If the particle origin is chosen to be zero, then the dipole becomes

$$\boldsymbol{p} = q\boldsymbol{x}_c + \boldsymbol{C}^c_{pE} \cdot \boldsymbol{E}^{\infty} \tag{5.50}$$

where $\boldsymbol{x}_c$ is the location of the center of charge. The torque about the origin at zero is

$$\boldsymbol{T} = \boldsymbol{p} \times \boldsymbol{E}^{\infty} = \boldsymbol{x}_c \times q\boldsymbol{E}^{\infty} + \boldsymbol{p}_c \times \boldsymbol{E}^{\infty} \tag{5.51}$$

Particle Symmetry. When the origin of the particle is taken as the center of charge $\boldsymbol{x}_c$, the relation between the moments of the surface charge, the particle potential, and the external field becomes

$$\begin{bmatrix} q \\ \boldsymbol{p}_c \end{bmatrix} = \begin{bmatrix} C_{q\Phi} & 0 \\ 0 & \boldsymbol{C}^c_{pE} \end{bmatrix} \cdot \begin{bmatrix} \Phi - \Phi^{\infty}_c \\ \boldsymbol{E}^{\infty} \end{bmatrix} \tag{5.52}$$

In general, the capacitance tensor is characterized by seven parameters. Invariance of the particle shape with respect to the operation $\boldsymbol{Q}$ implies the following relationship among the components of the capacitance tensor

$$\boldsymbol{C}^c_{pE} = \boldsymbol{Q}^T \cdot \boldsymbol{C}^c_{pE} \cdot \boldsymbol{Q} \tag{5.53}$$

Chapter 6

Future of Multiple particle Contact Charge Electrophoresis systems

6.1 Introduction

All the previous chapters have shown the modeling[Chapter 2, 3] and utilization of multiple particle contact charge electrophoresis systems leading to an emergent organization for dispersion of particles[Chapter 4] like chain formation for the unrestricted system of dispersion of colloids and formation of traveling waves in the case of restricted dispersion as well as controlled actuation of clusters/aggregates[Chapter 5] using the shape of the particles and effect of confinement on their trajectory. I have demonstrated in the prior chapters the advantage of coupling the CCEP motion with shape of the colloidal cluster and how restricted dispersion of particles that interact via electrostatic force can lead to emergent behaviours that can be utilized for various applications in mixing, pumping and cargo transport at micro-scale. Furthermore CCEP is independent of scale so most of these ideas can be transferred to much larger or much smaller scales in contrast to other traditional electrostatic manipulation tech-

niques like Dielectrophoresis(DEP) and Induced charge electrophoresis(ICEP).

6.2 Emergence of traveling waves in restricted multiple particle systems

Chapter 4 discusses the emergence of traveling wave like patterns that emerge when an array of conductive particles are restricted from direct contact, by making racetrack like grooves perpendicular to pair of electrodes. This dynamic self assembly of CCEP oscillators was shown to perform cargo transport tasks illustrated via bubble transport example. Here we explore an extension of this idea and other more sophisticated tasks this mechanism is capable of performing.

6.2.1 Soft robotic applications

Electroactive polymers are soft composite materials that can be deformed by applying voltages to stretchable electrodes patterned on their surfaces. By incorporating arrays of CCEP oscillators within such dielectric compartments, it should be possible to create self-organized motions that drive transient deformations and thereby locomotion of soft robotic materials.

6.2.2 Pumping and propulsion

Unlike standard pressure pumps the pumps based on traveling wave motions allow for recirculating flows and would complement existing applications of CCEP in microfluidic unit operations. Also we performed some preliminary experiments that reveal using the traveling waves generated on a movable platform with the linear assembly of

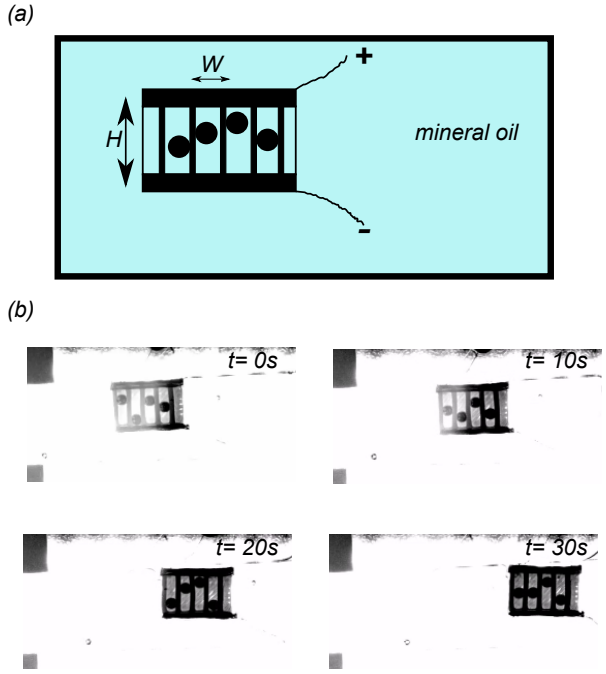

Figure 6.1: **Traveling wave propulsion of mobile setup**(a) Schematic of setup showing conductive particles sandwiched between two parallel plate electrodes with constant potential on racetrack like groves free to move on the petridish filled with dielectric media, where V= 8kV, Particle radius = 1.25mm, W = 3mm, H = 10mm. (b) The timestamp illustrates the motion of the setup in the petridish due to the propulsion by traveling waves.

oscillators to propel the platform itself when whole setup is placed in a non-conducting fluid. The setup with fewer number of particles is placed on fluorinated high density oil-mineral oil interface and the voltage is switched on leading to formation of a traveling wave in a particular direction which leads to fluid being ejected in opposite direction hence propelling the setup as shown in Figure 6.1. Maybe this idea can be further explored leading to more sophisticated microfluidic robotic applications.

6.2.3 Extension to two dimensional systems of oscillators

Chapter 4 discusses illustrates the idea that traveling waves created via assembly of linear oscillators can perform intricate tasks like propulsion, transport and pumping so here we explore bit further into the regime of two dimensional oscillator that showcase even more abundant emerging patterns and frustrations due to accommodation of multitude of these patterns.

6.2.3.1 Frustration in phase repulsive oscillators

Before we talk about possible applications of 2D oscillator systems lets dive into how and what kind of patterns can be generated as well as what kind of complications need to be expected. First of all it should be kept in mind that these system of oscillator have a phase-repulsive dynamics in its oscillator network that leads to a positive total frustration and whose value strongly depends on the details of network topology. So in order to quantify it, we resort to a different link-based measure of the collective dynamics. Now taking the ideas from disordered systems terminology, the frustration has been defined in work of other authors as $local frustration, f_{ijk} = 1 - cos(_{ijjk})$ and $total frustration, F = 1/L \sum f_{ijk}$ providing a good way to quantify the state of the dynamical system with either travelling waves or anti-phase or mixer of two, for the cases of complete anti-phase at all oscillator or traveling waves the value of frustration would be 0 while for the case with traveling waves with different phase differences or mixer of traveling wave and anti-phase mode the value of frustration would be non-zero. Determining the frustration in system can help us understand which and how many different kind of stable states exist in our system, which can further be utilized to tailor patterns that can in turn perform tasks like manipulation

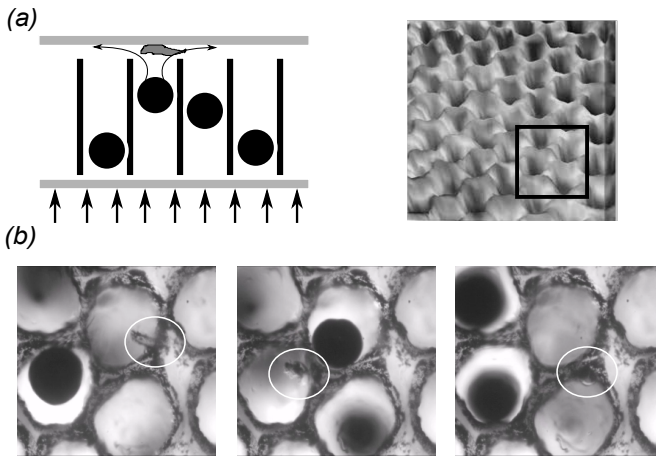

Figure 6.2: **2D Manipulation of blob** (a) Conductive spheres immersed in mineral oil oscillate along dielectric tracks connecting two plane electrodes subject to a constant voltage V with a small blob trapped between the surface of electrode and the CCEP performing particle. The other diagram on the right illustrates the honeycomb lattice being used as well as the black square focuses the region of interest for presented result. (b) The snapshots illustrate that as the particles in the adjacent tracks perform anti-synchronous motion they change the position of the suspended blob/particle.

as illustrated in Figure 6.2.

6.2.3.2 Stability of emergent states and patterns

We also explored specifically the system of ring lattice with nearest neighbor. Considering a generalized case for attractive;$K < 0$ and repulsive oscillator;$K > 0$ which have fixed point solutions for all values $\theta_{equi} = 2\pi n/N$. To determine the stability of these solutions we note that the Jacobian is a circulant matrix , for which the eigenvalues are easily computable And for ring topology we find $_m$ =

$4Ksin2(m\pi/N)cos\theta_{equi}; m = 0, 1, ..., N1$. Since sin(m/n) is always positive and K is positive because of repulsive interaction, the stability depends only on the phase difference θ_{equi}. For values of $K > 0$, all values of θ_{equi} between $\pi/2$ and $3\pi/2$ are stable, It should be noted that while $\theta_{equi} = \pi$ is the most stable phase configuration for $K > 0$, it is not accessible for systems with odd numbers of oscillators. Contrast this with the case of $K < 0$ where the most stable state, $\theta = 0$, is accessible for any number of oscillators.

6.3 Chain formation or bucket brigade system for unrestricted multiple particle system

When a collection of multiple conductive particles are dispersed in a non-conducting dielectric media between two electrodes they tend to form chain like structures at low particle volume fractions, these formations are also known by the phrase bucket brigade (from Chapter 1). Which refers to a method of transporting items wherein items are passed from one stationary member of the brigade to the next. A conceptually similar behavior occurs during CCEP of multiple particles, which organize to pass charge from one electrode to the other. In one realization, multiple aluminum discs were distributed randomly on the surface of a dielectric liquid between two electrodes. Upon application of the field, the discs organized to form linear chains which oscillate continuously, passing charge from neighbor to neighbor. Similar behaviors have been observed for water drops moving in oil between two electrodes. Importantly, the number of particles in the chain cannot exceed L/2a; otherwise, they will span the gap between the electrode and short the circuit. This phenomenon of chain

formation begins with formation of multiple chains which finally collapse together to generate a large single chain there by short circuiting the system. Understanding the timescale of rate at which these smaller chains merge to form larger ones can possibly be utilized to control and manipulate the short circuits in transformer oils with metallic impurities etc. Another idea involves considering these particles as charge-phonons since they carry charge in a periodic manner and lead to change in amount of current that flows through the circuit leading to controlled conduction or current in the device (discussed in Chapter 2).

6.4 Future of CCEP in clusters and aggregates

Utilizing particle shape to direct the motion of active colloids is generally applicable to any energy input or propulsion mechanism either it be chemical, electrical or magnetic. As discussed in Chapter 5 we utilize CCEP to power these aggregates that rectify their motion both due to their shape and presence of walls leading to very interesting trajectories. These tailored trajectories can be used to several microfluidic tasks like sensing, tracking, mixing and transport.

6.5 Conclusion

In the presented dissertation I explored the various cases involving dynamics and modeling of multiple particles using simple CCEP mechanism as the motor. Starting off in Chapter 1 which covered the motivation for both single particle and multiple particle CCEP and how it can be used for tasks like mixing, actuation, separation and transport while predicting new horizons for the multiple particle systems. Chapter 2

and Chapter 3 explore those horizons for all possible cases of multiple particle systems for e.g. restricted dispersion, unrestricted dispersion and aggregates. Finally Chapter 4 and Chapter 5 explore in more details about formation of these emergent behaviours and their utility in microfluidic applications.

Bibliography

[1] J. A. Acebrón, L. L. Bonilla, C. J. P. Vicente, F. Ritort, and R. Spigler. The Kuramoto model: A simple paradigm for synchronization phenomena. *Rev. Mod. Phys.*, 77(1):137–185, 2005.

[2] E. Acome, S. Mitchell, T. Morrissey, M. Emmett, C. Benjamin, M. King, M. Radakovitz, and C. Keplinger. Hydraulically amplified self-healing electrostatic actuators with muscle-like performance. *Science*, 359(6371):61–65, 2018.

[3] S. Ahmed, W. Wang, D. T. Gentekos, M. Hoyos, and T. E. Mallouk. Density and Shape Effects in the Acoustic Propulsion of Bimetallic Nanorod Motors. *ACS Nano*, 10:4763–4769, 2016.

[4] B. Ahn, K. Lee, R. Panchapakesan, and K. W. Oh. On-demand electrostatic droplet charging and sorting. *Biomicrofluidics*, 5(2):24113, 2011.

[5] J. A. Anderson, C. D. Lorenz, and A. Travesset. General purpose molecular dynamics simulations fully implemented on graphics processing units. *Journal of Computational Physics*, 227(10):5342–5359, 2008.

[6] J. J. Anderson. Colloid transport by interfacial forces. *Annu. Rev. Fluid Mech.*, 21:61–99, 1989.

[7] J. H. Bahng, B. Yeom, Y. Wang, S. O. Tung, J. D. Hoff, and N. Kotov. Anomalous dispersions of hedgehog' particles. *Nature*, 517(7536):596–599, 2014.

[8] F. Balboa Usabiaga, B. Delmotte, and A. Donev. Brownian dynamics of confined suspensions of active microrollers. *The Journal of Chemical Physics*, 146(13):134104, 2017.

[9] G. K. Batchelor. Transport Properties of Two-Phase Materials With Random Structure. *Annu. Rev. Fluid Mech.*, 6:227–255, 1974.

[10] J. R. Baylis, J. H. Yeon, M. H. Thomson, A. Kazerooni, X. Wang, A. E. S. John, E. B. Lim, D. Chien, A. Lee, J. Q. Zhang, J. M. Piret, L. S. Machan, T. F. Burke, N. J. White, and C. J. Kastrup. Self-propelled particles that transport cargo through flowing blood and halt hemorrhage. *Sci. Adv.*, 1(October):e1500379, 2015.

[11] H. T. Baytekin, A. Z. Patashinski, M. Branicki, B. Baytekin, S. Soh, and B. A. Grzybowski. The Mosaic of Surface Charge in Contact Electrification. *Science*, 333(6040):308–312, 2011.

[12] S. Birlasekaran. The measurement of charge on single particles in transformer oil. *IEEE Trans. Electr. Insul.*, 26(6):1094–1103, 1991.

[13] K. J. Bishop, A. M. Drews, C. A. Cartier, S. Pandey, and Y. Dou. Contact charge electrophoresis: Fundamentals and microfluidic applications. *Langmuir*, 34(22):6315–6327, 2018.

[14] K. J. M. Bishop, A. M. Drews, C. A. Cartier, S. Pandey, and Y. Dou. Contact charge electrophoresis: Fundamentals and microfluidic applications. *Langmuir*, 34(22):6315–6327, 2018.

[15] D. Blair and E. Dufresne. The matlab particle tracking code repository. `http://physics.georgetown.edu/matlab/`. Accessed: 2016-06-01.

[16] J. R. Blake and M. A. Sleigh. Mechanics of ciliary locomotion. *Biol. Rev.*, 49:85–125, 1974.

[17] R. T. Bonnecaze. Yield stresses in electrorheological fluids. *J. Rheol. (N. Y. N. Y).*, 36(1992):73, 1992.

[18] R. T. Bonnecaze and J. F. Brady. A method for determining the effective conductivity of dispersions of particles. *Proc. R. Soc. A*, 430:285–313, 1990.

[19] R. T. Bonnecaze and J. F. Brady. A method for determining the effective conductivity of dispersions of particles. *Proc. R. Soc. A*, 430:285–313, 1990.

[20] R. T. Bonnecaze and J. F. Brady. The effective conductivity of random suspensions of spherical particles. *Proc. R. Soc. A*, 432(1886):445–465, 1991.

[21] R. T. Bonnecaze and J. F. Brady. Dynamic simulation of an electrorheological fluid. *J. Chem. Phys.*, 96(3):2183–2202, 1992.

[22] A. Boymelgreen, G. Yossifon, S. Park, and T. Miloh. Spinning Janus doublets driven in uniform ac electric fields. *Physical Review E*, 89(1):011003, 2014.

[23] J. F. Brady and G. Bossis. Stokesian dynamics. *Annu. Rev. Fluid Mech.*, 20(1):111–157, 1988.

[24] J. F. Brady and G. Bossis. Stokesian dynamics. *Annual Review of Fluid Mechanics*, 20(1):111–157, 1988.

[25] H. Brenner. The slow motion of a sphere through a viscous fluid towards a plane surface. *Chem. Eng. Sci.*, 16(34):242–251, 1961.

[26] H. Brenner. The Stokes resistance of an arbitrary particle. 2. An extension. *Chem. Eng. Sci.*, 19(9):599–629, 1964.

[27] A. Bricard, J.-B. Caussin, N. Desreumaux, O. Dauchot, and D. Bartolo. Emergence of macroscopic directed motion in populations of motile colloids. *Nature*, 503(7474):95–98, nov 2013.

[28] A. Brown and W. Poon. Ionic effects in self-propelled Pt-coated Janus swimmers. *Soft Matter*, pages 4016–4027, 2014.

[29] J. D. Carlson and M. R. Jolly. MR fluid, foam and elastomer devices. *Mechatronics*, 10(4):555–569, 2000.

[30] C. Cartier, J. Graybill, and K. Bishop. Electric generation and ratcheted transport of contact-charged drops. *Phys. Rev. E*, 96:043101, 2017.

[31] C. A. Cartier, A. M. Drews, and K. J. Bishop. Microfluidic mixing of nonpolar liquids by contact charge electrophoresis. *Lab Chip*, 14(21):4230–4236, 2014.

[32] C. A. Cartier, A. M. Drews, and K. J. M. Bishop. Microfluidic Mixing of nonpolar liquids by contact charge electrophoresis. *Lab Chip*, 14(21):4230–4236, sep 2014.

[33] C. A. Cartier, A. M. Drews, and K. J. M. Bishop. Microfluidic mixing of nonpolar liquids by contact charge electrophoresis. *Lab Chip*, 14:4230–4236, 2014.

[34] C. A. Cartier, J. R. Graybill, and K. J. M. Bishop. Electric generation and ratcheted transport of contact-charged drops. *Phys. Rev. E*, 96:043101, Oct 2017.

[35] C. A. Cartier, J. R. Graybill, and K. J. M. Bishop. Electric generation and ratcheted transport of contact-charged drops. *Phys. Rev. E*, 96(4):043101, 2017.

[36] S. T. Chang, V. N. Paunov, D. N. Petsev, and O. D. Velev. Remotely powered self-propelling particles and micropumps based on miniature diodes. *Nat. Mater.*, 6(3):235–240, 2007.

[37] A. Y. H. Cho. Contact charging of micron-sized particles in intense electric fields. *J. Appl. Phys.*, 35(9):2561–2564, 1964.

[38] A. H. Cohen, G. B. Ermentrout, T. Kiemel, N. Kopell, K. A. Sigvardt, and T. L. Williams. Modelling of intersegmental coordination in the lamprey central pattern generator for locomotion. *Trends Neurosci.*, 15(11):434–438, 1992.

[39] A. H. Cohen, P. J. Holmes, and R. H. Rand. The Nature of the Coupling Between Segmental Oscillators of the Lamprey Spinal Generator for Locomotion: A Mathematical Model. *J. Math. Biol.*, 13:345–369, 1982.

[40] G. M. Colver. Dynamic and stationary charging of heavy metallic and dielectric particles against a conducting wall in the presence of a dc applied electric field. *J. Appl. Phys.*, 47(11):4839–4849, 1976.

[41] T. Darden, D. York, and L. Pedersen. Particle mesh Ewald: An N.log(N) method for Ewald sums in large systems. *J. Chem. Phys.*, 98:10089–10092, 1993.

[42] S. Das, A. Garg, A. I. Campbell, J. Howse, A. Sen, D. Velegol, R. Golestanian, and S. J. Ebbens. Boundaries can steer active Janus spheres. *Nat. Commun.*, 6:8999, 2015.

[43] S. K. Das, S. U. S. Choi, and H. E. Patel. Heat Transfer in NanofluidsA Review. *Heat Transf. Eng.*, 27(10):3–19, 2006.

[44] M. H. Davis. Two Charged Spherical Conductors in a Uniform Electric Field: Forces and Field Strength. *Q. J. Mech. Appl. Math.*, 17:499–511, 1964.

[45] M. H. Davis. Two Charged Spherical Conductors in a Uniform Electric Field: Forces and Field Strength. *Q. J. Mech. Appl. Math.*, 17:499–511, 1964.

[46] M. H. Davis. Electrostatic Field and Force on a Dielectric Sphere near a Conducting PlaneA Note on the Application of Electrostatic Theory to Water Droplets. *Am. J. Phys.*, 37(1):26, 1969.

[47] W. W. Dean and M. M. O'Neill. A slow motion of viscous liquid caused by the rotation of a solid sphere. *Mathematika*, 10(6):13–24, 1963.

[48] B. Delmotte, A. Donev, M. Driscoll, and P. Chaikin. Minimal model for a hydrodynamic fingering instability in microroller suspensions. *Phys. Rev. Fluids*, 2:114301, Nov 2017.

[49] K. K. Dey, F. Wong, A. Altemose, and A. Sen. Catalytic MotorsQuo Vadimus? *Curr. Opin. Colloid Interface Sci.*, 21:4–13, 2016.

[50] M. Dijkstra. Capillary Freezing or Complete Wetting of Hard Spheres in a Planar Hard Slit? *Physical Review Letters*, 93(10):108303, 2004.

[51] P. S. Dittrich and A. Manz. Lab-on-a-chip: microfluidics in drug discovery. *Nat. Rev. Drug Discov.*, 5(3):210–218, 2006.

[52] Y. Dou, C. Cartier, W. Fei, S. Pandey, S. Razavi, I. Kretzschmar, and K. Bishop. Directed motion of metallodielectric particles by contact charge electrophoresis. *Langmuir*, 32:13167–13173, 2016.

[53] A. M. Drews, C. A. Cartier, and K. J. Bishop. Contact charge electrophoresis: Experiment and theory. *Langmuir*, 31(13):3808–3814, 2015.

[54] A. M. Drews, C. A. Cartier, and K. J. M. Bishop. Contact Charge Electrophoresis: Experiment and Theory. *Langmuir*, 31:3808–3814, 2015.

[55] A. M. Drews, M. Kowalik, and K. J. Bishop. Charge and force on a conductive sphere between two parallel electrodes: A stokesian dynamics approach. *J. Appl. Phys.*, 116(7):074903, 2014.

[56] A. M. Drews, M. Kowalik, and K. J. M. Bishop. Charge and force on a conductive sphere between two parallel electrodes: a Stokesian dynamics approach. *J. Appl. Phys.*, 116:074903, 2014.

[57] A. M. Drews, H.-Y. Lee, and K. J. Bishop. Ratcheted electrophoresis for rapid particle transport. *Lab Chip*, 13(22):4295–4298, 2013.

[58] A. M. Drews, H.-Y. Lee, and K. J. M. Bishop. Ratcheted electrophoresis for rapid particle transport. *Lab Chip*, 13:4295–4298, 2013.

[59] A. M. Drews, H.-Y. Lee, and K. J. M. Bishop. Ratcheted electrophoresis for rapid particle transport. *Lab Chip*, 13:4295–4298, oct 2013.

[60] A. M. Drews, H.-Y. Lee, and K. J. M. Bishop. Ratcheted electrophoresis for rapid particle transport. *Lab Chip*, 13:4295–4298, 2013.

[61] R. Dreyfus, J. Baudry, M. L. Roper, M. Fermigier, H. A. Stone, and J. Bibette. Microscopic artificial swimmers. *Nature*, 437(7060):862–865, 2005.

[62] M. Driscoll, B. Delmotte, M. Youssef, S. Sacanna, A. Donev, and P. Chaikin. Unstable fronts and stable "critters" formed by microrollers. *Nat. Phys.*, 13(April):375–380, 2017.

[63] L. Durlofsky, J. F. Brady, and G. Bossis. Dynamic simulation of hydrodynamically interacting particles. *Journal of Fluid Mechanics*, 180:21–49, 1987.

[64] S. J. Ebbens. Active colloids: Progress and challenges towards realising autonomous applications. *Curr. Opin. Colloid Interface Sci.*, 21:14–23, 2015.

[65] J. Elgeti and G. Gompper. Emergence of metachronal waves in cilia arrays. *Proc. Natl. Acad. Sci. U.S.A.*, 110(12):4470–4475, 2013.

[66] E. Elton, E. Rosenberg, and W. Ristenpart. Crater Formation on Electrodes during Charge Transfer with Aqueous Droplets or Solid Particles. *Phys. Rev. Lett.*, 119(9):094502, 2017.

[67] E. S. Elton, Y. Tibrewala, E. R. Rosenberg, B. S. Hamlin, and W. D. Ristenpart. Measurement of Charge Transfer to Aqueous Droplets in High Voltage Electric Fields. *Langmuir*, page 10.1021/acs.langmuir.7b03375, 2017.

[68] J. S. Eow, M. Ghadiri, and A. Sharif. Experimental studies of deformation and break-up of aqueous drops in high electric fields. *Colloids Surf., A*, 225(1-3):193–210, 2003.

[69] D. Erickson, D. Sinton, and D. Li. A miniaturized high-voltage integrated power supply for portable microfluidic applications. *Lab Chip*, 4(2):87–90, 2004.

[70] F. Fahrenberger and C. Holm. Computing the coulomb interaction in inhomogeneous dielectric media via a local electrostatics lattice algorithm. *Phys. Rev. E*, 90:063304, Dec 2014.

[71] N. J. Felici. Forces and charges of small objects in contact with an electrode subjected to an electric field. *Revue Generale de l'electricite*, 75(10):1145–1160, 1966.

[72] S. Fournier-Bidoz, A. C. Arsenault, I. Manners, and G. A. Ozin. Synthetic self-propelled nanorotors. *Chemical Communications*, (4):441–443, 2005.

[73] B. Franklin. *Experiments And Observations On Electricity*. E. Cave, London, 1751.

[74] B. Franklin. Letter to P. Collinson. In L. Labaree, editor, *The Collected Papers of Benjamin Franklin*, chapter 5, page 69. Yale University, New Haven, 1962.

[75] B. Franklin and J. Bigelow. *The complete works of Benjamin Franklin; including his private as well as his official and scientific correspondence, and numerous letters and documents now for the first time printed, with many others not included in any former collection, also, the unmutilated and correct version of his autobiography.* G. P. Putnam's sons, New York and London, 1887. 10 v.

[76] M. M. Gacek and J. C. Berg. The role of acid-base effects on particle charging in apolar media. *Adv. Colloid Interface Sci.*, 220:108–123, 2015.

[77] Z. Gan, H. Wu, K. Barros, Z. Xu, and E. Luijten. Comparison of efficient techniques for the simulation of dielectric objects in electrolytes. *Journal of Computational Physics*, 291:317 – 333, 2015.

[78] S. Gangwal, O. J. Cayre, and O. D. Velev. Dielectrophoretic assembly of metallodielectric Janus particles in ac electric fields. *Langmuir*, 24(23):13312–13320, 2008.

[79] W. Gao, R. Dong, S. Thamphiwatana, J. Li, W. Gao, L. Zhang, and J. Wang. Artificial micromotors in the mouse's stomach: A step toward in vivo use of synthetic motors. *ACS Nano*, 9(1):117–123, 2015.

[80] C. D. Garcia, Y. Liu, P. Anderson, and C. S. Henry. Versatile 3-channel high-voltage power supply for microchip capillary electrophoresis. *Lab Chip*, 3(4):324–328, 2003.

[81] A. Garg, C. A. Cartier, K. J. Bishop, and D. Velegol. Particle Zeta Potentials Remain Finite in Saturated Salt Solutions. *Langmuir*, 32(45):11837–11844, 2016.

[82] L. Gervais, N. de Rooij, and E. Delamarche. Microfluidic chips for Point-of-Care immunodiagnostics. *Adv. Mater.*, 23(24):H151–H176, 2011.

[83] J. Glaser, T. D. Nguyen, J. A. Anderson, P. Lui, F. Spiga, J. A. Millan, D. C. Morse, and S. C. Glotzer. Strong scaling of general-purpose molecular dynamics simulations on {GPUs}. *Computer Physics Communications*, 192:97 – 107, 2015.

[84] A. Goldman, R. G. Cox, H. Brenner, and A. J. Goldmans. Slow viscous motion of a sphere parallel to a plane wallI Motion through a quiescent fluid. *Chem. Eng. Sci.*, 22:637–651, 1967.

[85] R. Golestanian, T. B. Liverpool, and A. Ajdari. Designing phoretic micro- and nano-swimmers. *New J. Phys.*, 9:126, 2007.

[86] C. P. Goodrich and M. P. Brenner. Using active colloids as machines to weave and braid on the micrometer scale. *tl. Acad. Sci. U.S.A.*, 114(2):257–262, 2017.

[87] L. Y. Gorelik, A. Isacsson, M. V. Voinova, B. Kasemo, R. I. Shekhter, and M. Jonson. Shuttle Mechanism for Charge Transfer in Coulomb Blockade Nanostructures. *Phys. Rev. Lett.*, 80(20):4526–4529, 1998.

[88] V. Gubala, L. F. Harris, A. J. Ricco, M. X. Tan, and D. E. Williams. Point of Care diagnostics: status and future. *Anal. Chem.*, 84(2):487–515, 2012.

[89] R. Hagedorn, G. Fuhr, T. Muller, and J. Gimsa. Traveling-wave dielectrophoresis of microparticles. *Electrophoresis*, 13(1-2):49–54, 1992.

[90] T. C. Halsey. Electrorheological Fluids. *Science*, 258(5083):761–766, 1992.

[91] B. S. Hamlin and W. D. Ristenpart. Transient reduction of the drag coefficient of charged droplets via the convective reversal of stagnant caps. *Phys. Fluids*, 24(1):012101, 2012.

[92] J. R. Happel and H. Brenner. *Low Reynolds Number Hydrodynamics*. M. Nijhoff, The Hague, 1983.

[93] C. K. Harnett, J. Templeton, K. a. Dunphy-Guzman, Y. M. Senousy, and M. P. Kanouff. Model based design of a microfluidic mixer driven by induced charge electroosmosis. *Lab Chip*, 8(4):565–572, 2008.

[94] M. Hase, S. N. Watanabe, and K. Yoshikawa. Rhythmic motion of a droplet under a dc electric field. *Phys. Rev. E*, 74(4):46301, 2006.

[95] Z. Hashin and S. Shtrikman. A Variational approach to the theory of the effective magnetic permeability of multiphase materials. *J. Appl. Phys.*, 33(10):3125–3131, 1962.

[96] F. J. Higuera, S. Succi, and R. Benzi. Lattice gas dynamics with enhanced collisions. *Europhysics Letters (EPL)*, 9(4):345–349, jun 1989.

[97] J. R. Howse, R. A. L. Jones, A. J. Ryan, T. Gough, R. Vafabakhsh, and R. Golestanian. Self-Motile Colloidal Particles: From Directed Propulsion to Random Walk. *Physical Review Letters*, 99(4):48102, 2007.

[98] M. Ibele, T. E. Mallouk, and A. Sen. Schooling behavior of light-powered autonomous micromotors in water. *Angew. Chem. Int. Ed.*, 48(18):3308–3312, jan 2009.

[99] A. J. Ijspeert. Central pattern generators for locomotion control in animals and robots: A review. *Neural Netw.*, 21:642–653, 2008.

[100] F. Ilievski, A. D. Mazzeo, R. F. Shepherd, X. Chen, and G. M. Whitesides. Soft robotics for chemists. *Angew. Chem. Int. Ed.*, 50(8):1890–1895, 2011.

[101] D. J. Im. Next generation digital microfluidic technology: Electrophoresis of charged droplets. *Korean J. Chem. Eng.*, 32(6):1001–1008, 2015.

[102] D. J. Im, M. M. Ahn, B. S. Yoo, D. Moon, D. W. Lee, and I. S. Kang. Discrete Electrostatic Charge Transfer by the Electrophoresis of a Charged Droplet in a Dielectric Liquid. *Langmuir*, 28(32):11656–11661, 2012.

[103] D. J. Im, J. Noh, D. Moon, and I. S. Kang. Electrophoresis of a charged droplet in a dielectric liquid for droplet actuation. *Anal. Chem.*, 83(13):5168–5174, 2011.

[104] D. J. Im, J. Noh, N. W. Yi, J. Park, and I. S. Kang. Influences of electric field on living cells in a charged water-in-oil droplet under electrophoretic actuation. *Biomicrofluidics*, 5(4):44112, 2011.

[105] D. J. Im, B. S. Yoo, M. M. Ahn, D. Moon, and I. S. Kang. Digital electrophoresis of charged droplets. *Anal. Chem.*, 85(8):4038–4044, 2013.

[106] Israelachvili. *Intermolecular and Surface Forces*. Academic Press, 2 edition, 1991.

[107] J. D. Jackson. *Classical Electrodynamics*. John Wiley, 1999. Third Edition.

[108] D. J. Jeffrey and M. Van Dyke. The Temperature Field or Electric Potential Around Two Almost Touching Spheres. *J. Inst. Math. its Appl.*, 22:337–351, 1978.

[109] G. B. Jeffrey and G. B. Jeffery. On the steady rotation of a solid of revolution in a viscous fluid. *Proc. London Math. Soc.*, 14:327–338, 1915.

[110] H. R. Jiang, N. Yoshinaga, and M. Sano. Active motion of a Janus particle by self-thermophoresis in a defocused laser beam. *Phys. Rev. Lett.*, 105(26):268302, 2010.

[111] Jie Zhang, Jing Yan, and Steve Granick. Directed Self-Assembly Pathways of Active Colloidal Clusters. *Angew. Chem. Int. Ed.*, 55:5166–5169, 2016.

[112] L. Jones and B. Makin. Measurement of charge transfer in a capacitive discharge. *IEEE Trans. Ind. Appl.*, 1A-16(1):76–79, 1980.

[113] Y. M. Jung and I. S. Kang. A novel actuation method of transporting droplets by using electrical charging of droplet in a dielectric fluid. *Biomicrofluidics*, 3(2):22402, 2009.

[114] Y.-M. Jung, H.-C. Oh, and I. S. Kang. Electrical charging of a conducting water droplet in a dielectric fluid on the electrode surface. *J. Colloid Interface Sci.*, 322(2):617–623, 2008.

[115] D. Kagan, P. Calvo-Marzal, S. Balasubramanian, S. Sattayasamitsathit, K. M. Manesh, G.-U. Flechsig, and J. Wang. Chemical sensing based on catalytic nanomotors: motion-based detection of trace silver. *J. Am. Chem. Soc.*, 131(34):12082–12083, 2009.

[116] P. Keblinski, R. Prasher, and J. Eapen. Thermal conductance of nanofluids: Is the controversy over? *J. Nanoparticle Res.*, 10(7):1089–1097, 2008.

[117] A. Khayari and A. Perez. Charge aquired by a spherical ball bouncing on an electrode: Comparison between theory and experiment. *IEEE Trans. Dielectr. Electr. Insul.*, 9(4):589–595, 2002.

[118] D. S. Kim, S. H. Lee, T. H. Kwon, and C. H. Ahn. A serpentine laminating micromixer combining splitting/recombination and advection. *Lab Chip*, 5(7):739–747, 2005.

[119] S. Kim and S. J. Karrila. *Microhydrodynamics*. Dover, Mineola, NY, 2005.

[120] C. Kittel. Introduction to solid state physics, 1995.

[121] A. Klckner, N. Pinto, Y. Lee, B. Catanzaro, P. Ivanov, and A. Fasih. Pycuda and pyopencl: A scripting-based approach to gpu run-time code generation. *Parallel Computing*, 38(3):157 – 174, 2012.

[122] C. R. Knutson, K. V. Edmond, M. T. Tuominen, and A. D. Dinsmore. Shuttling of charge by a metallic sphere in viscous oil. *J. Appl. Phys.*, 101(1):13706, 2007.

[123] A. B. Kolomeisky and M. E. Fisher. Molecular Motors: A Theorist's Perspective. *Annu. Rev. Phys. Chem.*, 58(1):675–695, 2007.

[124] M. Kopp and F. HÃ¶fling. Gpu-accelerated simulation of colloidal suspensions with direct hydrodynamic interactions. *The European Physical Journal Special Topics*, 210(1):101–117, 2012.

[125] M. Kowalik and K. J. M. Bishop. Ratcheted electrophoresis of Brownian particles. *Appl. Phys. Lett.*, 108(20):203103, 2016.

[126] R. V. Krotkov, M. T. Tuominen, and M. L. Breuer. Franklin's Bells and charge transport as an undergraduate lab. *Am. J. Phys.*, 69(1):50, 2001.

[127] S. K. Kumar, B. C. Benicewicz, R. A. Vaia, and K. I. Winey. 50th Anniversary Perspective: Are Polymer Nanocomposites Practical for Applications? *Macromolecules*, 50(3):714–731, 2017.

[128] L. D. Landau and E. Lifshitz. *Electrodynamics of Continuous Media*. Elsevier, New York, 1984.

[129] D. J. Laser and J. G. Santiago. A review of micropumps. *J. Micromech. Microeng.*, 14(6):R35–R64, 2004.

[130] E. Lauga and T. R. Powers. The hydrodynamics of swimming microorganisms. *Reports Prog. Phys.*, 72(9):096601, 2009.

[131] J. Lee, Z. L. Zhou, and S. H. Behrens. Charging Mechanism for Polymer Particles in Nonpolar Surfactant Solutions: Influence of Polymer Type and Surface Functionality. *Langmuir*, 32(19):4827–4836, 2016.

[132] J. Li, I. Rozen, and J. Wang. Rocket Science at the Nanoscale. *ACS Nano*, 10:5619–5634, 2016.

[133] J. Li, V. V. Singh, S. Sattayasamitsathit, J. Orozco, K. Kaufmann, R. Dong, W. Gao, B. Jurado-Sanchez, Y. Fedorak, and J. Wang. Water-driven micro-

motors for rapid photocatalytic degradation of biological and chemical warfare agents. *ACS Nano*, 8(11):11118–11125, nov 2014.

[134] D. R. Link, E. Grasland-Mongrain, A. Duri, F. Sarrazin, Z. Cheng, G. Cristobal, M. Marquez, and D. A. Weitz. Electric Control of Droplets in Microfluidic Devices. *Angew. Chem. Int. Ed.*, 45(16):2556–2560, 2006.

[135] A. C. Maggs and V. Rossetto. Local simulation algorithms for coulomb interactions. *Phys. Rev. Lett.*, 88:196402, Apr 2002.

[136] L. Malic, D. Brassard, T. Veres, and M. Tabrizian. Integration and detection of biochemical assays in digital microfluidic LOC devices. *Lab Chip*, 10(4):418–431, 2010.

[137] M. C. Marchetti, J.-f. Joanny, S. Ramaswamy, Liverpool, Prost, Rao, and Simha. Hydrodynamics of soft active matter. *Reivews of Modern Physics*, 85(September), 2013.

[138] E. Marder and D. Bucher. Central pattern generators and the control of rhythmic movements. *Curr. Biol.*, 11:R986–R996, 2001.

[139] F. Martinez-Pedrero and P. Tierno. Magnetic Propulsion of Self-Assembled Colloidal Carpets: Efficient Cargo Transport via a Conveyor-Belt Effect. *Phys. Rev. Appl.*, 3(5):051003, 2015.

[140] T. Masuda, A. M. Akimoto, K. Nagase, T. Okano, and R. Yoshida. Artificial cilia as autonomous nanoactuators: Design of a gradient self-oscillating polymer brush with controlled unidirectional motion. *Sci. Adv.*, 2(August):e1600902, 2016.

[141] J. Maxwell. A treatise on electricity and magnetism, 1873.

[142] E. Mersch and N. Vandewalle. Antiphase synchronization of electrically shaken conducting beads. *Phys Rev E*, 84(6), 2011.

[143] E. Mersch and N. Vandewalle. Antiphase synchronization of electrically shaken conducting beads. *Physical Review E*, 84(6):061301, 2011.

[144] T. Mochizuki, Y. H. Mori, and N. Kaji. Bouncing motions of liquid drops between tilted parallel-plate electrodes. *AIChE J.*, 36(7):1039–1045, 1990.

[145] E. Morales-Narváez, M. Guix, M. Medina-Sánchez, C. C. Mayorga-Martinez, and A. Merkoçi. Micromotor enhanced microarray technology for protein detection. *Small*, 10(13):2542–2548, 2014.

[146] J. L. Moran, P. M. Wheat, and J. D. Posner. Locomotion of electrocatalytic nanomotors due to reaction induced charge autoelectrophoresis. *Phys. Rev. E*, 81(6):065302, 2010.

[147] H. Morgan, N. G. Green, M. P. Hughes, W. Monaghan, and T. C. Tan. Large-area travelling-wave dielectrophoresis particle separator. *J. Micromech. Microeng.*, 7(2):65–70, 1997.

[148] F. Nadal and E. Lauga. Asymmetric steady streaming as a mechanism for acoustic propulsion of rigid bodies. *Phys. Fluids*, 26:082001, 2014.

[149] P. Neuži, S. Giselbrecht, K. Länge, T. J. Huang, and A. Manz. Revisiting lab-on-a-chip technology for drug discovery. *Nat. Rev. Drug Discov.*, 11(8):620–32, 2012.

[150] N.-T. Nguyen. *Micromixers: fundamentals, design, and fabrication.* Number 2011. William Andrew, 2nd ed. edition, 2012.

[151] T. Niedermayer, B. Eckhardt, and P. Lenz. Synchronization, phase locking, and metachronal wave formation in ciliary chains. *Chaos*, 18:037128, 2008.

[152] B. R. A. Nijboer and F. W. Dewette. The Internal Field in Dipole Lattices. *Physica*, 24(6):422–431, 1958.

[153] M. E. O'Neill. A slow motion of viscous liquid caused by a slowly moving solid sphere. *Mathematika*, 11(2):67–74, 1964.

[154] L. Ornstein and F. Zernike. Accidental deviations of density and opalescence at the critical point of a single substance. *Proc. Akad. Sci.(Amsterdam)*, XVII(September):793–806, 1914.

[155] J. M. Ottino and S. Wiggins. Introduction: mixing in microfluidics. *Phil. Trans. R. Soc. A*, 362(1818):923–935, 2004.

[156] B. Ottino-Loffler and S. Strogatz. Comparing the Locking Threshold for Rings and Chains of Oscillators. *Phys. Rev. E*, 94:062203, 2016.

[157] J. Palacci, S. Sacanna, A. P. Steinberg, D. J. Pine, and P. M. Chaikin. Living crystals of light-activated colloidal surfers. *Science*, 339(6122):936–940, mar 2013.

[158] S. Palagi, A. G. Mark, S. Y. Reigh, K. Melde, T. Qiu, H. Zeng, C. Parmeggiani, D. Martella, A. Sanchez-Castillo, N. Kapernaum, F. Giesselmann, D. S.

Wiersma, E. Lauga, and P. Fischer. Structured light enables biomimetic swimming and versatile locomotion of photoresponsive soft microrobots. *Nat. Mater.*, 15(6):647–653, 2016.

[159] H. Park, J. Park, A. K. L. Lim, E. H. Anderson, A. P. Alivisatos, and P. L. McEuen. Nanomechanical oscillations in a single C60 transistor. *Nature*, 407:57–60, 2000.

[160] S.-J. Park, M. Gazzola, K. S. Park, S. Park, V. D. Santo, E. L. Blevins, J. U. Lind, P. H. Campbell, S. Dauth, A. K. Capulli, F. S. Pasqualini, S. Ahn, A. Cho, H. Yuan, B. M. Maoz, R. Vijaykumar, J.-W. Choi, K. Deisseroth, G. V. Lauder, L. Mahadevan, and K. K. Parker. Phototactic guidance of a tissue-engineered soft-robotic ray. *Science*, 353(6295):158–162, 2016.

[161] M. Parthasarathy and D. J. Klingenberg. Electrorheology: Mechanisms and models. *Mater. Sci. Eng. R Reports*, 17(2):57–103, 1996.

[162] I. Pasichnyk and B. Dnweg. Coulomb interactions via local dynamics: a molecular-dynamics algorithm. *Journal of Physics: Condensed Matter*, 16(38):S3999–S4020, sep 2004.

[163] A. B. Pawar and I. Kretzschmar. Patchy particles by glancing angle deposition. *Langmuir*, 24(2):355–358, 2008.

[164] W. F. Paxton, K. C. Kistler, C. C. Olmeda, A. Sen, S. K. St Angelo, Y. Y. Cao, T. E. Mallouk, P. E. Lammert, and V. H. Crespi. Catalytic nanomotors: Autonomous movement of striped nanorods. *J. Am. Chem. Soc.*, 126(41):13424–13431, 2004.

[165] J. A. Pelesko. A self-organizing bucket brigade. In W. Badawy and W. Moussa, editors, *2004 International Conference on MEMS, NANO and Smart Systems*, pages 212–217, Los Alamitos, 2004. IEEE Computer Society.

[166] J. A. Pelesko. A self-organizing bucket brigade. In W. Badawy and W. Moussa, editors, *2004 Int. Conf. Mems, Nano Smart Syst. Proc.*, pages 212–217, Los Alamitos, 2004. IEEE.

[167] A. Perro, S. Reculusa, S. Ravaine, E. B. Bourgeat-Lami, and E. Duguet. Design and synthesis of Janus micro- and nanoparticles. *J. Mater. Chem.*, 15(35-36):3745–3760, 2005.

[168] P. Perry and G. J. Throop. Decay of pair correlations in hard sphere fluids. *The Journal of Chemical Physics*, 57(5):1827–1829, 1972.

[169] F. Potamian and J. Walsh. Franklin and Some Contemporaries. In *Makers of Electricty*, pages 68–132. Fordham University Press, New York, 1909.

[170] C. Pozrikidis. *A Practical Guide to Boundary Element Methods with the Software Library BEMLIB*. CRC Press, 2002.

[171] B. G. Prevo and O. D. Velev. Controlled, rapid deposition of structured coatings from micro-and nanoparticle suspensions. *Langmuir*, 20(6):2099–2107, 2004.

[172] D. C. Prieve, B. A. Yezer, A. S. Khair, P. J. Sides, and J. W. Schneider. Formation of Charge Carriers in Liquids. *Adv. Colloid Interface Sci.*, 244:21–35, 2017.

[173] E. M. Purcell. Life at Low Reynolds Number. *Am. J. Phys.*, 45(1):3–11, 1977.

[174] W. D. Ristenpart, J. C. Bird, A. Belmonte, F. Dollar, and H. A. Stone. Non-coalescence of oppositely charged drops. *Nature*, 461(7262):377–380, 2009.

[175] D. Rus and M. T. Tolley. Design, fabrication and control of soft robots. *Nature*, 521(7553):467–475, 2015.

[176] D. Rus and M. T. Tolley. Design, fabrication and control of soft robots. *Nature*, 521(7553):467–475, 2015.

[177] E. Schlauch, M. Ernst, R. Seto, H. Briesen, M. Sommerfeld, and M. Behr. Comparison of three simulation methods for colloidal aggregates in stokes flow: Finite elements, lattice boltzmann and stokesian dynamics. *Computers Fluids*, 86:199 – 209, 2013.

[178] M. Schmidt and H. Löwen. Phase diagram of hard spheres confined between two parallel plates. *Phys. Rev. E*, 55:7228–7241, Jun 1997.

[179] I. Sinn, P. Kinnunen, S. N. Pei, R. Clarke, B. H. McNaughton, and R. Kopelman. Magnetically uniform and tunable Janus particles. *Appl. Phys. Lett.*, 98(2):024101, 2011.

[180] G. S. Smith and R. Barakat. Electrostatics of two conducting spheres in contact. *Appl. Sci. Res.*, 30:418–432, 1975.

[181] W. Smith and D. Henderson. Analytical representation of the percus-yevick hard-sphere radial distribution function. *Molecular Physics*, 19(3):411–415, 1970.

[182] W. Smythe. *Static and Dynamic Electricity*. McGraw-Hill, New York, 1950.

[183] A. Snezhko and I. S. Aranson. Magnetic manipulation of self-assembled colloidal asters. *Nat. Mater.*, 10(9):698–703, 2011.

[184] J.-H. So and M. D. Dickey. Inherently aligned microfluidic electrodes composed of liquid metal. *Lab Chip*, 11(5):905–911, 2011.

[185] L. Soler, V. Magdanz, V. M. Fomin, S. Sanchez, and O. G. Schmidt. Self-propelled micromotors for cleaning polluted water. *ACS Nano*, 7(11):9611–9620, 2013.

[186] M. Spellings, M. Engel, D. Klotsa, S. Sabrina, A. M. Drews, N. H. P. Nguyen, K. J. M. Bishop, and S. C. Glotzer. Shape control and compartmentalization in active colloidal cells. *Proc. Natl. Acad. Sci. U.S.A.*, 112(34):E4642–50, 2015.

[187] B. Sprinkle, F. Balboa Usabiaga, N. A. Patankar, and A. Donev. Large scale brownian dynamics of confined suspensions of rigid particles. *The Journal of Chemical Physics*, 147(24):244103, 2017.

[188] B. Sprinkle, A. Donev, A. P. Singh Bhalla, and N. Patankar. Brownian Dynamics of Fully Confined Suspensions of Rigid Particles Without Green's Functions. *arXiv e-prints*, page arXiv:1901.06427, Jan 2019.

[189] T. M. Squires and M. Z. Bazant. Breaking symmetries in induced-charge electro-osmosis and electrophoresis. *J. Fluid Mech.*, 560:65–101, 2006.

[190] G. Stokes. On the effect of the internal friction of fluids on the motion of pendulums. *Trans. Cambridge Philos. Soc.*, 9:8, 1851.

[191] J. W. Swan and J. F. Brady. Simulation of hydrodynamically interacting particles near a no-slip boundary. *Phys. Fluids*, 19(11):113306, 2007.

[192] J. W. Swan and J. F. Brady. Simulation of hydrodynamically interacting particles near a no-slip boundary. *Phys. Fluids*, 19(11):113306, 2007.

[193] J. W. Swan and J. F. Brady. Particle motion between parallel walls: hydrodynamics and simulation. *Phys. Fluids*, 22(10):103301, 2010.

[194] J. W. Swan and J. F. Brady. The hydrodynamics of confined dispersions. *J. Fluid Mech.*, 687:254–299, Oct. 2011.

[195] D. Takagi, J. Palacci, A. B. Braunschweig, M. J. Shelley, and J. Zhang. Hydrodynamic capture of microswimmers into sphere-bound orbits. *Soft Matter*, 10:1784–1789, 2014.

[196] H. Takele, H. Greve, C. Pochstein, V. Zaporojtchenko, and F. Faupel. Plasmonic properties of ag nanoclusters in various polymer matrices. *Nanotechnology*, 17(14):3499, 2006.

[197] Y. Tanaka. A peristaltic pump integrated on a 100% glass microchip using computer controlled piezoelectric actuators. *Micromachines*, 5(2):289–299, 2014.

[198] G. Taylor. Analysis of the Swimming of Microscopic Organisms. *Proc. Royal Soc. A*, 209(1099):447–461, 1951.

[199] R. Taylor, S. Coulombe, T. Otanicar, P. Phelan, A. Gunawan, W. Lv, G. Rosengarten, R. Prasher, and H. Tyagi. Small particles, big impacts: A review of the diverse applications of nanofluids. *J. Appl. Phys.*, 113(1), 2013.

[200] R. Tobazeon. Electrohydrodynamic behaviour of single spherical or cylindrical conducting particles in an insulating liquid subjected to a uniform DC field. *J. Phys. D: Appl. Phys.*, 29(10):2595–2608, 1996.

[201] L. S. Tsimring, N. F. Rulkov, M. L. Larsen, and M. Gabbay. Repulsive synchronization in an array of phase oscillators. *Phys. Rev. Lett.*, 95(1):014101, 2005.

[202] M. T. Tuominen, R. V. Krotkov, and M. L. Breuer. Stepwise and hysteretic transport behavior of an electromechanical charge shuttle. *Phys. Rev. Lett.*, 83(15):3025–3028, 1999.

[203] T. Um, J. Hong, D. J. Im, S. J. Lee, and I. S. Kang. Electrically Controllable Microparticle Synthesis and Digital Microfluidic Manipulation by Electric-Field-Induced Droplet Dispensing into Immiscible Fluids. *Sci. Rep.*, 6:31901, 2016.

[204] J. Van Beek and R. Puers. A review of mems oscillators for frequency reference and timing applications. *J. Micromechanics Microengineering*, 22(1):013001, 2011.

[205] H. Varmus, R. Klausner, E. Zerhouni, T. Acharya, A. S. Daar, and P. A. Singer. Grand challenges in global health. *Science*, 302(5644):398–399, 2003.

[206] P. Walsh. *Makers of Electricity.* Fordham University Press, 1909.

[207] C. M. Wang, L. Wang, X. R. Zhu, Y. G. Wang, and J. M. Xue. Low-voltage electroosmotic pumps fabricated from track-etched polymer membranes. *Lab Chip*, 12(9):1710–1716, 2012.

[208] W. Wang, T. Y. Chiang, D. Velegol, and T. E. Mallouk. Understanding the efficiency of autonomous nano- and microscale motors. *J. Am. Chem. Soc.*, 135(28):10557–10565, 2013.

[209] W. Wang, W. Duan, S. Ahmed, A. Sen, and T. E. Mallouk. From one to many: Dynamic assembly and collective behavior of self-propelled colloidal motors. *Acc. Chem. Res.*, 48(7):1938–1946, 2015.

[210] Y. Wang, R. M. Hernandex, D. J. Bartlett, J. M. Bingham, T. R. Kline, A. Sen, and T. E. Mallouk. Bipolar electrochemical mechanism for the propulsion of catalytic nanomotors in hydrogen peroxide solutions. *Langmuir*, 22:10451–10456, 2006.

[211] H. Wei and H. Eilers. Electrical conductivity of thin-film composites containing silver nanoparticles embedded in a dielectric fluoropolymer matrix. *Thin Solid Films*, 517(2):575 – 581, 2008.

[212] H. Wu and E. Luijten. Accurate and efficient numerical simulation of dielectrically anisotropic particles. *The Journal of Chemical Physics*, 149(13):134105, 2018.

[213] Y. N. Xia and G. M. Whitesides. Soft lithography. *Annu. Rev. Mater. Sci.*, 28:153–184, 1998.

[214] J. Yan, M. Bloom, S. C. Bae, E. Luijten, and S. Granick. Linking synchronization to self-assembly using magnetic Janus colloids. *Nature*, 491(7425):578–581, 2012.

[215] J. Yan, M. Han, J. Zhang, C. Xu, E. Luijten, and S. Granick. Reconfiguring active particles by electrostaticâ?imbalance. *Nature Materials*, 15:1095 EP, Jul 2016.

[216] S. H. Yang and D. J. Im. Electrostatic Origins of the Positive and Negative Charging Difference in the Contact Charge Electrophoresis of a Water Droplet. *Langmuir*, 33:13740–13748, 2017.

[217] V. V. Yashin, O. Kuksenok, P. Dayal, and A. C. Balazs. Mechano-chemical oscillations and waves in reactive gels. *Rep. Prog. Phys.*, 75(6):066601, 2012.

[218] W. M. Zhang, H. Yan, Z. K. Peng, and G. Meng. Electrostatic pull-in instability in MEMS/NEMS: A review. *Sensors Actuators, A Phys.*, 214:187–218, 2014.

Part I

Appendices

Appendix A

A.1 Electrostatics of Particle Dispersions

A.1.1 Grand Potential Tensor

Consider a collection of N conductive particles dispersed in an unbounded dielectric medium and subject to an external potential $\phi^{\infty}(\boldsymbol{x})$. The electric potential $\phi(\boldsymbol{x})$ in the dielectric is governed by the Laplace equation

$$\nabla^2\phi = 0. \tag{A.1}$$

Far from the particles, the potential approaches the external potential present in the particles' absence; at the surface $\mathcal{S}_\beta$ of particle β, the potential is equal to the particle potential Φ_β

$$\phi(\boldsymbol{x}) = \phi^{\infty}(\boldsymbol{x}) \quad \text{for } |\boldsymbol{x}| \to \infty, \tag{A.2}$$

$$\phi(\boldsymbol{x}) = \Phi_\beta \quad \text{for } \boldsymbol{x} \in \mathcal{S}_\beta. \tag{A.3}$$

In general, the disturbance potential can be expressed by a series of integrals over the particle surfaces as

$$\phi(\boldsymbol{x}) - \phi^{\infty}(\boldsymbol{x}) = \sum_{\beta=1}^{N} \int_{\mathcal{S}_\beta} [-G(\boldsymbol{x},\boldsymbol{y})\nabla\phi(\boldsymbol{y}) + \phi(\boldsymbol{y})\nabla_{\boldsymbol{y}} G(\boldsymbol{x},\boldsymbol{y})] \cdot \boldsymbol{n}(\boldsymbol{y}) d\mathcal{S}_\beta(\boldsymbol{y}), \tag{A.4}$$

where $\boldsymbol{n}$ is the unit vector directed out from the particles, and $G(\boldsymbol{x}, \boldsymbol{y})$ is the Green's function for the potential at point $\boldsymbol{x}$ due to a point charge at point $\boldsymbol{y}$.Bonnecaze1990,Pozrikidis2002 For an unbounded medium, the Green's function is simply

$$G(\boldsymbol{x}, \boldsymbol{y}) = \frac{1}{4\pi\varepsilon r}, \tag{A.5}$$

with $r = |\boldsymbol{x} - \boldsymbol{y}|$.

Expanding the Green's function in a Taylor series in $\boldsymbol{y}$ about the center of each particle $\boldsymbol{x}_\beta$, we can write equation (A.4) in terms of the charge moments

$$\phi(\boldsymbol{x}) - \phi^\infty(\boldsymbol{x}) = \sum_{\beta=1}^{N} \left[q_\beta G(\boldsymbol{x}, \boldsymbol{x}_\beta) + \boldsymbol{p}_\beta \cdot \nabla_{\boldsymbol{y}} G(\boldsymbol{x}, \boldsymbol{y})|_{\boldsymbol{y}=\boldsymbol{x}_\beta} + \dots \right] \tag{A.6}$$

where q_β and $\boldsymbol{p}_\beta$ are the charge and dipole of particle β

$$q_\beta = \int_{\mathcal{S}_\beta} -\nabla\phi(\boldsymbol{y}) \cdot \boldsymbol{n}(\boldsymbol{y}) d\mathcal{S}(\boldsymbol{y}), \tag{A.7}$$

$$\boldsymbol{p}_\beta = \int_{\mathcal{S}_\beta} \left[-(\boldsymbol{y} - \boldsymbol{x}_\beta)\nabla\phi(\boldsymbol{y}) + \boldsymbol{\delta}\phi(\boldsymbol{y}) \right] d\mathcal{S}(\boldsymbol{y}). \tag{A.8}$$

Higher order charge moments can be obtained in a similar fashion.

When $\boldsymbol{x}$ is located on a Integrating equation (A.9) for the potential $\phi'(\boldsymbol{x})$ over the surface of particle α, we obtain

$$\phi'(\boldsymbol{x}) = \sum_{\beta=1}^{N} \left[q_\beta G(\boldsymbol{x}, \boldsymbol{x}_\beta) + \boldsymbol{p}_\beta \cdot \nabla_{\boldsymbol{y}} G(\boldsymbol{x}, \boldsymbol{y})|_{\boldsymbol{y}=\boldsymbol{x}_\beta} + \dots \right] \tag{A.9}$$

Equation (A.4) also implies that the integrals over the particles surface containing the external potential are also zero. To see this,

The expression for the dipole moment assumes that the particles are conductive; the more general case was described previously by Bonnecaze and Brady.Bonnecaze1990

Additionally, Porzikidis equation (4.2.11) can be used to show that the double layer potential is zero for conductive particles.

For conductive particles, the potential at the surface of particle β is constant and equal to the particle potential; as a result, the second term of equation (A.4) (the so-called double-layer potential) is identically zero.

Derivation. Integrating equation (A.9) for the potential $\phi'(\boldsymbol{x})$ over the surface of particle α, we obtain

$$\int_{\mathcal{S}_\alpha} \phi'(\boldsymbol{x}) d\mathcal{S}(\boldsymbol{x}) = \int_{\mathcal{S}_\alpha} \sum_{\beta=1}^{N} \left[q_\beta G(\boldsymbol{x}, \boldsymbol{x}_\beta) + \boldsymbol{p}_\beta \cdot \nabla_{\boldsymbol{y}} G(\boldsymbol{x}, \boldsymbol{y})|_{\boldsymbol{y}=\boldsymbol{x}_\beta} + \dots \right] d\mathcal{S}(\boldsymbol{x}) \quad \text{(A.10)}$$

A.1.2 Two-Body Capacitance Tensor, $\mathcal{C}^{2B}$

We consider two conductive spheres of equal radius a located at positions $\boldsymbol{x}_\alpha$ and $\boldsymbol{x}_\beta$ within an unbounded dielectric medium of permittivity ε. The two spheres are subject to an external potential

$$\phi^\infty(\boldsymbol{x}) = -\boldsymbol{x}\cdot\boldsymbol{E}^\infty \tag{A.11}$$

The charges q_α and q_β and dipole moments $\boldsymbol{p}_\alpha$ and $\boldsymbol{p}_\varphi$ on the two spheres are related to the sphere potentials Φ_α and Φ_β and to the external field $\boldsymbol{E}^\infty$ by the linear relation

$$\begin{bmatrix} q_\alpha \\ q_\beta \\ \boldsymbol{p}_\alpha \\ \boldsymbol{p}_\beta \end{bmatrix} = \begin{bmatrix} A_{\alpha\alpha} & A_{\alpha\beta} & \widetilde{\boldsymbol{B}}_{\alpha\alpha} & \widetilde{\boldsymbol{B}}_{\alpha\beta} \\ A_{\beta\alpha} & A_{\beta\beta} & \widetilde{\boldsymbol{B}}_{\beta\alpha} & \widetilde{\boldsymbol{B}}_{\beta\beta} \\ \boldsymbol{B}_{\alpha\alpha} & \boldsymbol{B}_{\alpha\beta} & \boldsymbol{C}_{\alpha\alpha} & \boldsymbol{C}_{\alpha\beta} \\ \boldsymbol{B}_{\beta\alpha} & \boldsymbol{B}_{\beta\beta} & \boldsymbol{C}_{\beta\alpha} & \boldsymbol{C}_{\beta\beta} \end{bmatrix} \cdot \begin{bmatrix} \Phi_\alpha - \phi(\boldsymbol{x}_\alpha) \\ \Phi_\beta - \phi(\boldsymbol{x}_\beta) \\ \boldsymbol{E}^\infty \\ \boldsymbol{E}^\infty \end{bmatrix} \tag{A.12}$$

where the capacitance coefficients depend only on the displacement vector $\boldsymbol{r} = \boldsymbol{x}_\beta - \boldsymbol{x}_\alpha$. The two-body capacitance tensor $\mathcal{C}^{2B}$ is symmetric and positive definite; this tensor is also invariant to rotation about the axis connecting the two spheres and to permutation of the two (identical) spheres. Accounting for these symmetries, the capacitance coefficients can be expressed as

$$A_{\alpha\alpha} = A_{\beta\beta} = X^A_{\alpha\alpha} \tag{A.13}$$

$$A_{\alpha\beta} = A_{\beta\alpha} = X^A_{\alpha\beta} \tag{A.14}$$

$$\boldsymbol{B}_{\alpha\alpha} = \widetilde{\boldsymbol{B}}_{\alpha\alpha} = -\boldsymbol{B}_{\beta\beta} = -\widetilde{\boldsymbol{B}}_{\beta\beta} = X^B_{\alpha\alpha}\hat{\boldsymbol{r}} \tag{A.15}$$

$$-\boldsymbol{B}_{\alpha\beta} = \widetilde{\boldsymbol{B}}_{\alpha\beta} = \boldsymbol{B}_{\beta\alpha} = -\widetilde{\boldsymbol{B}}_{\beta\alpha} = X^B_{\alpha\beta}\hat{\boldsymbol{r}} \tag{A.16}$$

$$\boldsymbol{C}_{\alpha\alpha} = \boldsymbol{C}_{\beta\beta} = X^C_{\alpha\alpha}\hat{\boldsymbol{r}}\hat{\boldsymbol{r}} + Y^C_{\alpha\alpha}(\boldsymbol{\delta} - \hat{\boldsymbol{r}}\hat{\boldsymbol{r}}) \tag{A.17}$$

$$\boldsymbol{C}_{\alpha\beta} = \boldsymbol{C}_{\beta\alpha} = X^C_{\alpha\beta}\hat{\boldsymbol{r}}\hat{\boldsymbol{r}} + Y^C_{\alpha\beta}(\boldsymbol{\delta} - \hat{\boldsymbol{r}}\hat{\boldsymbol{r}}) \tag{A.18}$$

where $\boldsymbol{\delta}$ is the identity tensor, $\hat{\boldsymbol{r}} = \boldsymbol{r}/r$ is the unit vector directed from sphere α to sphere β, and the scalar quantities $X^A_{\alpha\alpha}$, $X^A_{\alpha\beta}$, $X^B_{\alpha\alpha}$, *etc.* are functions of the sphere separation r.

Here and throughout, it will be convenient make use of dimensionless quantities where lengths are scaled by the particle radius a, electric fields by E^∞, electric potentials by aE^∞, charges by $4\pi\varepsilon a^2 E^\infty$, and dipoles by $4\pi\varepsilon a^3 E^\infty$. Using the analytical solution of DavisDavis1964b, the scalar functions can be expressed as

$$X^A_{\alpha\alpha} = 2bS_0(\mu) \tag{A.19}$$

$$X^A_{\alpha\beta} = 2bS_0(0) \tag{A.20}$$

$$X^B_{\alpha\alpha} = 2b^2\left[-S_1(\mu) + \frac{r}{2b}S_0(\mu)\right] \tag{A.21}$$

$$X^B_{\alpha\beta} = 2b^2\left[-S_1(0) + \frac{r}{2b}S_0(0)\right] \tag{A.22}$$

$$X^C_{\alpha\alpha} = 2b^3\left[S_2(\mu) - \frac{r}{b}S_1(\mu) + \frac{r^2}{4b^2}S_0(\mu)\right] \tag{A.23}$$

$$X^C_{\alpha\beta} = 2b^3\left[S_2(0) - \frac{r}{b}S_1(0) + \frac{r^2}{4b^2}S_0(0)\right] \tag{A.24}$$

$$Y^C_{\alpha\alpha} = 8b^3 S_0'(\mu) \tag{A.25}$$

$$Y^C_{\alpha\beta} = 8b^3 S_0'(0) \tag{A.26}$$

Here, b and μ are geometric quantities defined as

$$b = \frac{1}{2}\sqrt{r^2 - 4} \quad \text{and} \quad \mu = \ln\left(r + \sqrt{r^2 - 4}\right) \tag{A.27}$$

The function $S_m(\xi)$ is given by the infinite sum

$$S_m(\xi) = \sum_{n=0}^{\infty} \frac{(2n+1)^m e^{(2n+1)\xi}}{e^{(4n+2)\mu} - 1} \tag{A.28}$$

The sum $S_m'(\xi)$ is that given in equation (A.28) but with the first term omitted.

Far Field Approximation, $\mathcal{C}^{2B,\infty}$

In using the pairwise capacitance functions outlined above, we must subtract the far field contribution $\mathcal{C}^{2B,\infty}$ which is already included (correctly) within the many body induction tensor $\mathcal{P}$. This correction is obtained by truncating the induction tensor for the two-sphere at the dipole level and then inverting to obtain $\mathcal{C}^{2B,\infty}$. The components of this truncated induction tensor relate the sphere charges and dipoles to the potentials and field as

$$\begin{bmatrix} a_{\alpha\alpha} & a_{\alpha\beta} & \widetilde{\boldsymbol{b}}_{\alpha\alpha} & \widetilde{\boldsymbol{b}}_{\alpha\beta} & \cdots \\ a_{\beta\alpha} & a_{\beta\beta} & \widetilde{\boldsymbol{b}}_{\beta\alpha} & \widetilde{\boldsymbol{b}}_{\beta\beta} & \\ \boldsymbol{b}_{\alpha\alpha} & \boldsymbol{b}_{\alpha\beta} & \boldsymbol{c}_{\alpha\alpha} & \boldsymbol{c}_{\alpha\beta} & \\ \boldsymbol{b}_{\beta\alpha} & \boldsymbol{b}_{\beta\beta} & \boldsymbol{c}_{\beta\alpha} & \boldsymbol{c}_{\beta\beta} & \cdots \\ \vdots & & & \vdots & \end{bmatrix} \cdot \begin{bmatrix} q_\alpha \\ q_\beta \\ \boldsymbol{p}_\alpha \\ \boldsymbol{p}_\beta \\ \vdots \end{bmatrix} = \begin{bmatrix} \Phi_\alpha - \phi(\boldsymbol{x}_\alpha) \\ \Phi_\beta - \phi(\boldsymbol{x}_\beta) \\ \boldsymbol{E}^\infty \\ \boldsymbol{E}^\infty \\ \vdots \end{bmatrix} \tag{A.29}$$

These induction coefficients share the same symmetries as the capacitance coefficients and can be expressed in a form analogous to that of equations (A.13) to (A.18). The associated scalar functions are given by

$$X^a_{\alpha\alpha} = 1 \tag{A.30}$$

$$X^a_{\alpha\beta} = r^{-1} \tag{A.31}$$

$$X^b_{\alpha\alpha} = 0 \tag{A.32}$$

$$X^b_{\alpha\beta} = -r^{-2} \tag{A.33}$$

$$X^c_{\alpha\alpha} = 1 \tag{A.34}$$

$$X^c_{\alpha\beta} = -2r^{-3} \tag{A.35}$$

$$Y^c_{\alpha\alpha} = 1 \tag{A.36}$$

$$Y^c_{\alpha\beta} = r^{-3} \tag{A.37}$$

It is possible to invert the truncated induction tensor analytically to obtain the far-field approximation to the two-sphere capacitance functions

$$X_{\alpha\alpha}^{A,\infty} = \frac{-4r^2 - r^4 + r^8}{1 - 4r^2 - 2r^4 - r^6 + r^8} \tag{A.38}$$

$$X_{\alpha\beta}^{A,\infty} = \frac{2r - r^7}{1 - 4r^2 - 2r^4 - r^6 + r^8} \tag{A.39}$$

$$X_{\alpha\alpha}^{B,\infty} = \frac{2r^3 + r^5}{1 - 4r^2 - 2r^4 - r^6 + r^8} \tag{A.40}$$

$$X_{\alpha\beta}^{B,\infty} = \frac{r^2 + r^6}{1 - 4r^2 - 2r^4 - r^6 + r^8} \tag{A.41}$$

$$X_{\alpha\alpha}^{C,\infty} = \frac{-r^4 - r^6 + r^8}{1 - 4r^2 - 2r^4 - r^6 + r^8} \tag{A.42}$$

$$X_{\alpha\beta}^{C,\infty} = \frac{-r^3 + 2r^5}{1 - 4r^2 - 2r^4 - r^6 + r^8} \tag{A.43}$$

$$Y_{\alpha\alpha}^{C,\infty} = \frac{-r^6}{1 - r^6} \tag{A.44}$$

$$Y_{\alpha\beta}^{C,\infty} = \frac{r^3}{1 - r^6} \tag{A.45}$$

Sphere-Wall Interactions

The near-field interaction between a sphere α and an a planar wall of constant potential at can be computed from the two-sphere results summarized above by considering an image sphere of charge q_β and dipole $\boldsymbol{p}_\beta$ located at position $\boldsymbol{x}_\beta$. We assume that the wall is oriented normal to the $\boldsymbol{e}_3$ direction at a height x_3^w above the origin. The resulting charge, dipole, and position of the image sphere are given by

$$q_\beta = -q_\alpha \tag{A.46}$$

$$\boldsymbol{p}_\beta = -\boldsymbol{p}_\beta + 2(\boldsymbol{p}_\beta \cdot \boldsymbol{e}_3)\boldsymbol{e}_3 \tag{A.47}$$

$$\boldsymbol{x}_\beta = \boldsymbol{x}_\alpha - 2(\boldsymbol{x}_\alpha \cdot \boldsymbol{e}_3 - x_3^w)\boldsymbol{e}_3 \tag{A.48}$$

A.1.3 Electric Current

The electric current I is defined as the time rate of change of the excess charge q_u on the upper electrode ($x_3 = L_3$) due to the motion of the charged polarizable particles

$$I = \frac{\mathrm{d}q_u}{\mathrm{d}t} \tag{A.49}$$

The excess charge q_u is related to the particle charges and dipoles as

$$q_u = -\frac{1}{L_3} \sum_{\beta=1}^{N} \left(x_3^\beta q_\beta + p_3^\beta \right) \tag{A.50}$$

This result can be derived using Green's second identity

$$\int_{\mathcal{V}} \left(\phi \nabla^2 u - u \nabla^2 \phi \right) \mathrm{d}\mathcal{V} = \int_{\mathcal{S}} \boldsymbol{n} \cdot \left(\phi \nabla u - u \nabla \phi \right) \mathrm{d}\mathcal{S} \tag{A.51}$$

where the control volume $\mathcal{V}$ contains the entire interelectrode region, and $\boldsymbol{n}$ is the unit normal vector pointing out from this volume. The two functions are the electric potential $\phi(\boldsymbol{x})$ and $u(\boldsymbol{x}) = -x_3$. Substituting these functions and making use of the Poisson equation, $\nabla^2 \phi = -\rho_e / \varepsilon$, we obtain

$$\int_{\mathcal{V}} x_3 \rho_e(\boldsymbol{x}) \mathrm{d}\mathcal{V} = \varepsilon \int_{\mathcal{S}} \boldsymbol{n} \cdot \left(\phi \boldsymbol{e}_3 - x_3 \nabla \phi \right) \mathrm{d}\mathcal{S} \tag{A.52}$$

The left-hand-side is the total dipole moment in the 3-direction within the interelectrode region. The right-hand-side must be evaluated over the lower and upper electrodes ($x_3 = 0$ and $x_3 = L_3$, respectively). Assuming the electrodes potentials are $\phi_l = 0$ and $\phi_u = -L_3 E^\infty$, the above relation can be written as

$$\int_{\mathcal{V}} x_3 \rho_e(\boldsymbol{x}) \mathrm{d}\mathcal{V} = -L_3 \int_{\mathcal{S}_u} \varepsilon \boldsymbol{e}_3 \cdot \left(\nabla \phi + \boldsymbol{E}^\infty \right) \mathrm{d}\mathcal{S} \tag{A.53}$$

The integral on the right-hand-side corresponds to the excess charge q_u on the upper electrode due to the charge distribution $\rho_e(\boldsymbol{x})$ between the electrodes. The total dipole

moment on the left-hand-side can be written as a sum over the particle charges and dipoles to obtain the desired result (A.50).

Equation (A.49) for the electric current is appropriate during the intervals between charge-transfer "collisions" among the particles. Such collisions make additional contributions to the current, which are modeled as instantaneous pulses of magnitude

$$\Delta q_u = q'_u - q_u \tag{A.54}$$

where q'_u is the new charge on the electrode after the collision. Additionally, when a particle α makes contact with the upper electrode and its charge changes from q_α to q'_α, that difference is transferred directly to the upper electrode and does not contribute to the flow of current through the external circuit. The overall current can therefore be written as

$$I(t) = \frac{\mathrm{d}q_u}{\mathrm{d}t} + \Delta q_u(t_k)\delta(t - t_k) - (q'_\alpha - q_\alpha)\delta(t - t^*_k) \tag{A.55}$$

where t_k refers to the time of the k^{th} collision of any kind. Those collisions between a particle α and the upper electrode (at time t^*_k) involve an additional correction to avoid double counting the direct charge transfer event.

Appendix B

B.1 Validation via Madelung Constants

To validate the method introduced in Chapter 3, we examine four classic problems: (1) the first order Madelung constant for NaCl crystal with alternating positive and negative point charges on lattice points, (2) second order Madelung constant for the simple cubic lattice of point dipoles on lattice points (3) the conductivity of simple cubic periodic lattice, and (4) the conductivity of random particle dispersions. Each of these problems has been considered previously for three-dimensionally periodic ("bulk") systems.

Here, we reproduce these known results in the limit as $L_3 \to \infty$ and compare with results from the case of confining boundaries that is finite L_3 as well as discuss the effects of the confining boundaries for smaller separations. Since all the classic problems from (1)-(3) involve simple cubic lattice, the method of image charges allows us to create a pseudo three dimensional periodic lattice by maintaining a distance of half the lattice constant ($c/2$) between the particles close to the wall and the wall. Thus comparing the three dimensionally periodic lattice with the above described confined two dimensionally periodic lattice must yield the same results for the problems (1)-(3).

B.1.1 First order Madelung constant

We apply the above method to compute the first order Madelung constant of NaCl crystal with ions approximated by point charges placed at lattice points sandwiched between two grounded electrodes.

- Charge density of ions is approximated by point charge.
- Simulation cell must be charge neutral.

The value of first order Madelung constant for a neutral ionic NaCl lattice is represented as,

$$\mathbf{M_{NaCl}} = \sum_{b} \frac{z_{ab}}{r_{ab}/r_0} = \langle \mathbf{\Phi_p} \rangle \cdot \mathbf{r_0}, \tag{B.1}$$

where $\mathbf{r_o}$ represents the nearest neighbour distance, value of Madelung constant for NaCl lattice is evaluated from (B.1) and compared against the exact value mentioned in Kittel[120]($\approx 1.74756\ldots$). Results from the literature agree very well with our simulation results which validates charge and potential relation accounted by our approach for periodic and confined systems.

B.1.2 Second order Madelung constant

The problem of calculating field for a lattice of point dipoles on a cubic lattice was first studied by Ornstein and Zernike[154] and relates closely to the calculation of internal field from Lorentz' classical theory of dielectric constant.

$$\acute{S} = p \sum_{\lambda} 2\mathbf{P_2}(\cos\theta_\lambda)/{r_\lambda}^3, \tag{B.2}$$

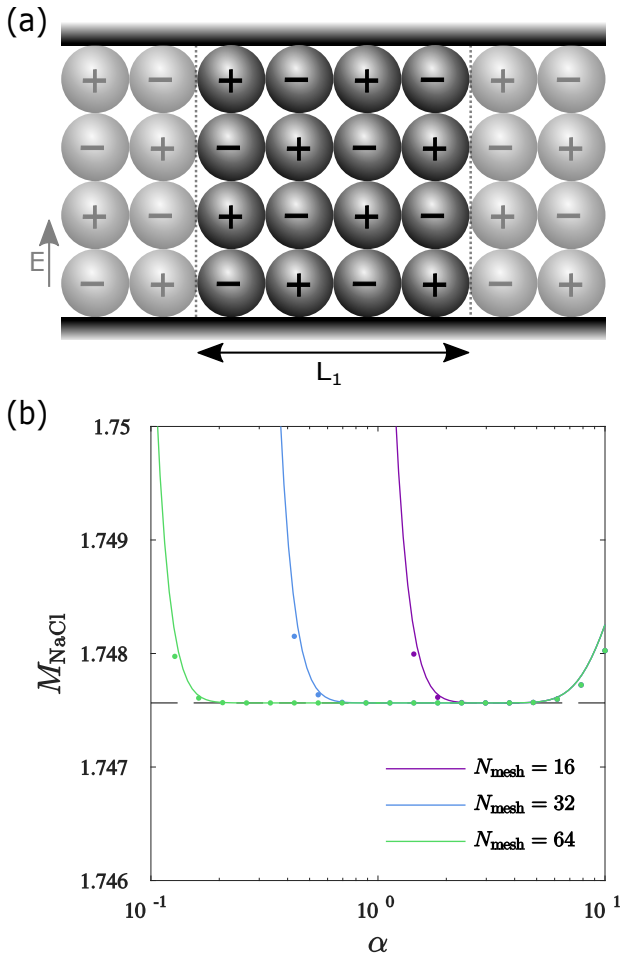

Figure B.1: Validation of charge-potential relation for far-field calculation using First order Madelung constant. (a) Schematic depicts the NaCl lattice with 2x2x2 supercell of alternating charges within a confined media. (b) Exact value of Madelung constant for NaCl crystal has been calculated by `Kittel(1976)`[120]; Variation of First order Madelung constant against splitting parameter, has been plotted for different number of mesh points, N_{mesh} where solid lines indicate the results for periodic media while dots depict the confined media.

where $\acute{S}$ represents the dipole sum for the simple cubic dipole lattice while p denotes the polarisation. As suggested in Nijboer[152], care must be taken when performing

the dipole sum as the sum represented in (B.2) is conditionally convergent and order of summation impacts the value of dipole sum. Taking the correct order of summation for the simple cubic lattice of equal point dipoles in *z-direction* yields constant value of $8\pi/3$ according to the Lorentz' theory.

The variation of second order Madelung constant at different values of number of mesh points as shown in Figure B.2(b) is due to the fact that wave part contribution of far-field interaction represents dipole as decomposition into opposite charges placed on succeeding and preceding mesh points in the direction parallel to the direction of dipoles hence smaller mesh spacing better captures the approximation compared to larger mesh spacing as has been illustrated by Figure B.3.

B.1.3 Conductivity of simple cubic lattice

The first order and second order Madelung constants described above are respectively helpful in validating the relationship between charge-potential and dipole-field pairs for the calculations involved in far-field interactions. The near-field interactions in the above described method are validated through calculation of effective conductivity for simple cubic lattice of particles at three different values of conductivity ratio $\lambda = 0.01$, $\lambda = 10$ and $\lambda \to \infty$. The method described above precisely calculates the value of effective conductivity even though contributions till the dipoles are considered. This relates to the fact that the quadrupole inclusion doesn't contribute to the grand potential matrix in this particular case as,

- Due to symmetric properties of simple cubic lattice.
- Neutrally charged particles in cubic array lead to zero quadrupole contribution.

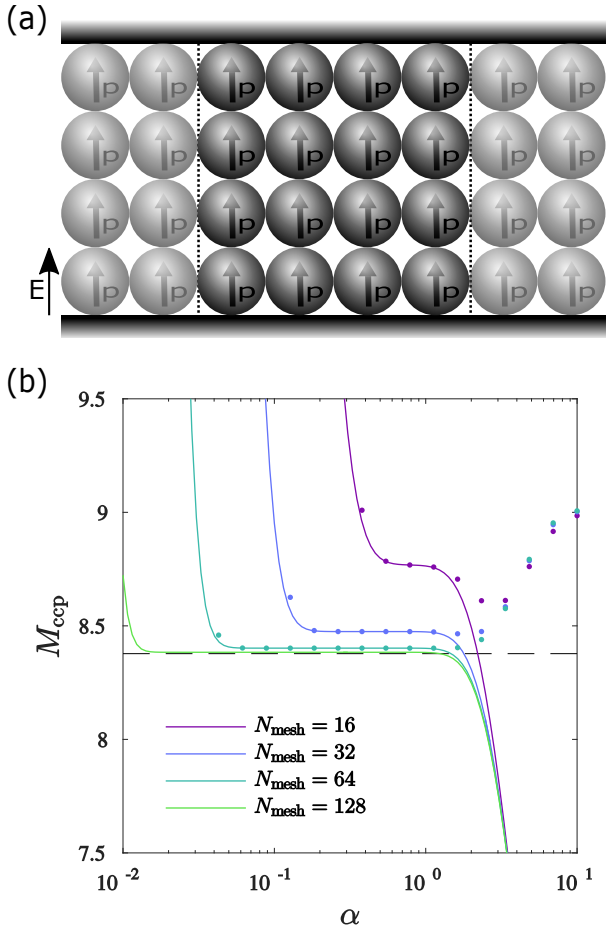

Figure B.2: Validation of dipole-potential gradient relation for far-field calculation using second order Madelung constant. (a) Schematic illustrates the confined 2x2x2 supercell containing point dipoles at the simple cubic lattice sites. (b) Analytical value of internal field generated by the lattice of point dipoles was demonstrated by `Nijboer(1958)`[152] ; Variation of Second order Madelung constant at varying value of splitting parameter represented by has been plotted for different number of mesh points, N_{mesh} ; Solid lines indicate the results for periodic media while dots depict the confined media.

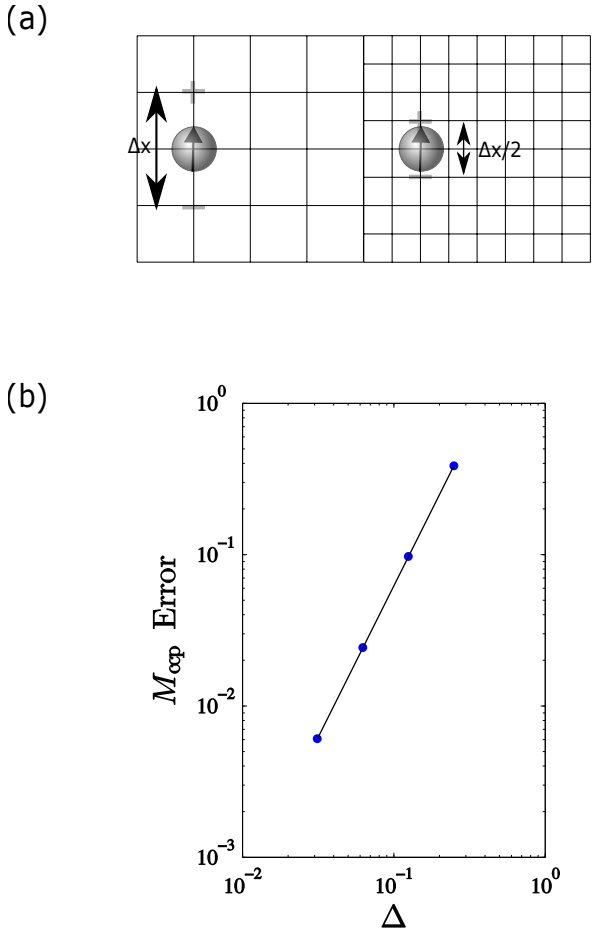

Figure B.3: Source of Error in Second order Madelung constant. (a) Schematic depicts a course and a fine grid points with grid spacing Δx and $\Delta x/2$, where $\Delta x = \frac{L_3}{N_{grid}}$. For a lattice of point dipoles, dipole at a particle center is represented by distributing opposite point charges on the grid points directly above and below the grid point with particle center. (b) The solid line with blue dots represent the deviation of second order Madelung constant value from the constant value of $(8\pi/3)p$ with the variation of grid spacing depicted by Δ.

B.2 Self-potential tensor Calculations

Here, we derive the self-potential tensor $\mathcal{P}^{(S)}$ for a single dielectric sphere n positioned between two parallel electrodes. The potential due to the particle's charge density

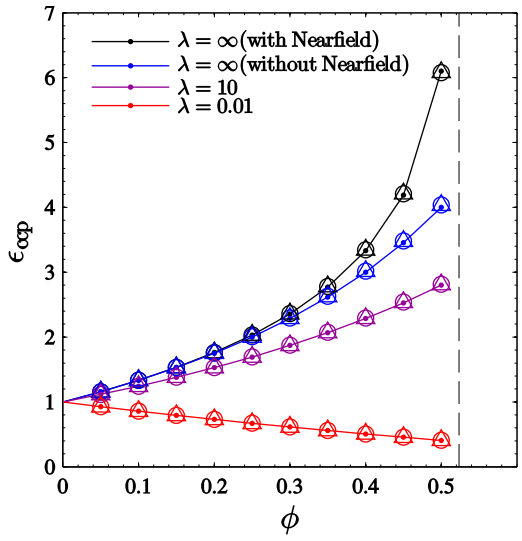

Figure B.4: Validation of Near-Field capacitance tensor for periodic and confined simple cubic lattice. Effective conductivity of system for variation in particle volume fraction at different values of conductivity ratio represented by $\lambda(=\frac{\epsilon_p}{\epsilon_m})$ is plotted. The results for effective conductivity against particle volume fraction in unbounded periodic simple cubic lattice have been previously demonstrated by `Bonnecaze (1990)`[18], have been reproduced in our calculation for both periodic ($\triangle$) and confined ($\bigcirc$) lattice.

$\rho_n(\mathbf{x})$ is given by

$$\phi_n(\mathbf{x}) = \int_V G(\mathbf{x}, \mathbf{x}')\rho_n(\mathbf{x}')d\mathbf{x}', \tag{B.3}$$

where $G(\mathbf{x}, \mathbf{x}')$ is the Green's function for a point charge between parallel electrodes. The Green's function can be divided in two contributions: (1) that due to a point charge in an unbounded medium, $J(\mathbf{x}, \mathbf{x}') = 1/4\pi\varepsilon r$, and (2) a correction due to the reflection off the two walls, $J_w(\mathbf{x}, \mathbf{x}')$, such that

$$G(\mathbf{x}, \mathbf{x}') = J(\mathbf{x}, \mathbf{x}') + J_w(\mathbf{x}, \mathbf{x}').$$

Inspection of equation (3.12) reveals that the Fourier coefficients of these two contributions are given by

$$J^{(k)}(x_3, x_3') = \frac{e^{-2\pi k|x_3 - x_3'|}}{4\pi k\varepsilon}, \tag{B.4}$$

$$J_w^{(k)}(x_3, x_3') = -\frac{e^{-2\pi k x_3}}{4\pi k\varepsilon}\frac{\sinh(2\pi k(L_3 - x_3'))}{\sinh(2\pi k L_3)} - \frac{e^{-2\pi k(L_3 - x_3)}}{4\pi k\varepsilon}\frac{\sinh(2\pi k x_3')}{\sinh(2\pi k L_3)}. \tag{B.5}$$

Expanding (B.3) in a Taylor series about the center of the particle and integrating the potential over the spherical surface of particle n, one can show that

$$\phi_n(\mathbf{x}_n) = P_{\Phi q}^{(S)} q_n + \mathbf{P}_{\Phi p}^{(S)} \cdot \mathbf{p}_n + \ldots,$$

where the elements of the self-potential tensor $\mathcal{P}^{(S)}$ are given by

$$P_{\Phi q}^{(S)} = \frac{1}{4\pi\varepsilon a_n}\left(1 + \frac{1}{2\lambda}\right) + J_w(\mathbf{x}_n, \mathbf{x}_n),$$

$$\mathbf{P}_{\Phi p}^{(S)} = \nabla_{\mathbf{x}'} J_w(\mathbf{x}, \mathbf{x}')\big|_{\mathbf{x}'=\mathbf{x}_n}^{\mathbf{x}=\mathbf{x}_n},$$

with $\lambda = \varepsilon_p/\varepsilon$. Here, we have assumed that the charge on the particle is distributed uniformly throughout its interior[18]; the special case of a conductive particle[56] corresponds to the limit as $\lambda \to \infty$.

Similarly, by integrating the product of $\mathbf{x} - \mathbf{x}_n$ and $\phi_n(\mathbf{x})$ over the surface of the sphere, one obtains

$$0 = \mathbf{P}_{Eq}^{(S)} q_n + \mathbf{P}_{Ep}^{(S)} \cdot \mathbf{p}_n + \ldots,$$

where the elements of $\mathcal{P}^{(S)}$ are given by

$$\mathbf{P}_{Eq}^{(S)} = \nabla_{\mathbf{x}} J_w(\mathbf{x}, \mathbf{x}')\big|_{\mathbf{x}'=\mathbf{x}_n}^{\mathbf{x}=\mathbf{x}_n},$$

$$\mathbf{P}_{Ep}^{(S)} = \frac{1}{4\pi\varepsilon a_n^3}\left(\frac{\lambda+2}{\lambda-1}\right) + \nabla_{\mathbf{x}}\nabla_{\mathbf{x}'} J_w(\mathbf{x}, \mathbf{x}')\big|_{\mathbf{x}'=\mathbf{x}_n}^{\mathbf{x}=\mathbf{x}_n}.$$

Using the Fourier coefficients (B.5) for the reflected component of the Green's function, the components of the self-potential tensor $\mathcal{P}^{(S)}$ can be written more explicitly as

$$P_{\Phi q}^{(S)} = \frac{1}{4\pi\varepsilon a_n}\left[\left(1+\frac{1}{2\lambda}\right)+\frac{1}{2}\left(\psi^{(0)}(\Xi)+\psi^{(0)}(1-\Xi)+2\gamma\right)\left(\frac{a_n}{L_3}\right)\right], \tag{B.6}$$

$$\mathbf{P}_{\Phi p}^{(S)} = \mathbf{P}_{Eq}^{(S)} = \frac{1}{4\pi\varepsilon a_n^2}\left[\frac{1}{4}\left(\psi^{(1)}(\Xi)-\psi^{(1)}(1-\Xi)\right)\left(\frac{a_n}{L_3}\right)^2\right]\mathbf{e}_3, \tag{B.7}$$

$$\begin{aligned}\mathbf{P}_{Ep}^{(S)} = \frac{1}{4\pi\varepsilon a_n^3}\Bigg\{&\left[\frac{\lambda+2}{\lambda-1}\right]\mathbf{I}+\left[\frac{1}{8}\left(\psi^{(2)}(\Xi)+\psi^{(2)}(1-\Xi)-4\zeta(3)\right)\left(\frac{a}{L_3}\right)^3\right]\mathbf{e}_3\mathbf{e}_3\\ &-\left[\frac{1}{16}\left(\psi^{(2)}(\Xi)+\psi^{(2)}(1-\Xi)+4\zeta(3)\right)\left(\frac{a}{L_3}\right)^3\right](\mathbf{I}-\mathbf{e}_3\mathbf{e}_3)\Bigg\}.\end{aligned} \tag{B.8}$$

Here, $\psi^{(m)}(\ )$ is the polygamma function of order m, γ is Euler's constant, $\zeta(\ )$ is the Riemann zeta function, and $\Xi = x_3^{(n)}/L_3$.

B.3 Wave-space contribution to the self-potential tensor

The potential due to the global charge distribution of a single particle n is given by

$$\phi_g(\mathbf{x}) = \int_V G_g(\mathbf{x}, \mathbf{x}'; \alpha)\rho_n(\mathbf{x}')d\mathbf{x}',$$

where $G_g(\mathbf{x}, \mathbf{x}'; \alpha)$ is the Green's function for a single Gaussian envelope between parallel electrodes. Expanding in a Taylor series about the center of the particle, we can write

$$\phi_g(\mathbf{x}) = q_n G_g(\mathbf{x}, \mathbf{x}_n; \alpha) + \mathbf{p}_n \cdot \nabla_{\mathbf{x}'} G_g(\mathbf{x}, \mathbf{x}'; \alpha)|_{\mathbf{x}'=\mathbf{x}_n} + \ldots.$$

Evaluating the potential and the potential gradient at the center of the particle, the elements of the self-potential tensor due to the global charge distribution are identified as

$$\begin{aligned}
P_{\Phi q}^{(S_g)} &= G_g(\mathbf{x}_n, \mathbf{x}_n; \alpha), \\
\mathbf{P}_{\Phi p}^{(S_g)} &= \nabla_{\mathbf{x}'} G_g(\mathbf{x}, \mathbf{x}'; \alpha)|_{\mathbf{x}'=\mathbf{x}_n}^{\mathbf{x}=\mathbf{x}_n}, \\
\mathbf{P}_{Eq}^{(S_g)} &= \nabla_{\mathbf{x}} G_g(\mathbf{x}, \mathbf{x}'; \alpha)|_{\mathbf{x}'=\mathbf{x}_n}^{\mathbf{x}=\mathbf{x}_n}, \\
\mathbf{P}_{Ep}^{(S_g)} &= \nabla_{\mathbf{x}} \nabla_{\mathbf{x}'} G_g(\mathbf{x}, \mathbf{x}'; \alpha)|_{\mathbf{x}'=\mathbf{x}_n}^{\mathbf{x}=\mathbf{x}_n},
\end{aligned}$$

where the Green's function is computed from equation (2.3.5) by application of the inverse Fourier transform. These have the general form

$$P_{\Phi q}^{(S_g)} = \frac{1}{4\pi\varepsilon L_3} f_1^{(\Phi q)}(\Xi, \beta), \tag{B.9}$$

$$\mathbf{P}_{\Phi p}^{(S_g)} = \mathbf{P}_{Eq}^{(S_g)} = \frac{1}{4\pi\varepsilon L_3^2} f_2^{(Eq)}(\Xi, \beta)\mathbf{e}_3, \tag{B.10}$$

$$\begin{aligned}
\mathbf{P}_{Ep}^{(S_g)} = \frac{1}{4\pi\varepsilon L_3^3} \Big[& f_3^{(Ep)}(\Xi, \beta)\mathbf{e}_3\mathbf{e}_3 \\
& + g_3^{(Ep)}(\Xi, \beta)(\mathbf{I} - \mathbf{e}_3\mathbf{e}_3) \Big],
\end{aligned} \tag{B.11}$$

where $\Xi = x_n^{(3)}/L_3$ and $\beta = \alpha/L_3^2$. The dimensionless functions $f(\ )$ and $g(\ )$ are illustrated in figure XXX.

B.4 Pairwise capacitance functions

B.4.1 Sphere-sphere functions

Near-field contributions to the grand capacitance tensor are computed in a pairwise fashion using analytical results for two conductive spheres subject to an electric field. For two equally-sized spheres (1 and 2) located at $\mathbf{x}_1$ and $\mathbf{x}_2$, respectively, within an external potential $\varphi^\infty(\mathbf{x}) = -\mathbf{x}\cdot\mathbf{E}^\infty$, the sphere charges q and dipole moments $\mathbf{p}$ can be expressed as

$$\begin{bmatrix} q_1 \\ q_2 \\ \mathbf{p}_1 \\ \mathbf{p}_2 \end{bmatrix} = \begin{bmatrix} A_{11} & A_{12} & \tilde{\mathbf{B}}_{11} & \tilde{\mathbf{B}}_{12} \\ A_{21} & A_{22} & \tilde{\mathbf{B}}_{21} & \tilde{\mathbf{B}}_{22} \\ \mathbf{B}_{11} & \mathbf{B}_{12} & \mathbf{C}_{11} & \mathbf{C}_{12} \\ \mathbf{B}_{21} & \mathbf{B}_{22} & \mathbf{C}_{21} & \mathbf{C}_{22} \end{bmatrix} \begin{bmatrix} \Phi_1 - \varphi^\infty(\mathbf{x}_1) \\ \Phi_2 - \varphi^\infty(\mathbf{x}_2) \\ \mathbf{E}^\infty \\ \mathbf{E}^\infty \end{bmatrix}, \tag{B.12}$$

where the capacitance coefficients $\mathbf{A}$, $\mathbf{B}$, and $\mathbf{C}$ depend only on the displacement vector $\mathbf{r} = \mathbf{x}_2 - \mathbf{x}_1$. Using the solution of Davis [45], the capacitance coefficients $\mathbf{A}$ can be written as

$$A_{11} = A_{22} = 8\pi\varepsilon b S_0(\mu), \tag{B.13}$$

$$A_{12} = A_{21} = -8\pi\varepsilon b S_0(0), \tag{B.14}$$

where b and μ are geometric quantities defined as

$$b = \frac{1}{2}\sqrt{r^2 - 4a^2} text \quad and \quad \mu = \ln\left(\frac{r + \sqrt{r^2 - 4a^2}}{a}\right), \tag{B.15}$$

and the function $S_m(\xi)$ is given by the infinite sum

$$S_m(\xi) = \sum_{n=0}^{\infty} \frac{(2n+1)^m e^{(2n+1)\xi}}{e^{(4n+2)\mu} - 1}. \tag{B.16}$$

Similarly, the $\mathbf{B}$ coefficients can be written as

$$\mathbf{B}_{11} = \tilde{\mathbf{B}}_{11} = -\mathbf{B}_{22} = -\tilde{\mathbf{B}}_{22} = X_{11}^B \hat{\mathbf{r}}, \tag{B.17}$$

$$-\mathbf{B}_{12} = -\tilde{\mathbf{B}}_{21} = \mathbf{B}_{21} = \tilde{\mathbf{B}}_{12} = X_{12}^B \hat{\mathbf{r}}, \tag{B.18}$$

where $\hat{\mathbf{r}}$ is the unit vector directed from sphere 1 to sphere 2, and X_{11}^B and X_{12}^B are the scalar functions

$$X_{11}^B = -8\pi\varepsilon b[bS_1(\mu) - \tfrac{1}{2}rS_0(\mu)], \tag{B.19}$$

$$X_{12}^B = -8\pi\varepsilon b[bS_1(0) - \tfrac{1}{2}rS_0(0)]. \tag{B.20}$$

Finally, the $\mathbf{C}$ coefficients are given by

$$\mathbf{C}_{\alpha\beta} = X_{\alpha\beta}^C \hat{\mathbf{r}}\hat{\mathbf{r}} + Y_{\alpha\beta}^C (\mathbf{I} - \hat{\mathbf{r}}\hat{\mathbf{r}}), \tag{B.21}$$

where $\mathbf{I}$ is the identity tensor and the functions $X_{\alpha\beta}^C$ and $Y_{\alpha\beta}^C$ are given by

$$X_{11}^C = X_{22}^C = 8\pi\varepsilon b \left[b^2 S_2(\mu) - rbS_1(\mu) + \tfrac{1}{4}r^2 S_0(\mu)\right], \tag{B.22}$$

$$X_{21}^C = X_{12}^C = 8\pi\varepsilon b \left[b^2 S_2(0) - rbS_1(0) + \tfrac{1}{4}r^2 S_0(0)\right], \tag{B.23}$$

$$Y_{11}^C = Y_{22}^C = 16\pi\varepsilon b^3 S'(\mu), \tag{B.24}$$

$$Y_{21}^C = Y_{12}^C = -16\pi\varepsilon b^3 S'(0), \tag{B.25}$$

where the function $S'(\xi)$ is given by the infinite sum

$$S'(\xi) = \sum_{n=1}^{\infty} \frac{n(n+1)e^{(2n+1)\xi}}{e^{(4n+2)\mu} - 1}. \tag{B.26}$$

B.4.2 Sphere-plane functions

The interaction between a conductive sphere 1 and a grounded plane subject to a field normal to its surface is readily obtained using the sphere-sphere results from

the previous section. The boundary condition on the grounded plane is satisfied by adding a fictitious "image" particle of equal size, opposite charge, and equal dipole moment on the opposite side of the plane. These conditions imply that the potential on the image particle (denoted 2) satisfies $\Phi_2 - \varphi^\infty(\mathbf{x}_2) = -\Phi_1 + \varphi^\infty(\mathbf{x}_1)$, where $\mathbf{x}_2$ is the position of the image. For a sphere above the lower boundary at $x_3 = 0$, the image particle is located at $\mathbf{x}_2 = \mathbf{x}_1 - 2x_3^{(1)}\mathbf{e}_3$. In this way, we obtain the following "self" contribution to the capacitance tensor

$$\begin{bmatrix} q_1 \\ \mathbf{p}_2 \end{bmatrix} = \begin{bmatrix} A_{11} - A_{12} & \tilde{\mathbf{B}}_{11} + \tilde{\mathbf{B}}_{12} \\ \mathbf{B}_{11} - \mathbf{B}_{12} & \mathbf{C}_{11} - \mathbf{C}_{12} \end{bmatrix} \begin{bmatrix} \Phi_1 - \varphi^\infty(\mathbf{x}_1) \\ \mathbf{E}^\infty \end{bmatrix}, \tag{B.27}$$

where the capacitance coefficients $\mathbf{A}$, $\mathbf{B}$, and $\mathbf{C}$ are defined in the previous section. The contribution of the upper boundary at $x_3 = L_3$ is obtained in similar fashion by introducing an image particle at $\mathbf{x}_2 = \mathbf{x}_1 + 2(L_3 - x_3^{(2)})\mathbf{e}_3$.

Appendix C

C.0.1 Evolution of traveling waves

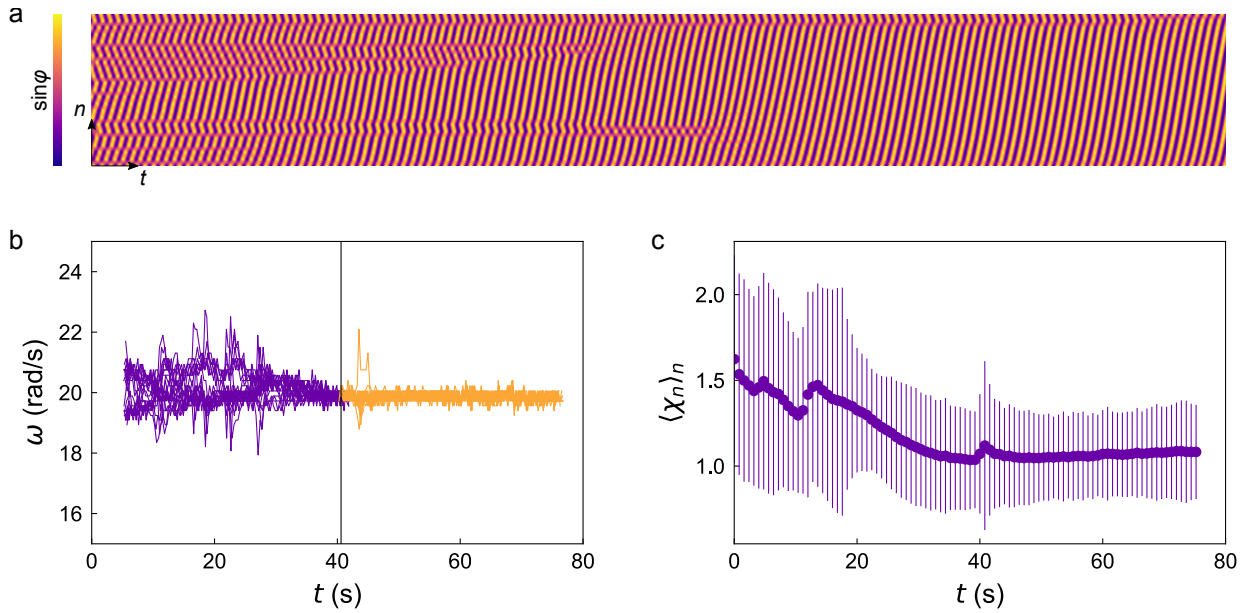

Figure C.1: (a) Full length space-time plot showing the development of traveling wave synchronization (see Figure 1d and Supplemental Movie 1). (b) Instantaneous oscillation frequency of each oscillator as a function of time during the development of synchronization. The onset of the fully synchronized state is denoted by the change in color from purple to yellow. (c) Average phase difference as a function of time during the development of synchronization. Error bars represent standard deviations in the phase difference. Data were collected for $N = 23$, $a = 1$ mm, $W = 3$ mm, $L = 25$ mm, and $V = 19$ kV.

C.0.2 Dependence of wavelength on the number of oscillators

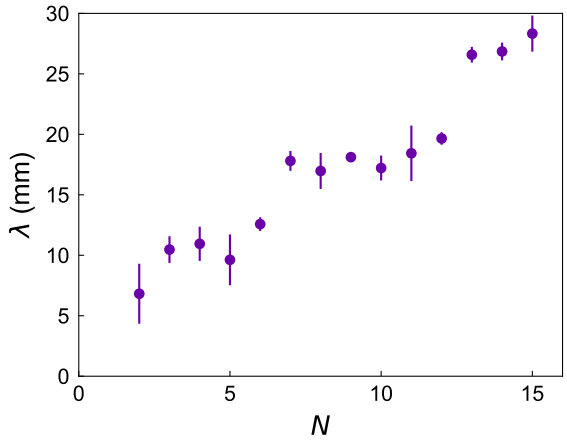

Figure C.2: Wavelength λ (defined in the main text) as a function of the number of oscillators $N < N^* = 15$. Error bars denote the standard deviation obtained over 50 cycles. Data were collected with $a = 1$ mm, $L = 25$ mm, $W = 3$ mm, and $V = 18$ kV.

C.0.3 Dependence of breaking frequency on oscillator number $N > N^*$

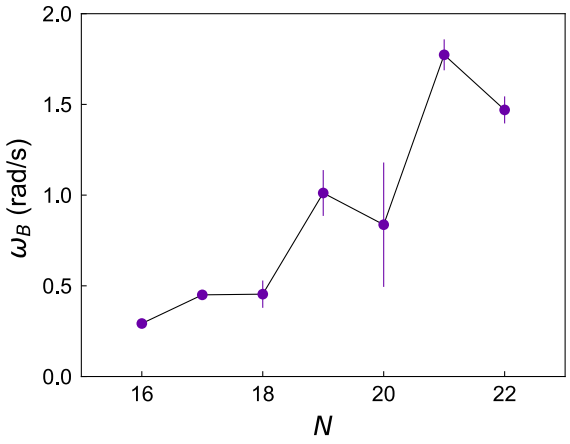

Figure C.3: Breaking frequency frequency ω_B as a function of the oscillator number $N > N^* = 15$. Error bars denote standard deviations obtained over at least five breaking events. Data were collected with $a = 1$ mm, $L = 25$ mm, $W = 3$ mm, and $V = 18$ kV.

C.0.4 Space-time plot for $N \gg N^*$

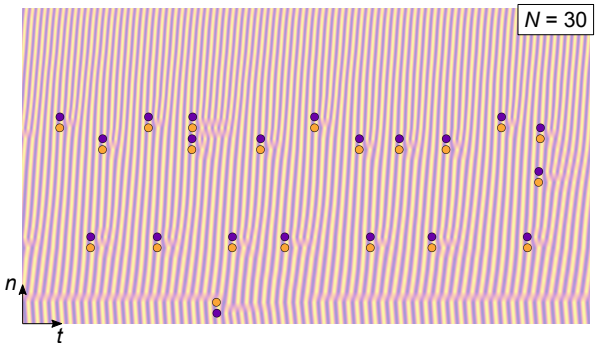

Figure C.4: Space-time plot for $N \gg N^*$ showing wave breaking at different locations and irregular time intervals. Wave breaks are characterized by edge dislocations highlighted by the markers, which show points in the space-time lattice with five-fold (purple) and seven-fold (yellow) coordination. Data were collected with $a = 1$ mm, $L = 25$ mm, $W = 3$ mm, and $V = 18$ kV. See also Supplemental Movie 5.

C.0.5 Control experiments on the role of hydrodynamic interactions

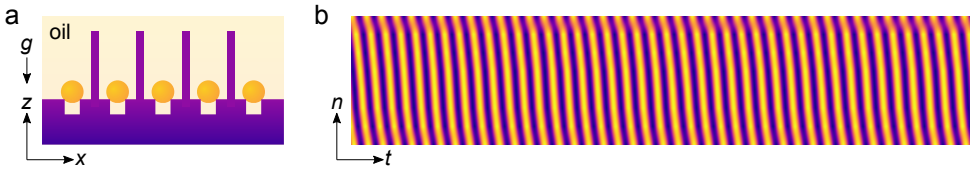

Figure C.5: (a) Experiments were performed in which particles were separated by solid walls to eliminate hydrodynamic interactions between neighboring particles. (b) Space-time plot showing traveling wave synchronization in the absence of hydrodynamic interactions. Data were collected with $N = 8$, $a = 1$ mm, $W = 4$ mm, $L = 25$ mm, and $V = 19$ kV.

Appendix D

Directed motion of metallodielectric particles bycontact charge electrophoresis

Introduction

[1]Self-propelled colloidal particles harness energy from their environment to power directed motions relative to their fluid surroundings [64, 132, 49]. Inspired by the locomotion of micro-organisms [130], these artificial swimmers are actively pursued for their potential to navigate complex environments [195, 42] and deliver cargo to targeted locations[79, 10]. Fluid flows induced by particle motions can also serve to enhance rates of mass transfer to/from the particle surface with emerging applications

[1]The material presented in this chapter has been reprinted with permission from Yong Dou, Charles A. Cartier, Wenjie Fei, Shashank Pandey, SepidehRazavi, Ilona Kretzschmar, and Kyle J. M. Bishop, Langmuir 2016, 32, 49, 13167-13173. Copyright 2018 American Chemical Society.

in water remediation[185, 133] and chemical detection[145, 115]. When many self-propelled particles get together, they often interact to form dynamic assemblies[209] such as swarms[98, 150], flocks [27], clusters[111], and crystals [157]. Synthetic realizations of such active matter[137] provide useful models by which to explore the many forms of self-organization that arise outside of thermodynamic equilibrium. Importantly, the diverse behaviors of motile particles depend critically on the specific mechanism of self-propulsion and on the associated interactions among the particles. Expanding the repertoire of colloidal self-propulsion can therefore enable the discovery of new dynamical behaviors as well as the development of future applications.

A wide variety of physicochemical mechanisms have been applied to power the self-propulsion of colloidal particles. Self-phoretic mechanisms[85] use asymmetries in particle shape and/or composition to create local gradients in the electric potential[28], chemical composition[97], or temperature[110] that drive particle motions via interfacial phoretic effects such as electrophoresis, diffusiophoresis, or thermophoresis, respectively[6]. In a classic example[164, 72], bimetallic nanorods move autonomously through a homogeneous liquid containing a suitable chemical fuel via reaction-induced self-electrophoresis[210, 146]. Self-propelled motions of asymmetric particles can also be powered by external fields. Alternating electric fields drive motions of polarizable particles by induced charge electrophoresis [189, 78, 22]; alternating magnetic fields power the swimming of flexible magnetic particles by inducing non-reciprocal beating motions [61]; acoustic fields propel dense metallic particles by directing steady streaming flows[207, 148, 3]. These examples of field-driven particle motion are generally considered forms of self-propulsion, as they allow particles to move freely in multiple directions (typically those perpendicular to the applied field). The use of

external fields to power such motions is attractive for studies of active matter as their magnitude is tunable in space and time.

Here, we describe a type of colloidal self-propulsion in which an electric field drives the autonomous motion of metallodielectric Janus particles[167, 163] within an insulating liquid between two plane electrodes (Fig. D.1a). Similar configurations have been used to investigate particle motions powered by induced charge electrophoresis within conductive liquids[22] and by Quicke rotation within weakly conductive liquids [27]. By contrast, field-driven motions of conductive particles in insulating liquids are driven by contact charge electrophoresis (CCEP) whereby particles acquire charge on contact with a biased electrode and then move in the field emanating from that electrode [57, 31, 53]. In one well studied example, a conductive sphere immersed in mineral oil oscillates rapidly between two electrodes subject to a constant voltage [53]. Each time the particle contacts an electrode, it acquires charge of opposite polarity and moves back towards the other electrode thereby transporting charge down the applied potential gradient. Harnessing these motions for useful functions requires strategies by which to rectify particle oscillations. One approach is to modify the electrodes with asymmetric, ratchet-like features that enable directed transport of conductive particles[57] or droplets[203]. Here, we introduce an alternative strategy that relies on particle asymmetries to achieve similar directed motions.

We show that oscillations of Janus particles between two parallel electrodes is accompanied by steady motions directed perpendicular to the applied field. Through experiment and theory, we develop and validate a mechanism of self-propulsion whereby the field-induced rotation of the particle upon charge reversal at the electrode surface results in its net displacement during each oscillation cycle. Repeated displacements

in a common direction propel Janus particles at speeds of up to 600 μm/s along wide circular arcs within the plane of the electrodes. Beyond the dynamics of individual particles, we show how particles can both attract or repel one another depending on their separation and on the phases of their respective oscillations. Together, these results demonstrate how particle symmetry can be used to direct the motions of active colloids powered by CCEP. The ability to engineer the motions of individual particles and their assemblies will ultimately contribute to the realization of colloidal machines that organize and operate autonomously to perform useful functions [186].

Results and Discussion

In a typical experiment, a dilute suspension of Janus particles in mineral oil was sandwiched between two transparent indium tin oxide (ITO) electrodes separated by a distance $H = 50 - 250$ μm (Fig. D.1a). We used two types of Janus particles: 8 μm silica particles and 4 μm fluorescent polystyrene particles, each coated on one hemisphere by a thin layer of gold. In the absence of an applied field, the particles settled to the surface of the lower electrode where they were imaged from above by an optical microscope. Application of a constant voltage $V = 200 - 1000$ V caused the particles to oscillate rapidly between the electrodes, as evidenced by their periodic appearance and disappearance from the focal plane (Fig. D.1b). Each time a particle came into focus, its position was displaced slightly from that in the previous cycle. The magnitude and direction of these displacements was relatively constant from one cycle to the next resulting in steady particle motions perpendicular to the applied field. Using high speed imaging, we quantified the frequency f of particle oscillations

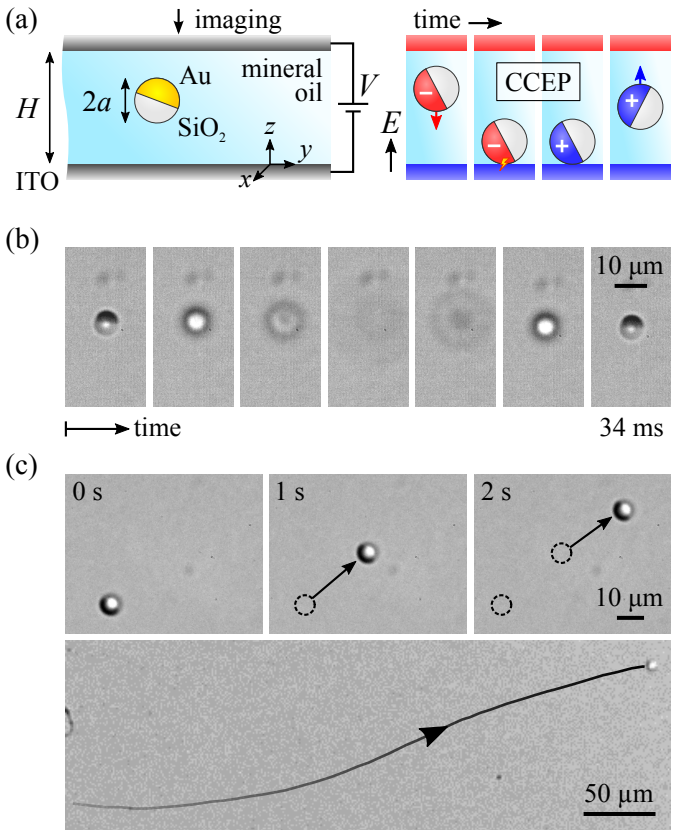

Figure D.1: (a) Schematic illustration of the experimental setup. A metallodieletric Janus particle is immersed in mineral oil between two parallel ITO electrodes (left). Application of a constant voltage V results in the oscillatory motion of the particle via contact charge electrophoresis (CCEP; right). (b) When imaged from above, the particle moves in and out of focus in time as it oscillates between the electrodes. (c) Over many oscillation cycles, the particle moves steadily away from its conductive hemisphere (top); the steady motion of the particle continues over hundreds of microns (bottom). See supporting videos 1, 2, and 3.

as well as the particle position (x_p, y_p) at each oscillation cycle. For example, at $V = 400$ V and $H = 200$ μm, a silica Janus particle oscillated between the electrodes at an average frequency of $f = 29$ Hz and moved perpendicular to the field at an average speed of $U_\perp = 25$ μm/s (Fig. D.1c). Directed particle motion continued over large distances for as long as the voltage was applied.

Figure D.2a shows the reconstructed trajectories of six different Janus particles under identical conditions over the course of one hundred oscillation cycles. The cumulative displacement of each particle increased roughly linearly with the number of oscillations (Fig. D.2b) as the particles moved along wide circular arcs of radii 30 μm or greater. These observations are consistent with the spatial homogeneity of the applied field, which suggests that particle motion be invariant to translation and rotation in the xy plane of the electrodes. Although the majority of particles (ca. 70% for $V = 800$ V and $H = 200$ μm) exhibited such directed motions, some Janus particles were observed to oscillate between the electrodes with no lateral motion whatsoever. Additionally, some particles (ca. 20%) remained "stuck" to the electrode surface and did not move at all upon application of the field.

For the particles that moved, the oscillation frequency increased monotonically with increasing voltage as $f \propto V^2$ (Fig. D.2c). This observation is consistent with previous studies of CCEP motion, which showed that the oscillation frequency scales as $f \sim \varepsilon a V^2/\eta H^3$, where ε and η are the permittivity and viscosity of the fluid, respectively, and a is the particle radius [53]. By contrast, the lateral displacement of the particle during each oscillation cycle was largely independent of the applied voltage; each oscillation contributed an average displacement of $\Delta = 0.2a$ (Fig. D.2d). Consequently, the lateral velocity of the particle, $U_\perp \equiv f\Delta$, also increased as the

square of the applied voltage (Fig. D.2e). This velocity could be further increased by decreasing the spacing between the electrodes H to increase the magnitude of the applied field (Fig. D.2f). Using spacers of $H = 50$ μm, we observed particles velocities up to $U_{\perp} = 600$ μm/s in the direction perpendicular to the applied field.

To explain these experimental observations, we propose the following propulsion mechanism illustrated in Figure D.3a. As it moves across the channel, a charged Janus particle adopts a preferred orientation in which its principal axis is oblique to the applied field and its motion is directed towards the metallic hemisphere. When it contacts either electrode, the charge on the particle changes sign thereby altering its preferred orientation in the field. The field-induced rotation of the particle in the vicinity of the electrode surface results in a lateral displacement, which is qualitatively similar to that of a sphere "rolling" along the surface. Successive rotations occur in a common direction towards the non-metallic hemisphere causing a steady lateral motion over the course of many oscillations. This putative mechanism is supported both by experimental observations of the transient particle orientation and by a mathematical model that describes the electrostatics and hydrodynamics of CCEP motion.

We used fluorescent particles to better visualize the orientation of Janus particles moving by CCEP. Such particles appeared bright when the metallic hemisphere was directed "down" (negative z direction; away from the microscope objective) and dark when the metallic hemisphere was directed "up" (positive z direction; towards the objective). For intermediate orientations, the fluorescent hemisphere of the particle was partially visible like the bright side of the moon in different phases. By focusing on planes in the middle of the two electrodes, we observed that particles moving

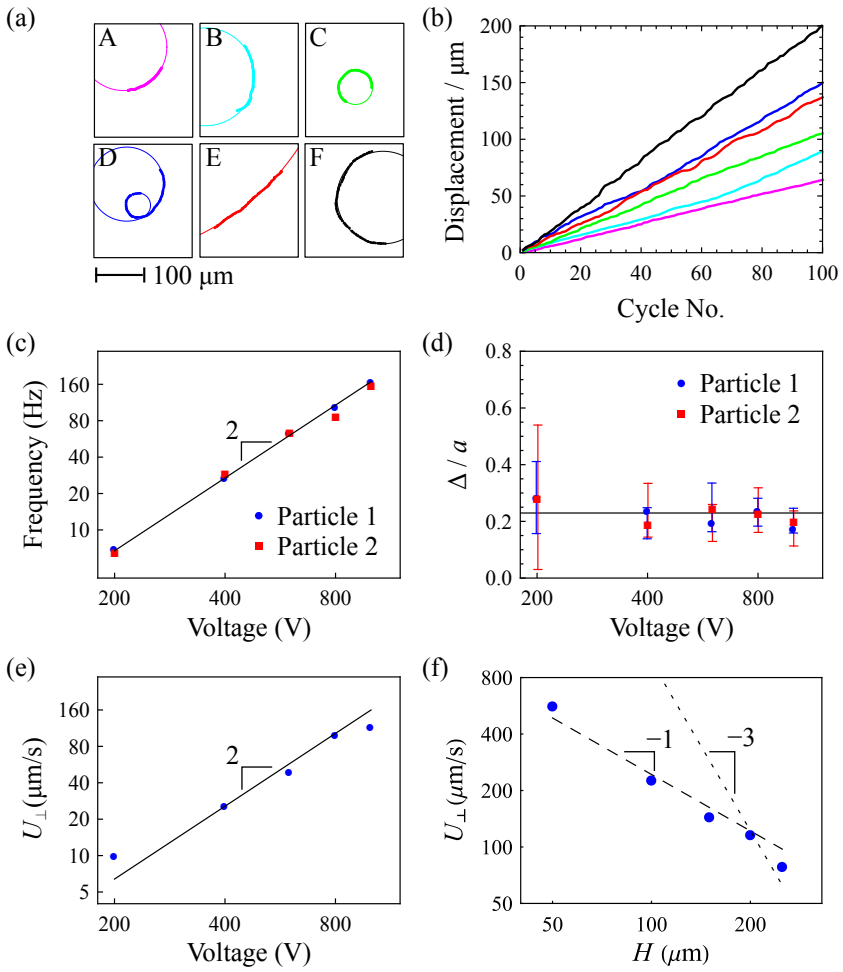

Figure D.2: (a) Reconstructed particle trajectories of six Janus particles (radius $a = 4$ μm; voltage $V = 800$ V; electrode spacing $H = 200$ μm). Markers denote the particle position at successive oscillations; curves are best circular fits to the data. (b) The cumulative displacement of particles in (a) increases linearly with the number of oscillation cycles. (c) The oscillation frequency of the particle scales quadratically with the voltage. Markers show data for two independent particles with an electrode spacing $H = 200$ μm; the curve is a fit of the form $f \propto V^2$. (d) The lateral particle displacement Δ during each oscillation is largely independent of the applied voltage. Markers show the mean displacement; error bars denote one standard deviation above and below the mean. (e) The particle velocity perpendicular to the field scales as the square of the voltage. Markers show data for one particle with an electrode spacing $H = 200$ μm; the curve is a fit of the form $U_\perp \propto V^2$. (f) Particle velocity increases with decreasing electrode spacing. Each marker represents the velocity of a single particle for an applied voltage $V = 800$ V.

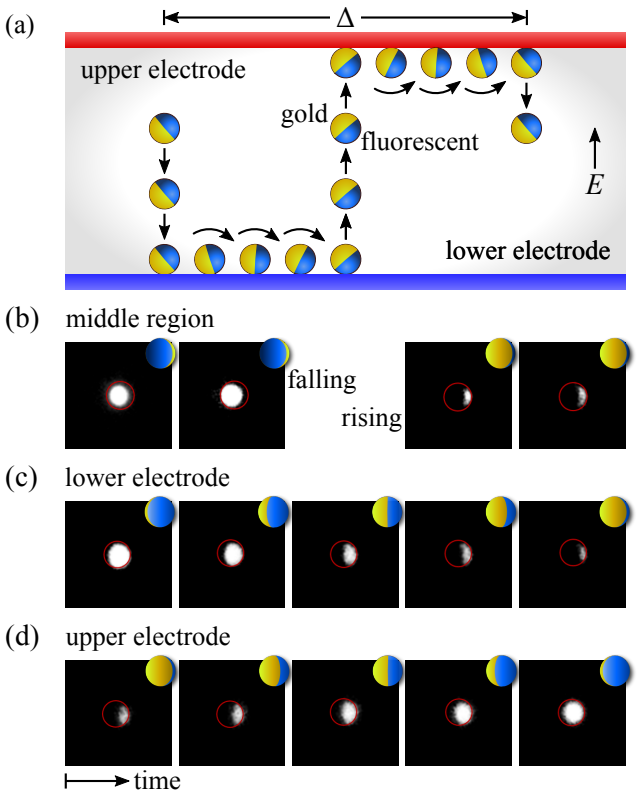

Figure D.3: (a) Schematic illustration of the propulsion mechanism showing one oscillation cycle. Rotation of the particle near the electrodes results in a lateral displacement Δ. (b-d) Fluorescent microscopy images highlight the non-metallic hemispheres of fluorescent Janus particles. Images are captured from above; the icons show the particles viewed from above using the color scheme from (a). Particles in the middle region (b) adopt a stable orientation that depends on their direction of travel (falling vs. rising). Upon contacting the lower (c) or upper (d) electrode, particles rotate in time from one orientation to another. See supporting video 4.

downward appeared bright (gibbous moon) while those moving upward appeared dark (crescent moon) (Fig. D.3b). By focusing on the lower electrode, we directly observed the rotation of the particle as it transitioned from the gibbous to crescent configuration (Fig. D.3c). The opposite behavior was observed at the upper electrode where the particle rotated from the crescent to gibbous configuration (Fig. D.3d). Importantly, the orientation of the Janus particle in the plane of the electrodes remained relatively constant from one cycle to the next, which allowed the particle to move steadily away from its metallic hemisphere.

To gain further insights into the propulsion mechanism, we use the equations of classical electrostatics and low-Reynolds number hydrodynamics to describe the dynamical trajectories of Janus particles moving by CCEP. In the model, both the liquid and the non-metallic hemisphere of the particle are treated as dielectrics with a common permittivity ε; the metallic hemisphere of the particle and the electrodes are treated as perfect conductors. We first consider the case of a single Janus particle with a net charge q in an unbounded medium subject to a uniform electric field E. We solve for the electric potential within the dielectric and evaluate the electrostatic torque $L(\alpha)$ on the particle as a function of its orientation α relative to the field. For each charge, there exists one stable orientation for which the electric torque is zero $L(\alpha) = 0$ and its derivative is negative $L'(\alpha) < 0$ (Fig. D.4a). Uncharged Janus particles tend to orient perpendicular to the applied field owing to the increased polarizability of their metallic hemisphere in that orientation ($\alpha = \pi/2$ for $q = 0$). The addition of positive or negative charge, respectively, acts to rotate the particle towards or away from the direction of the field. When the charge exceeds a critical magnitude, the particle orients perfectly with or against the applied field. Importantly, this critical

charge is similar in magnitude to that acquired by the particle during contact charging (see Fig. S2).

We now consider the dynamics of a particle "collision" with the lower electrode (Fig. D.4b). Initially, the particle is positioned far from the electrode surface ($z_p \gg a$) with some fixed charge q. We solve for the electrostatic force and torque on the particle, which, when properly non-dimensionalized, depend only on the particle charge q, orientation α, and height above the surface z_p. The electric force and torque induce both translational and rotational motions, which have been described previously for spherical particles above solid surfaces in the limit of zero Reynolds number [118]. We then integrate these dynamical equations of motion to describe the position and orientation of a single particle as function of time. Following our previous investigation of spherical particles [53], we assume that the particle makes electrical contact with the electrode at a finite surface separation δ and that the particle charge changes from q to $-q$. When suitably non-dimensionalized, this model has only two parameters: the particle charge $q/4\pi\varepsilon a^2 E$ and the separation at contact δ/a.

Figure D.4b shows three different particle trajectories for different contact separations and a common charge $q = 0.5q_s$ where $q_s = 4\pi\varepsilon a^2 E$ is a convenient charge scale. The trajectories are in qualitative agreement with the experimental observations: a particle moves towards the electrode with a preferred orientation, reverses its charge on contact, rotates and translates as it adopts a newly preferred orientation, and ultimately moves away from the surface. The net lateral displacement Δ depends on how closely the particle approaches the surface. For particles that approach more closely to the surface, their rotational motion is more tightly coupled to their lateral translation, and they move farther during each collision. The displacement

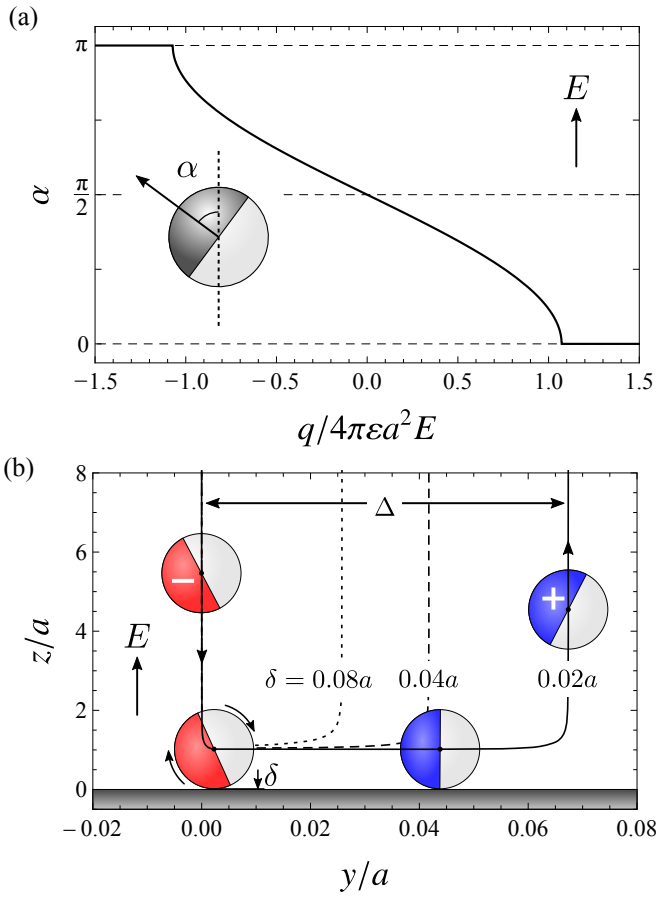

Figure D.4: Results of the theoretical model. (a) The stable orientation α of a Janus particle in a uniform electric field depends on the particle's charge q (scaled by $q_s = 4\pi\varepsilon a^2 E$). Uncharged particles align perpendicular to the applied field E ($\alpha = \pi/2$ for $q = 0$); highly charged particles align parallel to the field ($\alpha = 0, \pi$ for $|q| > 1.07q_s$). (b) Simulated particle "collisions" with the lower electrode for a particle charge $q = \pm 0.5q_s$. The solid curve shows the trajectory of the particle center; the orientation of the particle at different points along the trajectory is illustrated graphically. The net particle displacement Δ depends on the surface separation δ at contact when the particle charge reverses polarity. Note that for clarity the z and y axes use different scales.

also depends on the particle charge in an somewhat surprising way: highly charged particles ($q > q_s$) exhibit little or no displacement (Fig. S7). Such particles contact the surface with their axis aligned parallel with field and therefore experience little or no torque upon charge reversal. Instead, these particles move backward from the surface before ultimately rotating into the new stable orientation; particle rotation far from the surface, however, results in little or no lateral displacement. This prediction of the model provides a plausible explanation for those particles that oscillate but do not translate perpendicular to the field.

There are some experimental observations that are not captured by the idealized model. Notably, the model predicts that particles should move along straight lines and not the circular trajectories observed in experiment. We attribute this discrepancy to defects on the Janus particles that break their axial symmetry. Imperfections in the particles' metallic hemispheres are known to arise during metal deposition due to shadowing by neighboring particles [163]. Such defects can lead to electric torques about the principle axis of the particle, which are otherwise prohibited by symmetry. As a result, particles are permitted to change their orientation in the plane of the electrode upon charge reversal. Understanding these effects requires further study of non-axisymmetric particles of well defined shape. Interestingly, in some experiments, the curvature of the particle trajectory changed abruptly during its motion (e.g., particle D in Fig. D.2a). This observation may imply that non-axisymmetric particles are capable of multiple "modes" of self-propulsion; however, we cannot yet dismiss alternative explanations based on adventurous dust particles.

As noted above, the propulsion velocity is equal to the product of the oscillation frequency and the rotation-induced displacement: $U_\perp = f\Delta$. This expression

suggests two basic strategies for maximizing the particle velocity: (i) increase the oscillation frequency, $f \sim \varepsilon a V^2/\eta H^3$, or (ii) increase the lateral displacement upon charge reversal. The oscillation frequency can be enhanced by increasing the voltage or by decreasing the spacing between the electrodes (Fig. D.2e,f). Of course, the electrode spacing cannot be smaller than the particles themselves, and the electric field cannot exceed the dielectric strength of mineral oil (ca. 5 V/μm). In Figure D.2f, the applied field actually exceeds this threshold value for electrode spacings less than $H = 200$ μm; however, device failure was avoided by limiting the current to only 10 μA. Under these conditions, the electric field remains roughly constant, and the velocity scales as $U_\perp \propto H^{-1}$ (not $U_\perp \propto H^{-3}$ as expected for a constant voltage). To increase the rotation-induced displacement of the particle on charge reversal, it is necessary to alter the geometry of the particle itself (e.g., the size of the metallic patch). Such modifications can be challenging to achieve in practice and their consequences difficult to anticipate. Ultimately, the magnitude of the displacement is limited by the size of the particle ($\Delta < a$).

Beyond the motions of individual particles, we observed several interesting behaviors in systems of two or more interacting particles (Fig. D.5). When two particles were separated by a distance less than the electrode spacing ($d < H$), they influenced one another at a distance through electrostatic interactions. These interactions were either attractive or repulsive depending on the respective phases of the particle oscillations[143]. Like-charged particles oscillating "in phase" repelled one another as evidence by an increase in particle separation with time (Fig. D.5a). By contrast, oppositely-charged particles oscillating "out of phase" moved toward one another in time (Fig. D.5b). Due to slight differences in their oscillation frequencies, two par-

ticles often transitioned repeatedly between attractive and repulsive regimes. This particle "dance" could end in two different ways: either the particles moved off in different directions to find new partners, or they embraced one another to form a dynamic oscillating chain (a so-called bucket brigade [166]). Finally, we observed that interacting particles often moved together in a common direction – typically, along the line connecting the particle centers (Fig. D.5c). Such coordinated motions were considerably faster that the propulsion velocity of individual Janus particles perhaps suggesting an additional strategy for directing CCEP motions. Importantly, we confirmed that the above effects involving two or more particles were also observed among spherically isotropic (non-Janus) particles. Understanding the complex dynamics of multiple particles moving by CCEP will require further study beginning with the simplest spherical particles.

Conclusions

Contact charge electrophoresis drives the rapid oscillatory motion of conductive microparticles within nonpolar fluids. Particle asymmetries can be used to rectify such oscillatory motions to achieve directed transport perpendicular to the applied field. Rectified motions derive from particle rotations near the electrode surface upon contact charge transfer, which lead to repeated displacements in a common direction. This type of self-propulsion exhibits several characteristics that distinguish it from related systems based on self-phoresis, induced-charge electrophoresis, or Quicke rotation. Owing to the negligible electric currents through the nonpolar fluid, particle motions are highly efficient and require small energy inputs (ca. 1 nW / particle)

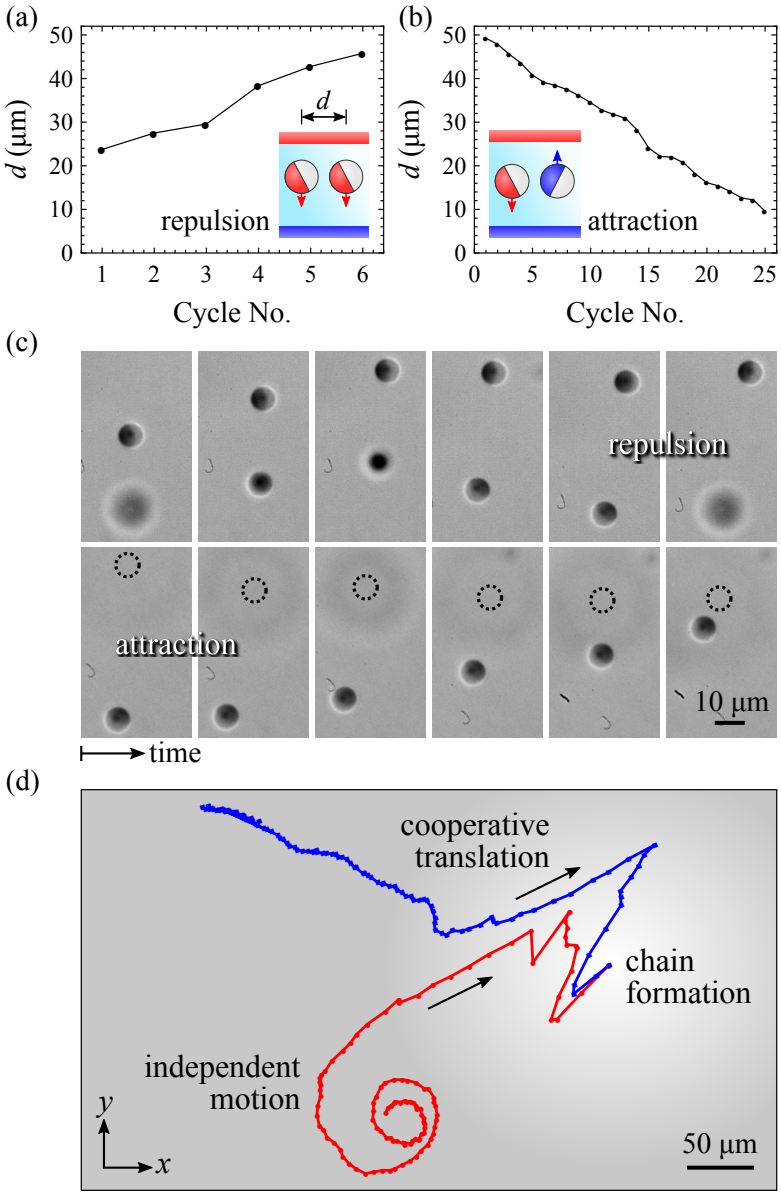

Figure D.5: (a) The horizontal distance d between two particles oscillating in phase increases during each oscillation cycle. (b) The distance between particles moving out of phase decreases each cycle. (c) Image sequence corresponding to data shown in (a) and (b). (d) Reconstructed trajectories for two interacting particles. Initially, the particles are moving independently until their separation becomes less than the electrode spacing (here, $H = 150$ μm). They then begin to move more quickly in a cooperative manner. Ultimately, the particles come together to form an oscillating chain. See supporting video 5.

[53]. Rapid particle motions can enhance microscale mixing within nonpolar fluids [31], which could be harnessed to accelerate catalytic reactions limited by mass transfer. Long-ranged electrostatic interactions among the particles results in complex collective motions relevant to the study of active matter. Importantly, the directed CCEP motions of asymmetric particles can in principle be engineered by tuning the particle shape and surface composition. The rational design of such active components is a critical prerequisite for constructing dynamic colloidal assemblies capable of useful functions – that is, colloidal machines.

Methods

Experimental details

Silica Janus particles were prepared by deposition of gold onto particle monolayers supported on glass slides. Following Prevo and Velev [171], 10 μL of a concentrated (30 wt%) suspension of 8 μm silica particles in water was placed between two acid-cleaned microscope slides mounted at an angle on a motorized stage (Harvard Apparatus PHD 2000). The trapped colloidal solution was dragged at a prescribed speed by the motion of the top slide to achieve well-packed monolayers. Successive layers of metal (5 nm Ti and 10 nm Au) were then deposited by physical vapor deposition (Cressington 308).

Fluorescent Janus particles were prepared following a procedure adapted from Kopelman et al. [179]. Briefly, sulfonated fluorescent polystyrene particles (ThermoFisher F8858) were washed three times in water by centrifugation and dispersed in methanol at a concentration of 1% w/v. 0.5 ml of the particle suspensions was

deposited onto a 4-inch silicon wafer wafer by spin coating at 2500 rpm for 15 min. Successive layers of metal (5 nm Ti, 25 nm Ni, and 20 nm Au) were then deposited by e-beam evaporation (Kurt J Lesker Co. Lab 18). The nickel layer was included for a purpose unrelated to the present experiments and is unnecessary here. The particles were gently brushed off the wafer using a damp brush.

The electrode setup was comprised of two indium tin oxide (ITO)-coated glass slides (SIGMA-Aldrich, CAS:50926-11-9, surface resistivity 70-100 Ω/sq) separated from one another by spacers made of glass (200 μm thick cover slides) or polydimethylsiloxane (PDMS, 50 μm to 150 μm thick). The ITO electrodes were connected to a high-voltage source (Keithley 2410 1100V SourceMeter) with a limiting current of 10 μA to prevent damage to the system in the event of a short-circuit. The Janus particles were dispersed in Nylon membrane-filtered mineral oil (SIGMA-Aldrich, CAS:8042-47) at a concentration of $0.01 - 1$ mg/ml and injected into the inter-electrode region. We note that the charge relaxation time for mineral oil is considerably larger the the timescale of particle oscillations, which is a necessary condition for CCEP [31]. The field-induced motion of the Janus particles was captured by a high speed camera (Phantom V310) mounted on an optical microscope (Zeiss Axio Imager A1) operating in bright field mode with 10x and 50x objectives.

Particle tracking analysis

Movies were captured at frame rates of 1,000 – 5,000 fps and processed in MATLAB to analyze particle oscillations and reconstruct particle trajectories. To determine the oscillation frequency, we first identified a fixed window around a single particle and computed the window-averaged pixel intensity for each frame. This average

intensity oscillated in time as the particle moved into and out of focus, reaching its local minimal value when the particle came into focus at the lower electrode. For each oscillation cycle $i = 1, 2, \ldots, N$, we identified the time t_i when the particle contacted the lower electrode. The mean oscillation frequency was then computed by dividing the number of particle oscillations by the total observation time, $f = N/(\Sigma_i t_i)$. To reconstruct particle trajectories (x_i, y_i), we considered only those frames when the particle was in focus (i.e., when the average intensity was minimal) and determined the location of the particle center using standard algorithms [15]. The net displacement for cycle i was computed as $\Delta_i^2 = (x_{i+1} - x_i)^2 + (y_{i+1} - y_i)^2$; the average speed of the particle (parallel to the electrodes) was computed as $U_\perp = (\Sigma_i \Delta_i)/(\Sigma_i t_i)$.

Theoretical model

The model of CCEP dynamics combines classical electrostatics and low Reynolds number hydrodynamics [53]. The metallic hemisphere of the Janus particle as well as the bounding electrodes are treated as perfect conductors. To facilitate our numerical analysis, the conductive portion of the particle is modeled as a solid hemisphere with rounded corners (radius $0.1a$) in contrast to the thin hemispherical cap present in experiment. Additionally, the non-metallic hemisphere and the surrounding fluid are assumed to be dielectrics with a common permittivity ε. Given the particle charge q, orientation α, and height z_p above the electrode surface, we solve the Laplace equation numerically to determine the electric potential Φ and field $\boldsymbol{E} = -\nabla\Phi$ throughout the dielectric medium (see Supporting Information for details). We then integrate the Maxwell stress over the surface of the conductive hemisphere to determine the electric force and torque that drive particle motion. At low Reynolds numbers (in experiments

$Re \leq 0.01$), the translational and rotational velocities of the particle are linearly related to the external force and torque by the so-called resistance tensor [118, 192]. For a spherical particle near a solid plane boundary, there exist exact analytical expressions [118] for the components of this tensor, which, when suitably rescaled, depends only on the separation between the sphere and the plane. Using these expressions, we compute the particle velocity and integrate numerically to determine the position and orientation of the particle as a function of time. We assume that the charge q on the particle remains constant until the surface of the metallic hemisphere reaches some critical separation δ from the plane electrode, at which point charge flows to/from the particle instantaneously to reverse the particle polarity ($q \rightarrow -q$). Physically, the contact charging process is thought to occur by a type of dielectric breakdown; the resulting charge on the particle is somewhat variable but consistently less than that expected at equilibrium (i.e., when the potential on the particle equals that of the electrode) [53]. After nondimensionalization, the computed particle trajectories depend on just two parameters: the dimensionless charge $q/4\pi\varepsilon a^2 E$ and the dimensionless separation at contact δ/a. Figure S6 shows how the net lateral displacement per collision Δ depends on these two parameters.